Doctoral Dissertation

Double activation of oxygen intermediates of oxygen reduction reaction by dual polymer/oxide electrocatalysts

Dong-Gyu Lee

Department of Energy Engineering

Graduate School of UNIST

2020

Double activation of oxygen intermediates of oxygen reduction reaction by dual polymer/oxide electrocatalysts

Dong-Gyu Lee

Department of Energy Engineering

Graduate School of UNIST

Double activation of oxygen intermediates of oxygen reduction reaction by dual polymer/oxide electrocatalysts

A dissertation
submitted to the Graduate School of UNIST
in partial fulfillment of the
requirements for the degree of
Doctor of Philosophy

Dong-Gyu Lee

11 / 22 / 2019 of submission
Approved by

_____

Advisor
Hyun-Kon Song

Double activation of oxygen intermediates of oxygen reduction reaction by dual polymer/oxide electrocatalysts

Dong-Gyu Lee

This certifies that the dissertation of Dong-Gyu Lee is approved.

11 / 22 / 2019 of submission

signature

_____

Advisor: Hyun-Kon Song

signature

_____

Jae Sung Lee

signature

_____

Sang Hoon Joo

signature

_____

Sang Kyu Kwak

signature

_____

Yongkook Kwon

Abstract

Oxygen reduction reaction (ORR) is one of the classical topics in electrochemistry which has been investigated for several decades. ORR, a notoriously sluggish cathodic process, requires an electrocatalyst to improve its kinetics. Platinum is well-known as the best catalyst for ORR. However, due to its high cost, many kinds of catalyst such as non-precious-metal-based catalysts (metal oxide, metal alloy and M-N-C) and metal-free catalysts (nitrogen doped carbon) have been studied as replacements for platinum. These studies on catalyst development commonly focus on significant generation of active sites. In this dissertation, dual polymer/oxide electrocatalytic system is presented, which further improves catalytic activity by adding the polymers that interact with the oxygen, not active site of oxides. The additional components act as co-catalysts by simultaneously participating in ORR with the original catalyst. The double activation of oxygen intermediates in the dual electrocatalytic system reduces adsorption energies of intermediates compared to a single catalytic system. Dual electrocatalysis achieved by simply mixing metal oxide particles (original catalyst) with polymers (additional catalyst) is one of the most efficient and easiest ways to improve the catalytic activity of cost-efficient catalysts to match the level of precious metal catalysts.

Firstly, perovskite oxides were investigated as a catalyst for ORR. Perovskite is a good model for the basic investigation of electrocatalysis because their physical properties, especially electrical conductivities, can be dynamically controlled with their composition and stoichiometry. Controlling conductive environment surrounding active sites, achieved by more conductive catalysts (providing internal electric pathways) or higher carbon content (providing external electric pathways), contributes to presenting the conductivity-dependent trend of the number of electron transfer in ORR.

Then, the perovskite catalysts were studied in presence of polypyrrole (pPy), which is the first additional catalyst considered for ORR. Nitrogen-containing electrocatalysts such as metal-nitrogen-carbon (M-N-C) composites and nitrogen-doped carbons are known to exhibit high activities for ORR. Even if the mechanism by which nitrogen improves the activities is not completely understood, strong electronic interaction between nitrogen and active sites has been found in these composites. In this work, I demonstrate a case in which nitrogen improves electroactivity, but in the absence of strong interaction with other components. The overpotentials of ORR and oxygen evolution reaction (OER) on perovskite oxide catalysts were significantly reduced by simply mixing the catalyst particles with polypyrrole/carbon composites (pPy/C). Any strong interactions between pPy (a nitrogen-containing compound) and active sites of the catalysts were not confirmed, but interaction between secondary amine(N-H) of pPy and oxygen was observed.

To activate oxygen and other intermediates, a series of the secondary amine conjugated polymers (HN-CPs) was tested with three different cobalt-based electrocatalysts (CoO, Co_3O_4, and $LiCoO_2$). In this work, the synergistic electrocatalysis of oxygen reduction reaction (ORR) was successfully demonstrated by showcasing the significantly improved kinetics of ORR. The electron donation number of the HN-CPs to diatomic oxygen (δ in $O_2^{\delta-}$) described the order of activity improvement by polypyrrole (pPy) > polyaniline (pAni) > polyindole (pInd). The maximum overpotential gain at ~150 mV was achieved by using pPy, characterized by the highest δ. In the mechanism, the activated diatomic oxygen species ($O_2^{\delta-}$) was transferred to the active site of electrocatalysts, while maintaining interaction with NH-CPs. As ORR proceeded along the mechanistic pathway following *OO → *OOH → *O → *OH → *OO (the surface intermediates on catalyst), the proton of the HN-CP was transferred to the single oxygen surface species (*O). The kinetic gains were obtained in the surface single oxygen formation step (*OOH to *O) at the equilibrium potential and the proton transfer step (*O to *OH) at a biased potential by the dual catalysis, when compared with the conventional electrocatalysis in the absence of OA (RDS = the surface peroxide formation step of *OO to *OOH).

Keywords: Oxygen reduction reaction • Dual electrocatalysis • Secondary-amine-conjugated polymer

Contents

List of Figures

cm^{-2}). **(b)** Number of electron transfer for overall processes ($\underline{n}_{overall}$). The values of $n_{overall}$ were calculated from currents on disk and ring electrodes along cathodic scan at the same rpm used in (a) during ORR. Its average values ($\underline{n}_{overall}$) were calculated by averaging $n_{overall}$ values at 0.33 V and 0.53 V. **(c)** Number of electron transfer for rate determining step (n_{RDS}). The values of n_{RDS} were calculated from Tafel slopes (b) by using the relationship: b = 60 mV dec^{-1}/ (n_{RDS} α) where transfer coefficient (α) was assumed to be 0.5. A single catalyst particle (yellow circle) surrounded by multiple carbon black (black circles) were schematically illustrated corresponding to their carbon compositions on the top of (b) and (c).

Figure 5. Voltammograms of disk (a to d) and ring (a' to d') currents of ORR in 0.1 M KOH (aq) at cathodic scan (10 mV sec^{-1}) on 1600 rpm in the presence of perovskite oxide catalysts (Loading density, L = 0.8 mg total cm^{-2} with total = oxide + carbon; disk area = 0.1256 cm^2). Background currents were presented in the presence of nitrogen without oxygen (grey solid lines). The background currents were estimated negligible when compared with ORR currents for all carbon contents.

Figure 6. The effects of local potential distribution nearby the active sites on $n_{overall}$. **(a)** Potential dependency of $n_{overall}$. The critical overpotentials (η_c) at which the $n_{overall}$ dramatically decreases were indicated. **(b)** BSCFO and NBSCO as representative examples of less versus more conductive catalysts, respectively. Overpotential (η) gradients are decreasingly developed along a direction away from the contact point with carbon through the body of catalyst.

Figure 7. Tafel plots of ORR polarization: solid lines = all experimental data; symbols = data points used for obtaining Tafel slope b (mV dec^{-1}); dashed lines = linear regression lines fitting symbols.

Figure 8. ORR cyclability test. Disk currents (i_{disk}) at +0.68 V vs. RHE were recorded along cycles at which potential was scanned at 50 mV s^{-1} between +0.2 V and +1 V vs. RHE.

Figure 9. RHE calibration and Collection efficiency. **(a)** RHE calibration. Pt wires were used as working and counter electrodes while Hg/HgO was used as a reference electrode. The potential was swept at 1 mV s^{-1} in H_2-saturated 0.1 M KOH (aq). The open circuit potential was measured at -0.929 V vs. Hg/HgO. **(b)** Collection efficiency (N). $Fe(CN)_6^{3-}$/ $Fe(CN)_6^{4-}$ was used as a reversible redox couple for the measurement.

Figure 10. Electron-microscopic characterization of NBSC. **(a)** A TEM image at low magnification. **(b)** A TEM image at high magnification with its fast Fourier transformed pattern. Spots of weak intensity in the pattern were observed when electron beam was introduced in a [110] direction. They are indexed with (001) of a tetragonal super lattice, indicating the double perovskite structure. **(c)** Element mapping

by energy dispersive spectroscopy (EDS). Each component was uniformly distributed throughout particles.

Figure 11. ORR **(a)** ORR polarization in 0.1 M KOH (aq) at cathodic scan (10 mV sec^{-1}) on 1600 rpm. C (Ketjenblack EC-600JD) or pPy/C was used at 20 wt. % with perovskite oxide catalysts (NBSC or BSCF). Open and solid circles on curves means +C and +pPy/C, respectively. Pt/C = Pt + 80 wt. % C. Loading density (L in mg_{total} cm^{-2} with total = oxide + carbon) = 0.8 for the perovskite catalyst layers and 0.4 for C and pPy/C. Baselines obtained from N_2-purged electrolyte for each sample were included. (**b**) Kinetic current densities (j_K) at 0.68 V_{RHE} and exchange current densities (j_o). **(c)** Number of electron transfer (n). (d) Potential profiles for the galvanostatic discharge at 20 mA cm^{-2} in zinc-air batteries. The ORR and OER polarization curves were obtained reproducibly.

Figure 12. Reproducibility of the NBSC+pPy/C performances. **(a)** ORR polarization in 0.1 M KOH (aq) at cathodic scan. **(b)** OER polarization in 0.1 M KOH (aq) at anodic scan. Scan rate = 10 mV sec^{-1}. Rotation speed = 1600 rpm.

Figure 13. OER &Bifunctionality **(a)** OER polarization at anodic scan (10 mV sec^{-1}) on 1600 rpm. The contents of C and pPy/C were indicated in Figure 1. **(b)** OER Stability. The OER current (i_{OER}) at 1.83 V was traced along repeated cycles between 0.93 V and 1.83 V vs. RHE. (**c**) Bifunctionality represented by potential gaps (Δ) between the potentials at -3 mA cm^{-2} for ORR (E_{ORR}) and at +10 mA cm^{-2} for OER (E_{OER}). TheΔ are indicated as numerical values while bars indicate the overpotential of ORR and OER (η; E_{eq} = 1.23 V vs. RHE).

Figure 14. TEM images of carbon black and pPy/C. **(a)** C = Ketjen black. **(b)** 20 % pPy/C. **(c)** 40 % pPy/C. The scale bars are for 50 nm.

Figure 15. ORR and OER of NBSC in the presence of different conducting agents: carbon (Ketjen black; C) and polypyrrole/carbon black composite (pPy/C). **(a)** Voltammogram of disk currents of ORR in 0.1 M KOH (aq) at cathodic scan (scan rate = 10 mV sec^{-1}; rotation speed = 1600 rpm). (b) Number of electron transfer (n). **(c)** Voltammogram of disk current of OER at anodic scan (scan rate = 10 mV sec^{-1}; rotation speed = 1600 rpm). (d) Stability of OER. The OER current (i_{OER}) at 1.83 V vs. RHE was traced along repeated cycles consisting of anodic and cathodic scans between 0.93 V and 1.83 V vs. RHE.

Figure 16. X-ray photoelectron spectra of Co 2p with the survey spectra. **(a, b)** NBSC. **(c, d)** NBSC + pPy/C. There were no differences observed between the two samples.

Figure 17. Sequential role allocation between pPy and oxide during ORR. (**a**) Proposed mechanism to explain the role of pPy on improved kinetics of ORR. (**b**) Frequency changes of a pPy-deposited quartz resonator in nitrogen-purged (black) or oxygen-saturated (red) deionized water. The optimized geometries of (**c**) O_2+ pPy, (**d**) NBSC+O_2 and (**e**) NBSC+O_2+pPy. The adsorption energy (ΔE_{ad}) of O_2 is indicated on top of each figure. Total charge of O_2 molecule and optimized distance between Co ion and O_2 are colored black and blue, respectively. Dashed cyan line indicates hydrogen bond. The gray dashed line indicates both lattice and periodic boundary.

Figure 18. Tafel plots. (a)ORR. (b)OER.

Figure 19. Spectroscopic characterization of pPy in the presence of O_2. **(a)** Infrared spectra. The peak at 3737cm^{-1} for OH stretching was developed along time when the pPy films were exposed to oxygen or air. **(b)** Temporal change in the absorbance at 3737cm^{-1}.

Figure 20. Proposed mechanism to explain the role of pPy on improved kinetics of ORR.

Figure 21. Optimized structures for DFT calculation. **(a)** NBSC. **(b)** pPy. **(c)** O_2. **(d)** (001) surface of NBSC. The labels of atomic colors are presented in the figure. The gray dashed line indicates both lattice and periodic boundary.

Figure 22. ORR polarization of NBSC in the presence of nitrogen-containing conducting polymers. Electrocatalytic layers were prepared by introducing 5 wt. % conducting polymer/carbon composites into NBSC. Doped pPy, undoped pPy or polyaniline was used as the conducting polymer. Scan rate = 10 mV sec^{-1}. Rotation speed = 1600 rpm.

Figure 23. Polarization of peroxide reduction on NBSC in the presence of 2mM peroxide in 0.1M KOH (aq)(red solid line). Presented for comparison was the ORR polarization on NBSC in oxygen-saturated 0.1M KOH (aq) (blue solid line). Scan rate = 10 mV sec^{-1}. Rotation speed = 1600 rpm.

Figure 24. Electrodeposition of pPy on NBSC+C. **(a)** Cyclic voltammogram (CV) of the ORR on disk electrode in N_2-saturated 0.1 M KOH (aq) at 10 mV sec^{-1}. Black, red and blue line are pPy03, pPy06 and pPy09.

Figure 25. ORR on pPy-deposited perovskite oxide. 0, 0.3, 0.6 and 0.9 wt. % of pPy was electrochemically deposited on NBSC. **(a)** ORR polarization in 0.1 M KOH (aq) at cathodic scan at 10 mV sec^{-1} at 1600 rpm. The pPy amounts were indicated. **(b)** The number of electron transfer (n). **(c)** Oxygen reduction on perovskite catalysts covered with pPy of three different thicknesses.

Figure 26. ORR and OER of pPy/NBSC. Black, red and blue lines are 0.3, 0.6 and 0.9 wt. % of pPy on NBSC catalyst layer, respectively. **(a)** ORR polarization in 0.1 M KOH (aq) at cathodic scan (scan rate = 10 mV sec^{-1}; rotation speed = 1600 rpm). **(b)** Tafel plots. **(c)** Voltammogram of ring current of re-oxidization at 0.4V. (d) OER polarization at anodic scan (scan rate = 10 mV sec^{-1}; rotation speed = 1600 rpm).

Figure 27. NBSC + pPy/C versus NBSC + C + pPy. It should be notified that the pPy-deposited system includes carbon (C) because pPy was electrodeposited on a mixture of NBSC and C (NBSC+pPy+C). The ORR kinetics was faster in NBSC+pPy/C than in NBSC+pPy+C when comparing the slopes of current increase before the limiting situation between the two systems. Electric conductivity would not be significantly different between NBSC+pPy/C and NBSC+C+pPy. However, the major difference comes from mass transfer. The use of pPy/C guarantee the porosity between the particles of NBSC and pPy/C. On the contrary, pPy films could block the ionic pathways existing between NBSC and C in the NBSC+C+pPy system.

Figure 28. Improved ORR activities in the presence of NH-CPs. **(a)** The number of electrons transferred from NH-CPs to diatomic oxygen (δ). **(b to d)** The ORR polarization curves of cobalt-based electrocatalysts in the presence of NH-CPs. The overall ORR currents on catalyst-loaded disk electrodes were recorded in 0.1 M KOH (aq) when the potential was cathodically swept at 10 mV sec^{-1} and 1600 rpm. The electrocatalysts are indicated. **(e)** Kinetic current density (i_k) at 0.68 V_{RHE} (versus reversible hydrogen electrode) of the cobalt-based catalysts in the presence of NH-CPs.

Figure 29. The correlation between the electron donation number of NH-CP to oxygen (δ) and the HOMO level of NH-CP. The value of |δ| is proportional to the charge transfer energy, which is determined by the difference between HOMO of NH-CP and the LUMO of oxygen.

Figure 30. X-ray photoelectron Co 2p spectra of cobalt-based electrocatalysts.

Figure 31. ORR of CoO. **(a)** Number of electron transfer (n). **(b)** production of peroxide. **(c)** Voltammogram of ring currents of ORR in 0.1 M KOH (aq) at cathodic scan (scan rate = 10 mVsec^{-1}; rotation speed = 1600 rpm).

Figure 32. ORR of Co_3O_4. **(a)** Number of electron transfer (n). **(b)** production of peroxide. **(c)** Voltammogram of ring currents of ORR in 0.1 M KOH (aq) at cathodic scan (scan rate = 10 mV sec^{-1}; rotation speed = 1600 rpm).

Figure 33. ORR of $LiCoO_2$. **(a)** Number of electron transfer (n). **(b)** production of peroxide. **(c)** Voltammogram of ring currents of ORR in 0.1 M KOH (aq) at cathodic scan (scan rate = 10 mV sec^{-1};

rotation speed = 1600 rpm).

Figure 34. Turnover frequencies (TOF) of the four-electron ORR on three different electrocatalysts (CoO, Co_3O_4 and $LiCoO_2$) in the presence of NH-CPs. The TOF was calculated by:

TOF of 4e ORR = N_{Avo} x i_k x f_{4e} / F / n_{active}

where i_k = kinetic current at 0.68 V_{RHE}; N_{Avo} = Avogadro's number; F = faraday constant;

f_{4e} = fraction of $4e^-$ process = $(I_d-I_r/N)/(I_d+I_r/N)$

with I_d = disk current; I_r = ring current; N = collection efficiency;

n_{active} = number of active sites = A_{geo} / A_{active}

with

A_{geo} = geometric surface area of a catalyst under the assumption of spherical particles

= $(m_{cat} / d_{cat}) / \{4 \pi (d_{particle}/2)^3/3\}$ x $4 \pi (d_{particle}/2)^2$

m_{cat} = mass of catalyst loaded on electrode; d_{cat} = density of catalyst

$d_{particle}$ = particle size (100nm)

A_{active} = area of unit cell (100) / the number of cobalt in unit cell (100) under assumption of (100) termination on the surfaces

= $(4.26\ Å)^2/2$ for CoO, $(8.06\ Å)^2/4$ for Co_3O_4 and (2.44 Å x 3.42 Å)/3 for $LiCoO_2$

Figure 35. The δ-dependency of the ORR activity. The half-wave overpotential ($\eta_{1/2}$; filled symbols) or the onset potential (E_{onset}; open symbols) was used as the ORR activity measure in the ordinate. The number of electrons donated by the NH-CP to oxygen, δ, was used as the NH-CPs descriptor in the abscissa. Three different cobalt-based oxides (CoO, $LiCoO_2$ and Co_3O_4) were tested as the ORR electrocatalysts in the presence of three different HN-CPs (**pPy**, **pAni** and **pInd**).

Figure 36. The binding energy (ΔE^{bind}) of diatomic oxygen species (the neutral or activated oxygen molecules, O_2 or $O_2^{\delta-}$) to CoO. The activated oxygen is generated in the presence of **pPy**. The more negative value indicates the stronger binding of oxygen molecule to CoO.

Figure 37. Adsorption of the neutral and partially charged diatomic oxygen species (O_2 and $O_2^{\delta-}$) on CoO catalyst. Bader charges developed in the diatomic species and the distance between an oxygen atom of the diatomic oxygen species and a cobalt atom of the surface lattice of CoO were indicated. The activated diatomic oxygen ($O_2^{\delta-}$) was generated in the presence of **pPy**.

Figure 38. Hybridization between d_{z^2}-orbital of Co and *p*-orbital of O_2 molecule (*i.e.*, anti pi-bonding state near Fermi level, E_F) at CoO surface**. (a)** Molecular representation: red sphere = oxygen; blue sphere = cobalt; oval = orbital. **(b and c)** Partial density of states (PDOS) of cobalt of CoO and adsorbed O_2 in the absence of **pPy** (**b**) and in the presence of pPy (**c**): red = total *d*-orbital of Co bonded to O_2;

blue = d_{z^2}-orbital of Co bonded to O_2; green = *p*-orbital of O_2. The d_{z^2}-orbital of Co and the *p*-orbital of O_2 are hybridized near E_F (indicated by arrows). The hybridized bonding orbital near E_F was partially filled when the neutral oxygen molecule (O_2) was activated to be the polarized oxygen molecule ($O_2^{\delta-}$) by the aid of **pPy**. The binding of the diatomic oxygen species to CoO surface is strengthened by the partially filled bonding orbital.

Figure 39. Energy diagram along ORR mechanism at the equilibrium potential ($U = U_{eq}$): main catalyst = CoO; additional catalyst = pPy. The pPy-present system (red) was compared with the pPy-absent system (black). The energy gap of the rate determining step of each system was indicated: 0.35 eV for the pPy-present system versus 1.05 eV for the pPy-absent system.

Figure 40. Molecular representation of the intermediate states along ORR mechanism on CoO electrocatalyst in the absence versus presence of **pPy** as the additional catalyst.

Figure 41. The mechanism of proton transfer in NH-CP assisted electrocatalysis for ORR. (**a**) A suggested mechanism of proton transfer from NH-CP to oxygen adsorbate in NH-CP assisted ORR on cobalt-based catalysts (M=active site of cobalt-based catalysts). (**b**) ORR polarization curves of CoO electrocatalyst without (solid lines) or with **pPy** (dashed lines) in a buffer solution at pH 7 (red) and 0.1 M KOH (blue; pH 13). Potential was cathodically scanned at 10 mV sec^{-1} while disk electrodes were rotated at 1600 rpm. (**c**) Energy required for the proton transfer from **pPy** to the four different intermediate states generated on CoO during the ORR.

Figure 42. Deutriation of pyrrole. **(a)** Fourier-transform infrared (FTIR) spectra of H_2O (black), D_2O (red) and pyrrole dissolved in H_2O (blue) and D_2O (magenta). **(b)** The closer look of the FTIR spectra **a** between 700 cm^{-1} and 1250 cm^{-1}. The wavenumber of the peak assigned to N-H in-plane vibration mode shifted from 1050cm^{-1} to 750cm^{-1} after deutriation.

Figure 43. ORR activities of CoO in the presence of polythiophene **(pTp).** Linear sweep voltammograms of the ORR disk current were obtained in 0.1 M KOH (aq) at cathodic scan (scan rate = 10 mV sec^{-1}; rotation speed = 1600 rpm). Black = CoO; Red = CoO + pTp.

Figure 44. ORR activities of CoO in an aprotic solvent. Cyclic voltammograms of the ORR disk current at 1st (solid line), 2nd (dashed line) and 8th cycle (dotted line) were obtained in 0 .1 M $LiClO_4$ in acetonitrile at cathodic scan (scan rate = 20 mV s^{-1}). Blue = CoO; Red = CoO + pPy.

Figure 45. Stability. The ORR polarization curves of the CoO electrocatalyst without (blue) or with pPy (red) at 10th cycle (dashed lines) and 500th cycle (solid lines). The potential was cathodically scanned at 50 mV sec^{-1} while the disk electrodes were rotated at 1600 rpm. Half-wave potential was

shifted about 10mV during 500 cycles in both cases.

Figure 46. Tafel plots of ORR on catalysts in the absence and presence of NH-CPs. **(a)** CoO. **(b)** Co_3O_4. **(c)** $LiCoO_2$.

Figure 47. The rate determining step (RDS) of NH-CP assisted ORR catalysis at biased potentials. **–pPy** = conventional catalysis in the absence of NH-CPs; **+pPy** = dual catalysis in the presence of **pPy** as one of the NH-CP. **(a)** Energy diagrams along the ORR mechanism. The energies of the intermediate and final states relative to the first state were calculated by DFT. The final state was biased relative to the first state by $U = 0$ so that the energy gap between the first and final states was 5.04 eV = $|(U - U_{eq}) \times 4e| = |(0\ V - 1.26\ V) \times 4e|$. The value of U_{eq} was estimated at 1.26 V by DFT, which is a measure of the standard reduction potential of the ORR versus normal hydrogen electrode (practically known as 1.23 V versus NHE). **(b)** The number of electrons transferred (n) in the overall ORR process on the four different cobalt-based catalysts. **(c)** Tafel plots for the ORR on $LiCO_2$ in the presence of the three different NH-CPs.

Figure 48. The overpotential (η) dependency of the number of electron transferred (n). **(a)** Conventional ORR catalysis in the absence of OA. **(b)** NH-CP-assisted ORR catalysis in the presence of OA. The 2e transfer becomes preferred in the catalysis as the applied overpotential increases.

Figure 49. The onset potential (E_{onset}) in the linear sweep voltammograms for investigating the ORR polarization. The E_{onset} was read from the point of intersection between the abscissa at zero current and the line tangent to the polarization curve at high overpotential region. **(a)** CoO, **(b)** Co_3O_4 and **(c)** $LiCoO_2$

Figure 50. Cyclic voltammogram of polyindole redox reaction on catalyst-loaded electrode in oxygen saturated 0.1 M KOH(aq) at 10mV/s of scan rate.

Figure 51 Chronoamperometry for electro-polymerization of indole on carbon electrode at 1 mA/cm^2 of constant current density.

Figure 52. (a) Unit cell structure and **(b)** (001) surface of CoO. The labels of atomic colors are presented in the figure. The applied formal spins are numbered on cobalt atoms. Lattice and periodic boundary are represented by dashed line.

Figure 53. Model systems for **(a)** $CoO+O_2$+pPy and **(b)** $CoO+O_2$+ pPy-H. The labels of atomic colors are represented in the figure.

List of Tables

I. Introduction

1.1 Oxygen Reduction Reaction

Oxygen (O_2) is an abundant resource in nature. The oxygen reduction reaction (ORR) is very important as it serves as the working principle of many energy conversion systems such as fuel cells and metal-air batteries. The ORR, especially in aqueous media, is mainly classified into two pathways depending on the number of electrons transferred (**Scheme 1**): 1) direct 4-electron pathway from O_2 to water (H_2O in acid) or hydroxide ion (OH^- in alkaline). and 2) 2-electron pathway from O_2 to hydrogen peroxide (H_2O_2 in acid, HO_2^- in alkaline). By receiving additional two electrons after 2-electron pathway, the indirect 4-electron pathway is possible. In organic or strong alkaline media, one more pathway is considered: 3) 1-electron pathway from O_2 to superoxide O_2^-.

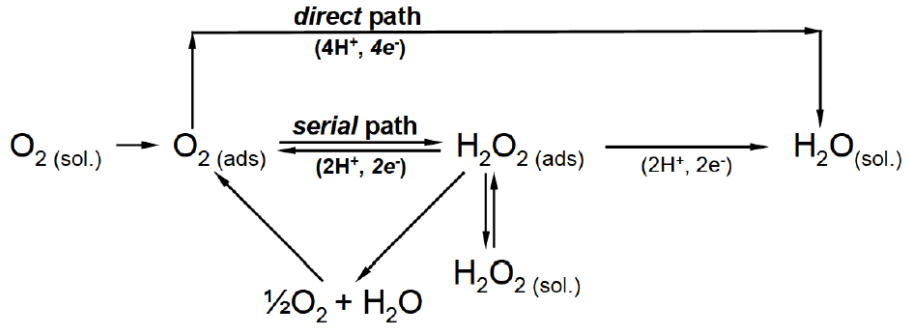

Scheme 1. Mechanism of Oxygen reduction reaction (ORR).

Thermodynamic potentials of ORR at standard conditions in different media are given as follows (**Table 1**). The potentials of ORR in organic media are not mentioned because these show increased variation depending on the organic solvent used.

Table 1. Standard formal potential of ORR.[1]

Media	*ORR*	E^0(V)
Acid Media	$O_2 + 4H^+ + 4e^- \rightarrow 2H_2O$	1.229
	$O_2 + 2H^+ + 2e^- \rightarrow H_2O_2$	0.70
Alkaline Media	$O_2 + 2H_2O + 4e^- \rightarrow 4OH^-$	0.401
	$O_2 + H_2O + 2e^- \rightarrow HO_2^- + OH^-$	-0.065
Organic Media	$O_2 + e^- \rightarrow O_2^-$	-
	$O_2^- + e^- \rightarrow O_2^{2-}$	-

Due to its relatively high thermodynamic potential, ORR has been used as a cathodic process in many energy conversion systems. The energy systems are defined by which reactions are applied as a counterpart of ORR. The fuel cells are operated by using hydrogen oxidation reduction as a counterpart for ORR, and metal-air batteries are designed by using metal oxidation as an anode. There are many kinds of fuel cells depending on the type of electrolyte: Alkaline Fuel Cell (AFC), Phosphoric Acid Fuel Cell (PAFC), Molten Carbonate Fuel Cell (MCFC), Solid Oxide Fuel Cell (SOFC), and Proton Exchange Membrane Fuel Cell (PEMFC). The operating temperature, which is a function of the physical properties of electrolytes is the distinguishable characteristic of fuel cells. The metal-air batteries typically include zinc-air (Zn-Air) and lithium-air (Li-Air) batteries. Zinc-Air has the advantage that it can operate in aqueous solutions, While Li-Air has the advantage of a high theoretical voltage because lithium has a low oxidation potential. However, its physical properties are very unstable and the products are irreversible, and hence, it is currently in the research stage for commercialization. The theoretical working potentials of the fuel cells and metal-air batteries are given below (**Table 2**).

Table 2. Working potentials of ORR-related energy conversion system.[2]

System	***Anode***	***Cathode***	***Overall***	***ΔE*(V)**
Fuel cell	$H_2 \rightarrow 2H^+ + 2e^-$	$O_2 + 4H^+ + 4e^- \rightarrow 2H_2O$	$O_2 + 2H_2 \rightarrow 2H_2O$	1.23
Zn-Air	$Zn + 4OH^- \rightarrow 2Zn(OH)_4^{2-} + 2e^-$ $Zn(OH)_4^{2-} \rightarrow ZnO + H_2O + 2OH^- + 2e^-$	$O_2 + 2H_2O + 4e^- \rightarrow 4OH^-$	$Zn + O_2 \rightarrow 2ZnO$	1.65
Li-Air	$Li \rightarrow Li^+ + e^-$	$O_2 + e^- \rightarrow O_2^-$ $LiO_2 + Li^+ + e^- \rightarrow Li_2O_2$	$2Li + O_2 \rightarrow Li_2O_2$	2.96

In these energy conversion systems, the working voltages are practically limited by ORR because of their slow kinetics (exceptionally, mass transfer of O_2^- ions in solid electrolyte is a rate determining step in SOFC). Therefore, research on improving ORR kinetics is ongoing to implement highly efficient energy conversion systems.

As environmental issues grow, the importance of hydrogen peroxide (H_2O_2) is increasing day by day. In addition to daily uses of H_2O_2 such as bleaching, detergent, H_2O_2, which is decomposed to hydroxyl radical ($OH\cdot$), removes organic contaminants by advanced oxidation processes (AOPs). Recently, the electrochemical production of H_2O_2, which can replace industrial anthraquinone processes, has been illuminated. Achieving high selectivity of H_2O_2 within a plurality of products is a key point of electrochemical synthesis.[3] In order to bias peroxide generation, it is necessary not only to improve the kinetics of the ORR but also adopt a new strategic approach. If the kinetics of front steps based on the peroxide intermediate are relatively improved, while limiting the kinetics of the rear steps, high selectivity of H_2O_2 will be achieved.

1.2 Kinetics of Oxygen Reduction Reaction

As mentioned in previous chapter, improving the sluggish kinetics of ORR is very important for the applicable energy devices. Theoretically, it is ideal for the potential of ORR to be as close to the thermodynamic reversible potential. The reaction rate of an electrochemical reaction, $O_{xy} + ne^- \leftrightarrow R_{ed}$, is represented by current, which is varies in terms of overpotential. The current as function of overpotential is given in Butler-Volmer equation.

$$i = i_0(e^{\frac{\alpha nF}{RT}\eta} - e^{-\frac{(1-\alpha)nF}{RT}\eta})$$

Where i is the current density of ORR, η is the overpotential, i_0 is the exchange current density, α is the transfer coefficient, n is the number of electron transferred at the rate determining step, F is the faradaic constant, R is the ideal gas constant, and T is the temperature.

In this equation, the exchange current, which represents the reaction rate at overpotential is 0, is largely involved in the change of the reaction rate.

$$i_0 = Fk_0({C_{oxy}}^{1-\alpha}{C_{red}}^{\alpha})$$

Where i_0 is the exchange current density, F is the faradaic constant, k_0 is the rate constant, C_{oxy} and C_{red} are concentrations of oxidized and reduced electrochemical species, and α is transfer coefficient.

The exchange current is associated with the concentrations of electroactive species and the rate constant. The rate constant varies in terms of temperature according to Arrhenius equation.

$$k(T) = Ae^{[-\frac{E_a}{RT}]}$$

In this equation, the kinetic constant is related to activation energy, which is an intrinsic property of the electrochemical reaction. The electrochemical reactions with low activation energy are beneficial for generating large current densities. The one method to reduce the activation energy without changing the reactant and product is to use an electrocatalyst.

1.3 Electrocatalysts for Oxygen Reduction Reaction

ORR electrocatalysis is a heterogeneous catalysis. Various electrochemical catalysts have been investigated for decades to improve ORR kinetics. The electrocatalytic activities are dependent on the element playing the role of an active site. The main trend is to change the electronic structures of active sites to improve electrocatalytic activities. Moreover, because electrocatalysis is a surface reaction, morphologies of catalyst materials have been controlled to maximize electrochemical surface area (ECSA). It is also important to maintain this maximized activity for a long lifetime. For this purpose, research has been conducted to find an optimized catalytic system with high stability and high performance. The catalysts studied can be classified into three categories: precious-metal-based catalysts, non-precious metal-based catalysts, and metal-free catalysts.

The activities of the catalysts and their cost has an approximately inverse relation in ORR. Platinum is a representative precious-metal catalyst, which shows the highest electrocatalytic activity with direct 4-electron transfer in ORR. Palladium (Pd) and Iridium (Ir) are catalysts, which show slightly lower activity than Pt but show high performance. A variety of bimetallic Pt catalysts (Pt-M) have been reported to reduce the proportion of the expensive Pt in the catalyst system, while maintaining or further enhancing its high activity. In this bimetallic catalyst, Pt still acts as an active site and its catalytic activity is enhanced by changes in electronic structure caused by other adjacent metals.

The interest is largely driven by the aim to find effective and efficient electrocatalysts that do not depend on precious metals such as Pt and Pd. As non-precious metal catalysts for ORR, numerous transition metal-based materials such as oxides, carbides, and nitrides have been reported. Metal-Nitrogen-Carbon complexes (M-N-C) are a representative example, inspired by bio-catalysts. The initial work was based on the biomimetic approach using Fe and Co porphyrins and phthalocyanines. While these materials exhibited some electrocatalytic activity, they were limited by short lifetimes. In an effort to overcome this limitation, numerous investigators pursued the use of Fe and Co composites with nitrogen doped carbons (N doped carbon). In many cases, the nitrogen doped carbons were derived from polypyrrole and related materials. Upon high temperature pyrolysis, polypyrrole yielded nitrogen doped carbons, which, in turn, could bind transition metals such as Co and Fe. These composites exhibited ORR activity with greatly enhanced lifetimes.

Without combining with transition metals, N doped carbon is noted as an innovative metal-free catalyst, which exhibits high activity in ORR. It includes carbon materials such as graphene, fullerene, porous carbon, and carbon nanotubes. The active sites, carbon atoms that naturally present in the oxidized state, are reduced in the process of electrochemical redox reaction. The reduced carbon atoms are required in the re-oxidized state upon oxygen adsorption. The catalytic activity for ORR of N doped carbon arises from the improvement of oxygen adsorption due to the change in the charge density of the carbon atoms adjacent to N (**Scheme 2a**). It was reported that doping of heterogeneous atoms could change the oxygen adsorption mode from end-on adsorption (Pauling model, associative mechanism) to side-on adsorption (Yeager model, dissociative mechanism).

There are different types of nitrogen in N-doped carbon: 1) pyridinic N (bonded to two carbon atoms), 2) graphitic N (bonded to three carbons), 3) pyrrolic N (bonded to two carbon and one hydrogen atoms). The type of N mainly generating the active sites is still not clear. Recently, the carbon atoms adjacent to the pyridinic N were suggested as active sites in acidic conditions (**Scheme 2b**).

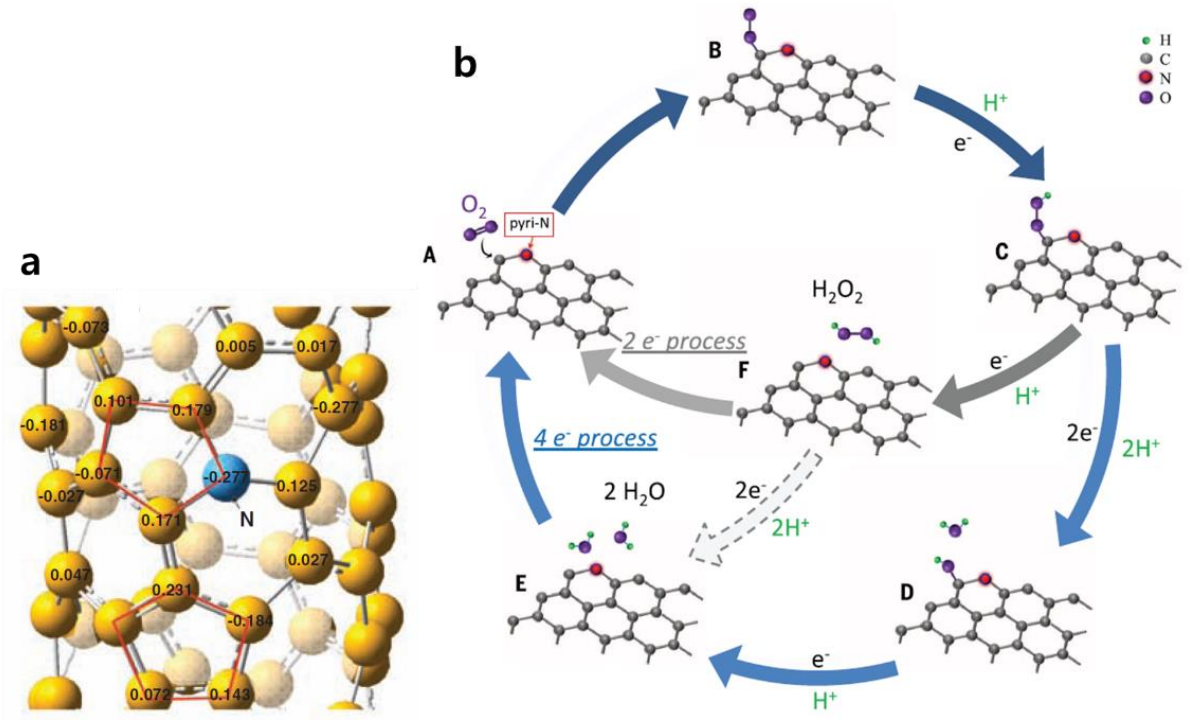

Scheme 2. (a) Charge density distribution in N-doped carbon nanotubes.[4] **(b)** Schematic pathway for ORR on N-doped carbon.[5]

1.4 Linear Scaling Relationship

In terms of ORR, extensive efforts to find high active catalysts have been exerted. Although many catalysts have been studied so far, no catalysts with higher performance than Pt have been found.

The theoretical approach using the density functional theory (DFT) coupled with the kinetics of electrocatalytic reaction has led to a reasonable understanding of volcano plots for catalytic activity (**Scheme 3a**). Volcano plots are represented by the linear relationship between the adsorption energies of different intermediates on the electrocatalysis (linear scaling relationship, **Scheme 3b**).[6] Breaking this linear correlation of intermediates is crucial to develop highly active electrocatalysts in ORR, even in electrochemical reactions.

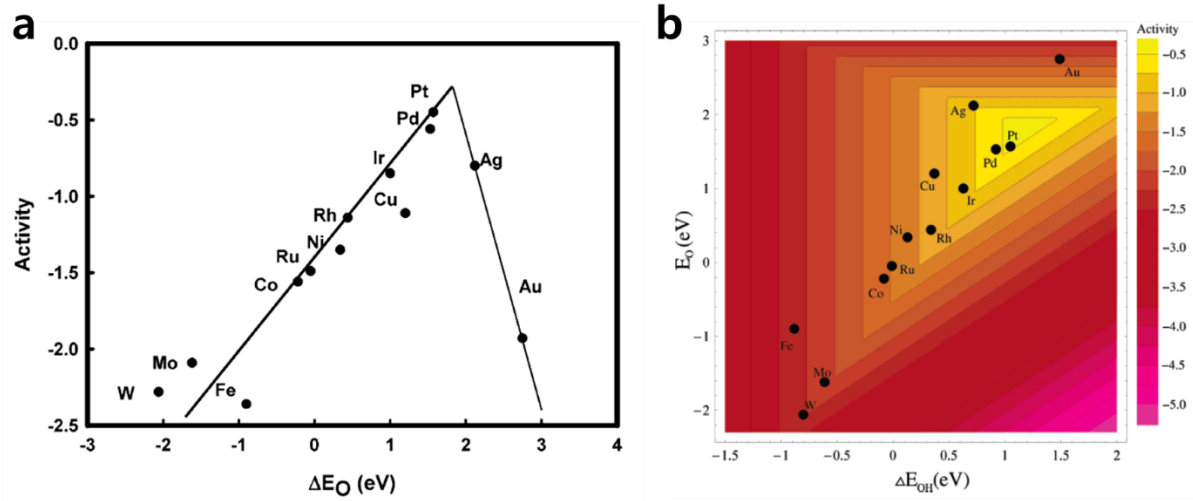

Scheme 3. (a) Volcano plots. Trends of ORR activities of metal catalysts plotted as a function of the O binding energy. **(b)** The dependencies of O and OH binding energy. Activity as the function of O and OH binding energy.[6]

There are have been several attempts to overcome the drawbacks of linear scaling relationships. Considering the catalysts studied so far, it is possible to find a solution in the complexity of the catalyst material. Pérez-Ramírez et al, graded the catalysts by complexity and compared it with the degree of escape from the linear relationship (**Scheme 4**).[7]

.

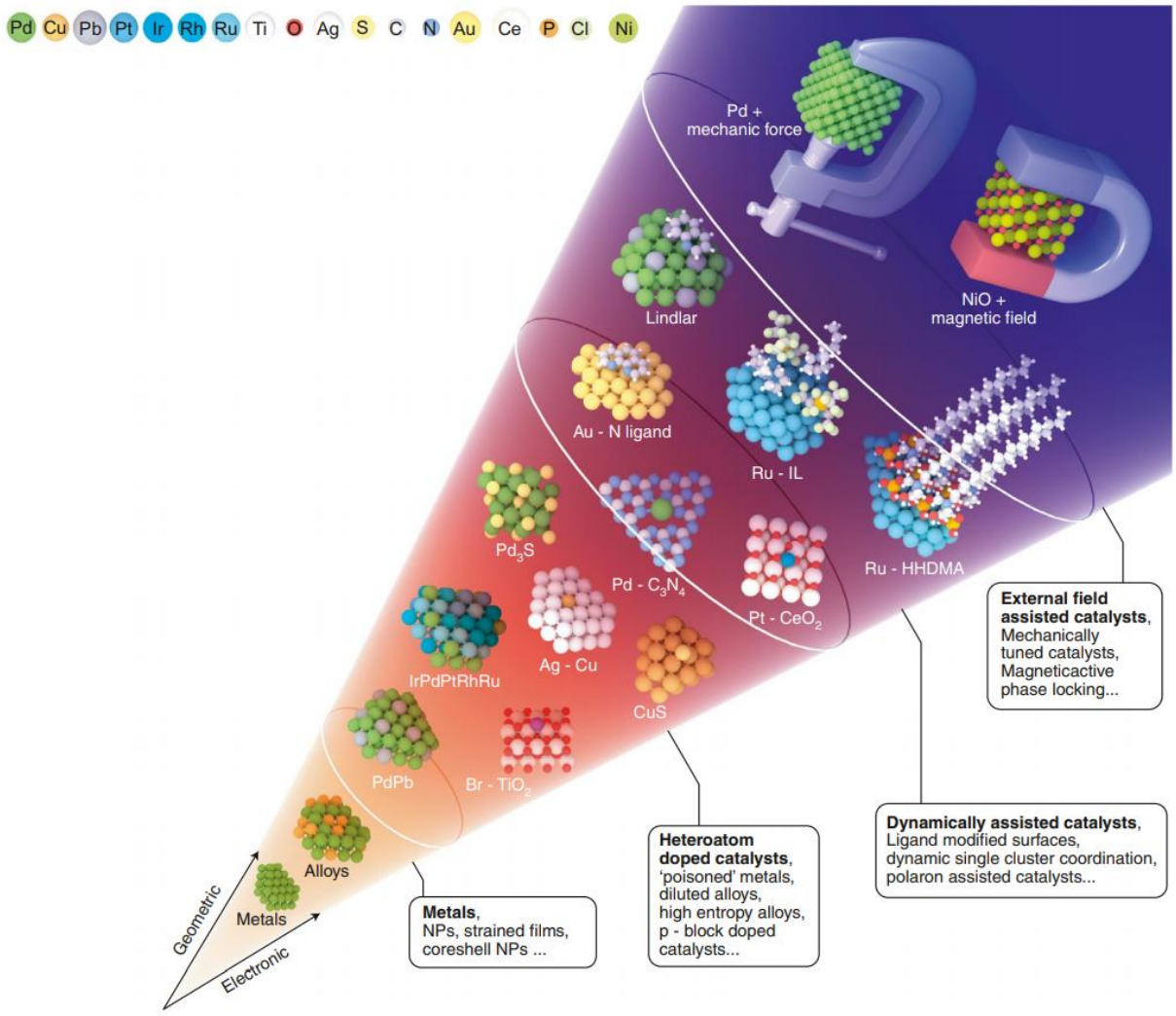

Scheme 4. The cone timeline of breaking linear-scaling relationships strategies.[7]

In terms of complexity, metal-only systems such as metal nanoparticles and metal alloys are located at the lowest level. In the second level of complexity, there are heteroatom doped systems such as metal single atoms in other metals, high entropy alloys, and p-block doped catalysts. The third level is formed by dynamically assisted catalytic systems such as ligand modification systems, organometallic systems, single atoms of the carbon matrix, and polaron-assisted catalytic systems. The highest level includes external field assisted catalytic system, introduction of light, mechanical or magnetic forces to the electrocatalysis as latest works in this area.

1.5 Dual Electrocatalysis

Dual catalysis is a potential method to break linear scaling relationships for achieving high activities in electrocatalysis, if the additional active site in dual active site system is selectively interacted with intermediates. The concept of dual catalysis has been well investigated in the field of organo-catalysis, catalytic chemical transformation by *homogeneous chemo*-catalysts. Appropriately formulated cocktails of multiple catalysts have often shown improved catalytic activities superior to the corresponding single catalyst systems.[8] Proposed mechanisms responsible for the improvement included either (1) associative activation (or double activation catalysis for dual catalysts, **Scheme 5b**), (2) dissociative activation in series (or cascade catalysis, **Scheme 5c**) or (3) dissociative activation in parallel (or synergistic catalysis, **Scheme 5d**). In the associative or double activation of reactant and/or intermediate molecules, multiple catalysts work towards activating a single species in combination.[8-10] In other words, the single species forms a separate chemical bond to each catalyst: e.g., [catalyst A] – intermediate – [catalyst B] where the horizontal lines indicate chemical bonds.

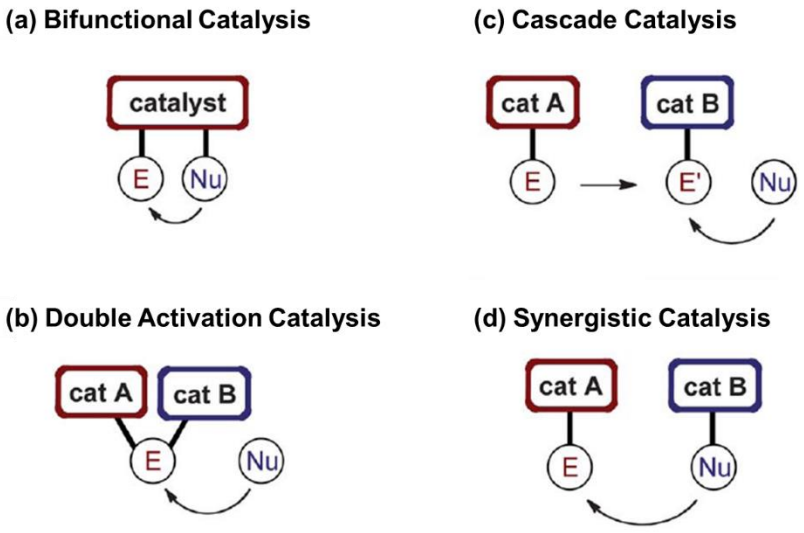

Scheme 5. Classification of homogeneous chemo-catalytic system involving two catalysts. (a) Bifunctional catalysis. (b) Cascade catalysis. (c) Double activation catalysis (d) synergistic catalysis.[8]

As a representative example, the dual catalyst system having tris(dibenzylideneacetone)dipalladium(0) (or $Pd_2(dba)_3$) and chloro(triphenylphosphine)gold(I) (or PPh_3AuCl) improved the catalytic transformation from alkynes to tri- and tetra-substituted olefins.[11] Cationic gold (Au^+) as a Lewis acid clung to the triple bond of alkynes to lower the LUMO energy of the alkynes and then, resultantly promoted the backbonding of palladium to the same triple bond. The bond between carbons of alkyne was concurrently coordinated to both catalysts, Pd and Au^+ (**Scheme 6**).

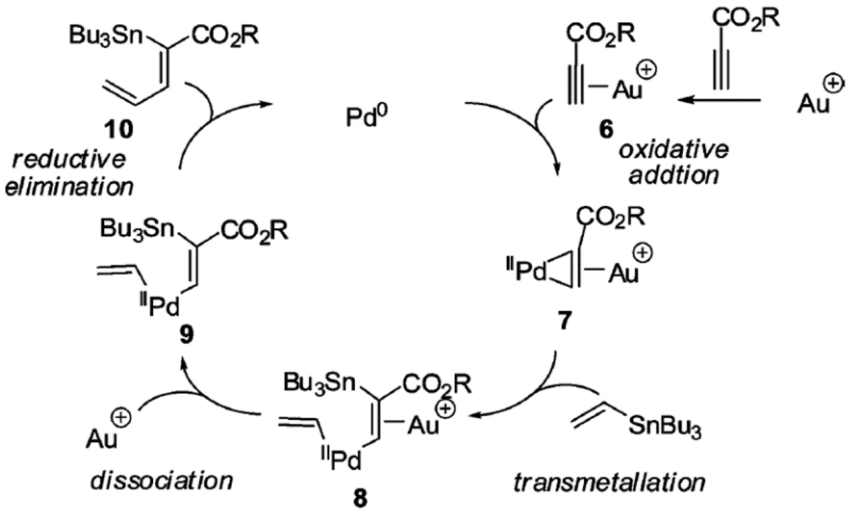

Scheme 6. Proposed mechanism of Gold- and Palladium-cocatalyzed synthesis of Tri- and Tetra-Substituted Olefin.[11]

In the field of *heterogeneous electro*-catalysis, on the other hand, it is difficult to find cases of multiple catalysts co-working to improve catalytic activities. Multi-component catalysts such as bi-metals[12, 13], nitrogen-doped carbons[4], and perovskite oxides modified by dopants[14] do not belong to the multiple catalyst systems. The physicochemical nature of the original active sites was changed by introducing the second-party elements ensuring that the surface species are still bound to a *single* active site. In other words, a second-party element did not provide the additional active site but changed the physicochemical nature of the active site of the original catalyst.

We found an example of the associative (or double) activation catalysis in electrochemical transformation even if the example was not one of a multiple catalyst system. Density function theory

(DFT) calculation expected the catalytic activities of ruthenium oxide for oxygen reduction reaction and oxygen evolution reaction (OER) to be improved only if the gap of nanoscopic channels of the heterogeneous electrocatalyst could be reduced. When the gap between two surface faces of pores was large enough, OOH, as one of the intermediate oxygen species, was attached to either of the surface faces: *OOH; the asterisk(*) indicates where the first oxygen atom is attached to an active site. However, both faces interacted with the OOH to form two bonds (*OO*H, where two bonds (*O and O*) are formed) when the gap becomes narrow enough. Therefore, we consider this work to demonstrate the associative activation of a reaction intermediate in a single *heterogeneous electro*-catalyst system.[15]

Herein, we extend the field of dual catalysis from *homogeneous chemo*-catalysis to *heterogeneous electro*-catalysis. Recently, a dissociative activation catalysis (cascade) using multiple heterogeneous electrocatalysts, SnO_x/Pt-Cu-Ni, was practically reported to promote ORR.[16] However, the same for associative activation catalysis has not been reported yet. Inorganic/organic hybrid dual catalyst systems were presented in this work as the examples of the associative activation electrocatalysis. Cobalt-based oxides were tested as the inorganic electrocatalysts for ORR. A series of polymers was introduced as the second-party organic catalysts to participate in the ORR process. ORR activities of the cobalt-based oxide electrocatalysts were significantly improved by simply mixing the inorganic catalyst particles with the organic catalyst. No sophisticated material engineering of catalysts was involved in developing the intimate interaction between the active sites of catalysts and the HN-CPs. Evidences to support the oxide/polymer dual electrocatalysts activated oxygen species in the associative manner are described in this work.

II. Conductivity-dependent Completion of Oxygen Reduction on Oxide Catalysts

2.1. Abstract

Electric-conductivity dependency of the number of electron transfer of oxygen reduction reaction is presented. Different from extensive properties of electrochemical reactions, intensive properties such as the number of electron transfer are difficult to be considered conductivity-dependent. Four different perovskite oxide catalysts of different conductivities were investigated with carbon varying in contents. More conductive environments surrounding active sites, achieved by more conductive catalysts (providing internal electric pathways) or higher carbon contents (providing external electric pathways), resulted in higher number of electron transfer toward more complete 4e reduction of oxygen and also changed the rate-determining steps from two-step 2e process to a single-step 1e process. The experimental evidences of the conductivity dependency were described by microscopic ohmic polarization model based on effective potential localized nearby the active sites.

2.2. Introduction

Electron conduction to electroactive sites is one of the necessary requirements for electrochemical reactions on electrodes in which the electroactive sites were immobilized. The statement sounds evident when considering a counter-extreme case that an active site embedded in an insulating matrix would not work for electrochemical reactions. Introducing conducting materials such as carbon particles to electrodes has been proved helpful as a support for electrocatalysts in fuel cells (for example, platinum supported by carbon or Pt/C)[17-23] and dye-sensitized solar cells[24] and as a conducting agent for lithium ion battery electrodes[25-28]. It should be carefully considered which factors determining reaction rates or currents are affected by the electron pathway development increasing electron conduction throughout electrodes. Increasing number of electroactive sites (as an extensive property) connected to the electric pathways is probably the primary reason for the reaction rate improvement.[29, 30] Decrease in ohmic loss leading to macroscopic potential drop is the following reason.[31, 32] On the other hand, it is not clear for the electron conduction to affect intrinsic and intensive parameters characterizing electron transfer reactions. Rather, it is difficult to imagine that the standard rate constant (k_o in $k = k_o \exp(-\alpha n F \eta / RT)$ from Butler-Volmer equation; not exchange current i_o) and the number of electron transfer (n) on each active site change with more conductive environments.[33] In this work, we demonstrate the case where the intrinsic parameters of electron transfer varies by tuning electron conduction. The intrinsic and intensive parameters of interest here, which are independent of the number of active sites, are the number of electron transfer for overall process ($n_{overall}$) and rate-determining step (n_{RDS}).

2.3. Results and Discussion

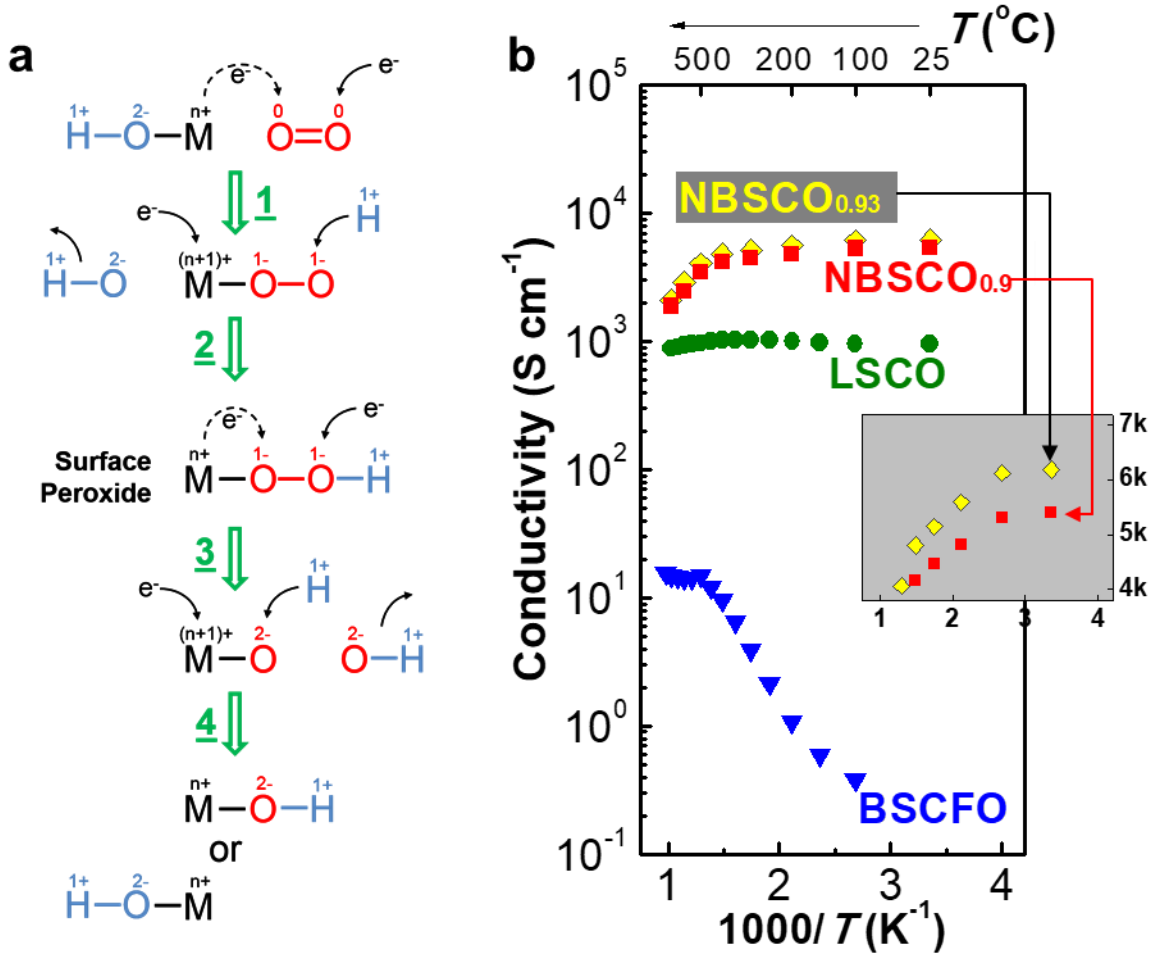

Figure 1. Mechanism of ORR & Conductivities of perovskite catalysts. **(a)** Four one-electron elementary steps constituting ORR on metal active sites (M) of metal oxide catalysts. Solid and dashed arrows with e^- indicate the directions of external and internal electron transfer from potentiostats and the metal active site, respectively. Blue and red colored elements come from electrolyte (0.1 M KOH (aq)) and dissolved oxygen, respectively. Oxidation numbers were indicated on top of the corresponding atoms. **(b)** Electrical conductivities (σ) of perovskite oxide catalysts in Arrhenius plots. Inset: Linear scale conductivity comparison between $NBSCO_{0.9}$ and $NBSCO_{0.93}$ for clarity.

Oxygen reduction reaction (ORR) was selected as a model system because its $n_{overall}$, which is determined by peroxide formation, varies between 2 and 4. The values are determined by configuration of oxygen adsorption depending on nature of active sites of catalysts: 4e for bidentate adsorption versus 2e for end-on (monodentate) configuration on platinum catalysts.[34-39] ORR especially by oxide catalysts consists of four one-electron (1e) elementary steps in series with four surface species on active sites along a turnover track: $-OH^- \rightarrow -OO_2^- \rightarrow -OOH^- \rightarrow -O_2^- \rightarrow -OH^-$ (**Figure 1a**).[34, 40, 41] Dioxygen molecules sit on metal atoms (M) of metal oxide catalysts via the monodentate configuration. The bond breakage of O-O of the surface peroxide (the 2e transfer product formed after the second step in **Figure 1a**) at step 3 is the step determining whether the overall reaction goes via 2e or 4e electron transfer. 4e transfer would be more encouraged if the peroxide intermediate were able to stay on the active sites (M) long enough to go forward to the next species before desorption or if the rate of the steps after the peroxide formation (steps 3 and 4) were faster than that of the previous steps (steps 1 and 2).

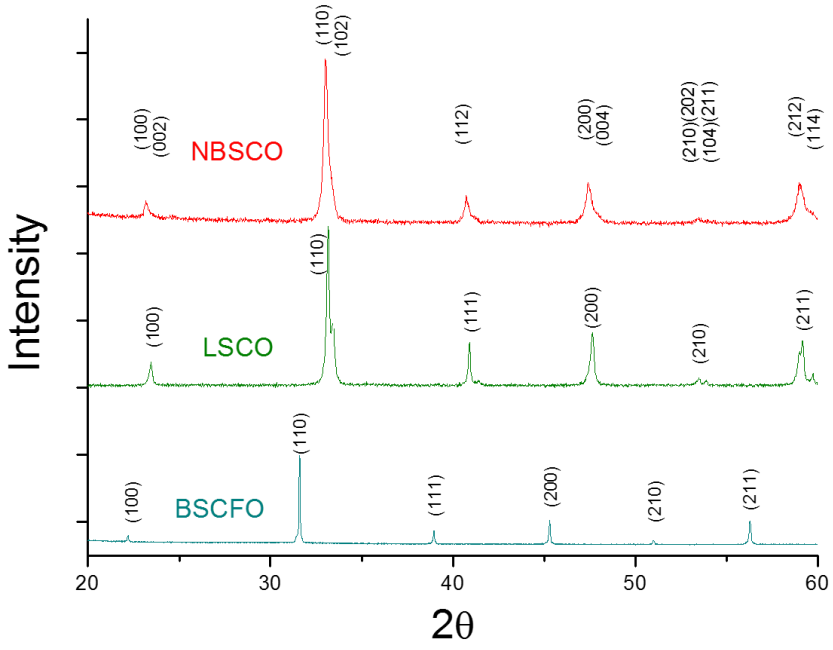

Figure 2. X-ray diffraction patterns of oxide electrocatalysts (BSCFO, LSCO and NBSCO). The patterns were indexed by Rietveld refinement.[42, 43]

Perovskite oxides, recently highlighted as catalysts for oxygen reduction and evolution,[40, 41, 44-56] are the materials proper for investigating the conductivity dependency of intrinsic parameters of ORR because of possible variation of their conductivities. To investigate the conductivity dependency of $n_{overall}$ and n_{RDS}, four different perovskite oxide catalysts having different electron conductivities were prepared: $Ba_{0.5}Sr_{0.5}Co_{0.8}Fe_{0.2}O_3$; BSCFO) at less than 0.4 S cm^{-1} as its room-temperature electron conductivity (σ_{RM}); $La_{0.8}Sr_{0.2}CoO_{0.79}$ (LSCO) at 1000 S cm^{-1}; $NdBa_{0.25}Sr_{0.75}Co_2O_{5+\delta}$ with δ = 0.9 and 0.93 ($NBSCO_{0.9}$ and $NBSCO_{0.93}$) at 5400 and 6200 S cm^{-1}, respectively (**Figure 1b**). BSCFO and LSCO are simple cubic perovskites (ABO3; A = alkaline and/or rare earth metals, B = transition metals) while NBSCOs are double perovskites having alternative layers of different A site elements (Ba (or Sr) and Nd) (**Figure 2**). Metallic conduction of the highly conductive NBSCO is explained by their narrow direct band gaps (E_{gap}) between valence bands (VB) extended above Fermi level (E_F) and conduction bands (CB)[57] (**Figure 3** with detailed discussion; calculation details in Experimental). On the contrary, the poorly conductive counterpart BSCFO showed indirect band gaps characterizing semi-metals and leading to wide direct band gaps.

Degree of ORR completion, indicated by $n_{overall}$, is an important parameter to describe the ORR as a series reaction. The overall current relevant to ORR, which is measured on the disk compartment of rotating ring-disk electrodes (RRDEs), does not result only from the complete reduction of oxygen to hydroxide ions via four-electron (4e; $n_{overall}$ = 4) transfer pathway ($O_2 + 2H_2O + 4e^- \rightarrow 4OH^-$)[58]. Two-electron (2e; $n_{overall}$ = 2) transfer pathway ($O_2 + H_2O + 2e^- \rightarrow HO_2^- + OH^-$) is partly responsible for the ORR current, not completing a turnover of ORR but generating peroxide as an intermediate product. The intermediate HO_2^- was detected by ring electrodes oxidizing the peroxide to oxygen at +0.4 V so that $n_{overall}$ was calculated by comparing between the currents of the disk and ring electrodes (**Figure 6a**). Interestingly, the $n_{overall}$ values (or $\underline{n}_{overall}$ as their average) were estimated higher on more conductive catalyst layers (**Figure 4a-b**). We controlled the electric conduction via internal and external pathways by using catalysts of different conductivities and increasing carbon contents in electrodes. At a fixed carbon content (5 wt. % carbon as a representative), 4e ORR processes were more encouraged by more conductive internal electric pathways resulting from higher conductivities of catalysts: $n_{overall}$ was estimated at 3.9 for the most conductive $NBSCO_{0.93}$ versus at 3.25 for the least conductive BSCFO. However, the difference of $n_{overall}$ between catalysts became smaller as the carbon contents increased (**Figure 4a-b**). The more amounts of carbon developed higher number of external electric pathways with shorter electron travelling length, approaching $n_{overall}$ to 4. With 50 wt. % carbon, therefore, there were no significant differences of $n_{overall}$ between catalysts.

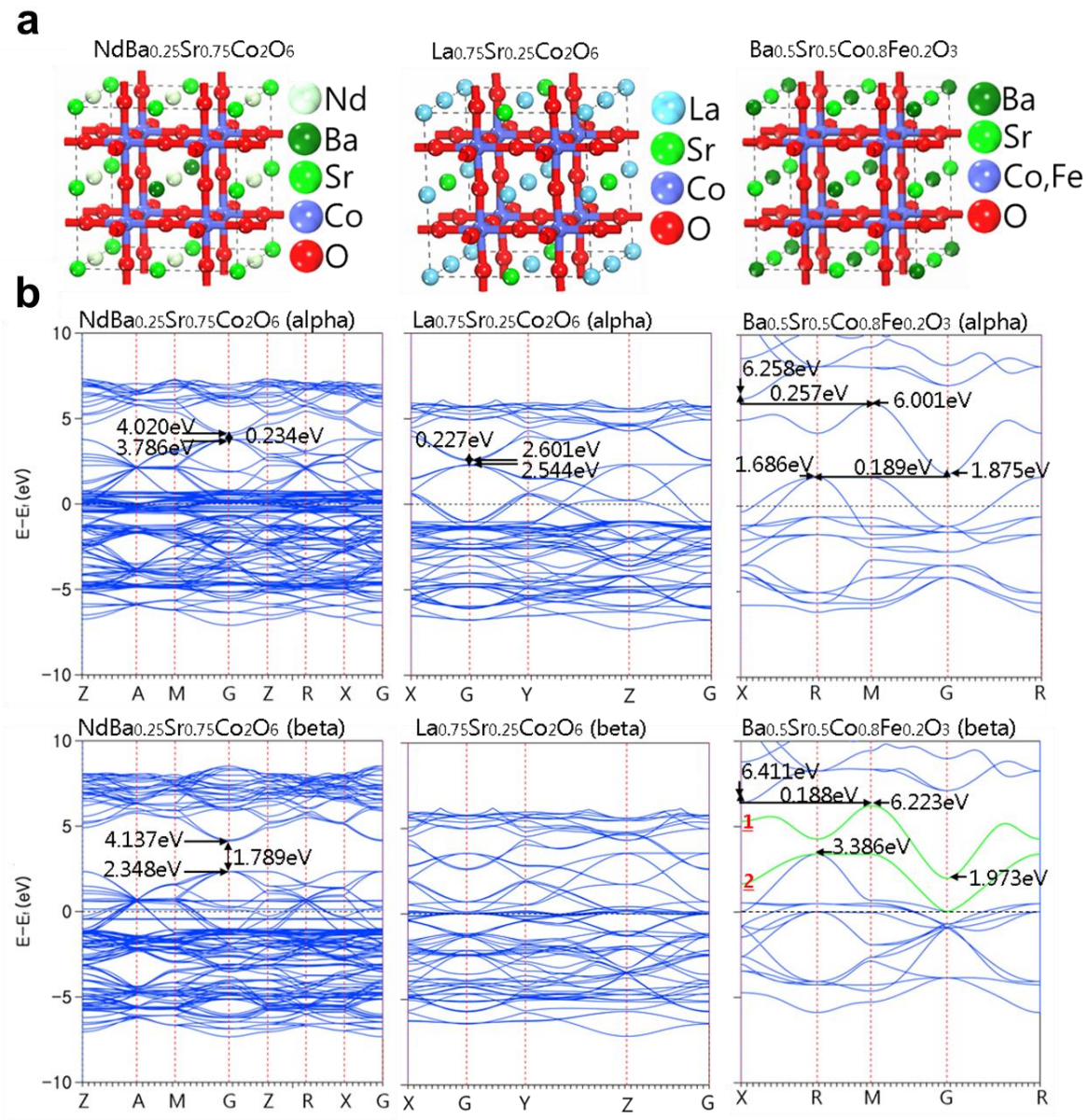

Figure 3. Electronic structures of double and simple perovskites. **(a)** Calculated model systems: $NdBa_{0.25}Sr_{0.75}Co_2O_6$ as NBSCO, $La_{0.75}Sr_{0.25}Co_2O_6$ as LSCO, and $Ba_{0.5}Sr_{0.5}Co_{0.8}Fe_{0.2}O_3$ as BSCFO. **(b)** Spin polarized band structures described by energy states (E) relative to Fermi level (E_F) along K-space vectors.

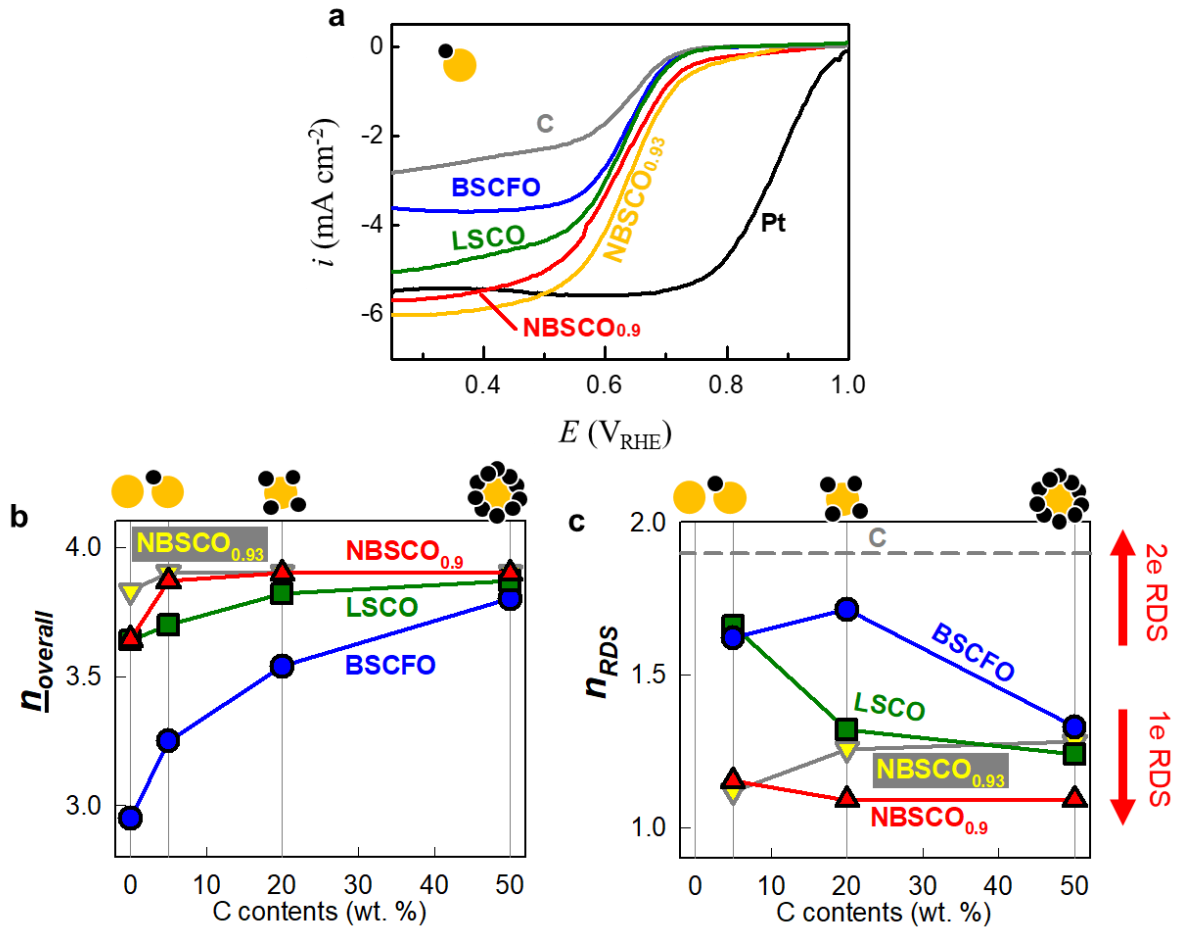

Figure 4. ORR. (a) Voltammograms of disk current of ORR in 0.1 M KOH (aq) at cathodic scan (10 mV sec^{-1}) on 1600 rpm. 5 wt. % carbon was used for BSCFO, LSCO and NBSCO (Loading density, L = 0.8 mg total cm^{-2} with total = oxide + carbon). 80 wt. % carbon was used with Pt (L = 0.4 mg total cm^{-2}). Refer to **Figure 5** for other carbon compositions with the perovskite oxide catalysts. **(b)** Number of electron transfer for overall processes ($\underline{n}_{overall}$). The values of $n_{overall}$ were calculated from currents on disk and ring electrodes along cathodic scan at the same rpm used in (a) during ORR. Its average values ($\underline{n}_{overall}$) were calculated by averaging $n_{overall}$ values at 0.33 V and 0.53 V. **(c)** Number of electron transfer for rate determining step (n_{RDS}). The values of n_{RDS} were calculated from Tafel slopes (b) by using the relationship: b = 60 mV dec^{-1}/ (n_{RDS} α) where transfer coefficient (α) was assumed to be 0.5. A single catalyst particle (yellow circle) surrounded by multiple carbon black (black circles) were schematically illustrated corresponding to their carbon compositions on the top of (b) and (c).

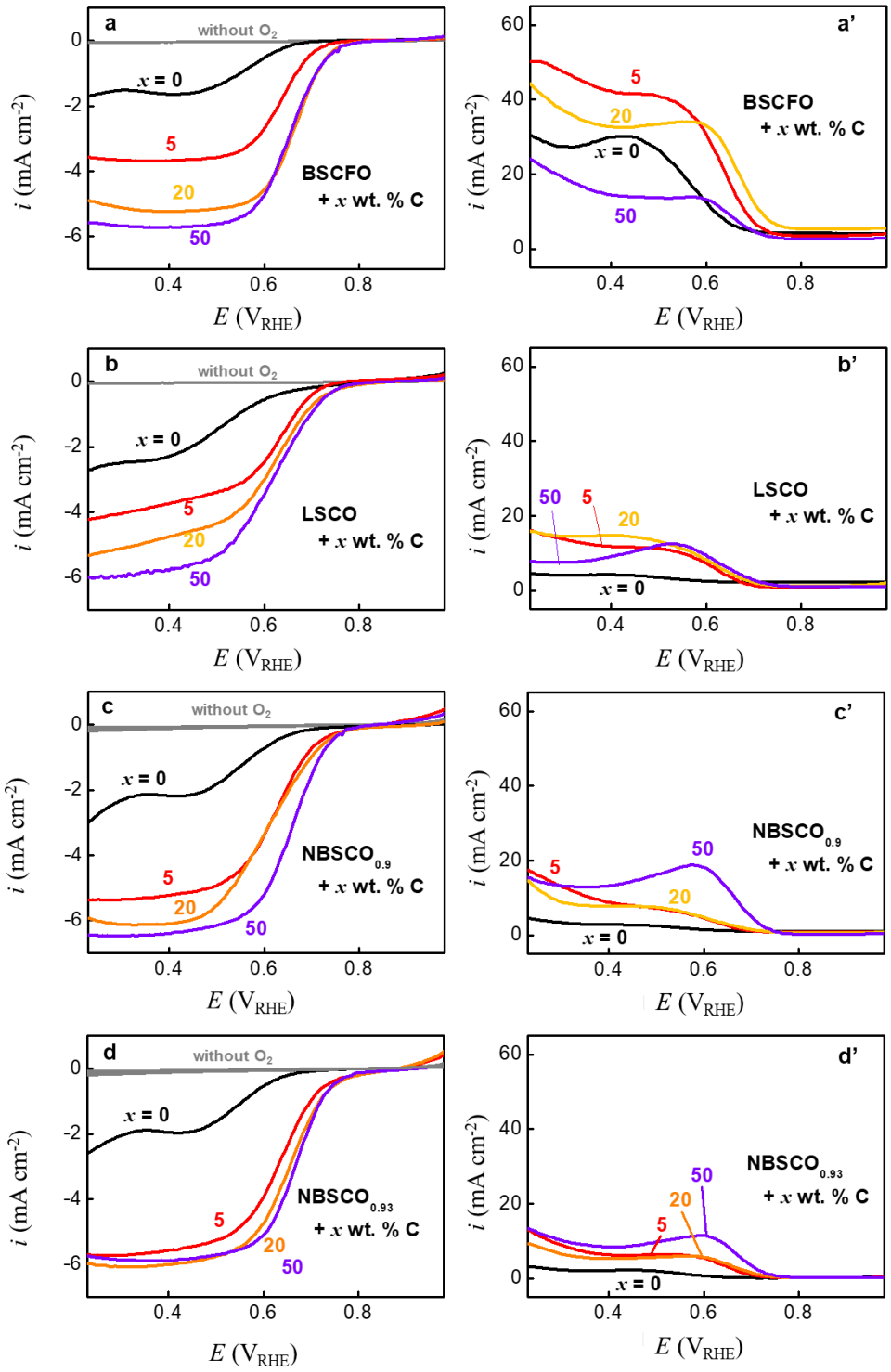

Figure 5. Voltammograms of disk **(a to d)** and ring **(a' to d')** currents of ORR in 0.1 M KOH (aq) at cathodic scan (10 mV sec^{-1}) on 1600 rpm in the presence of perovskite oxide catalysts (Loading density, L = 0.8 mg total cm^{-2} with total = oxide + carbon; disk area = 0.1256 cm^2). Background currents were presented in the presence of nitrogen without oxygen (grey solid lines). The background currents were estimated negligible when compared with ORR currents for all carbon contents.

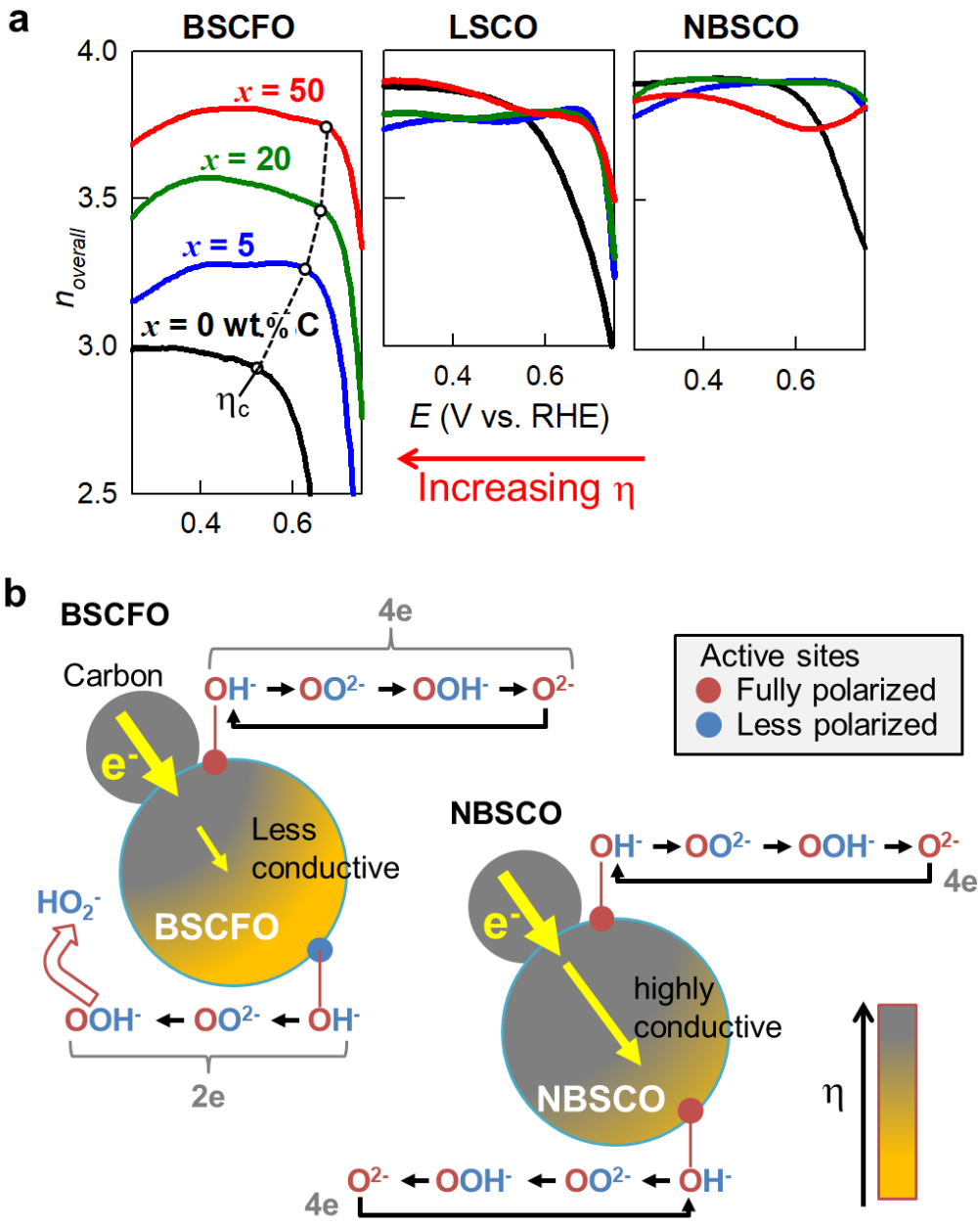

Figure 6. The effects of local potential distribution nearby the active sites on $n_{overall}$. **(a)** Potential dependency of $n_{overall}$. The critical overpotentials (η_c) at which the $n_{overall}$ dramatically decreases were indicated. **(b)** BSCFO and NBSCO as representative examples of less versus more conductive catalysts, respectively. Overpotential (η) gradients are decreasingly developed along a direction away from the contact point with carbon through the body of catalyst.

The conductivity-dependent contribution of 4e or 2e process to the overall currents on the perovskite oxide catalysts could be understood from the viewpoint of effective potential localized nearby active sites. The values of $n_{overall}$ (c.f. $\underline{n}_{overall}$ is the average value of the $n_{overall}$ between 0.33 V and 0.53 V) depended on overpotential (η) (**Figure 6a**): the higher η (or the more negative potential) resulted in the larger $n_{overall}$. Even if the overpotential dependency trend was consistent over all samples, the critical overpotential (η_c) at which the $n_{overall}$ began to decrease dramatically shifted in the direction to higher η (or more negative potential) from 0.65 V to 0.52 V with decreasing carbon contents in the most resistive BSCFO. However, more conductive catalysts (LSCO and NBSCO) showed no significant change in η_c with carbon contents except of 0 wt. % C. It indicates that more resistive situations caused by resistive catalysts and/or small carbon contents have ohmic potential drop developed and require higher overpotential to complete the 4e reaction.

Based on the overpotential dependency of $n_{overall}$, the catalytically active sites of low-conductivity perovskite catalysts (e.g., BSCFO) can be schematically categorized into fully and less polarized sites (**Figure 6b**). Both sites benefit from the kinetic gain by the catalytic activation energy reduction. The fully polarized sites, experiencing high η and completing the 4e pathway, are physical points at which electric pathways provided by carbon meet the catalyst surface with the chemical species including O_2. They are found nearby the contact points between carbon black and catalyst. The less polarized sites, on the BSCFO surface without contact to external electric pathway or far from the contact points between carbon and catalyst, experience small η for ORR in the catalyst-side space charge region nearby the electrolyte-catalyst interface due to the resistive electron pathways throughout BSCFO to them. Therefore, peroxide ions are significantly produced from the less polarized sites before completing the overall 4e turnover probably because the small η causes the rate of the steps after the peroxide formation (steps 3 and 4) to be kinetically slow (**Figure 1a**). The surface peroxide is desorbed kinetically when its stay on an active site is longer than its possible retention time. The discussion is supported by the experimental fact that higher carbon contents of BSCFO-based electrodes increased $n_{overall}$ from 3.25 with 5 wt. % carbon to 3.8 with 50 wt. % carbon (**Figure 4b**). On the other hand, all active sites of our highly conductive NBSCO have η high enough to proceed ORR efficiently along the 4e pathway with high $n_{overall}$ values even at low carbon contents. Insignificant change in $n_{overall}$ value with increasing carbon contents supports that electrons are supplied to the surface efficiently through the NBSCO even without external electron pathways (**Figure 4b**).

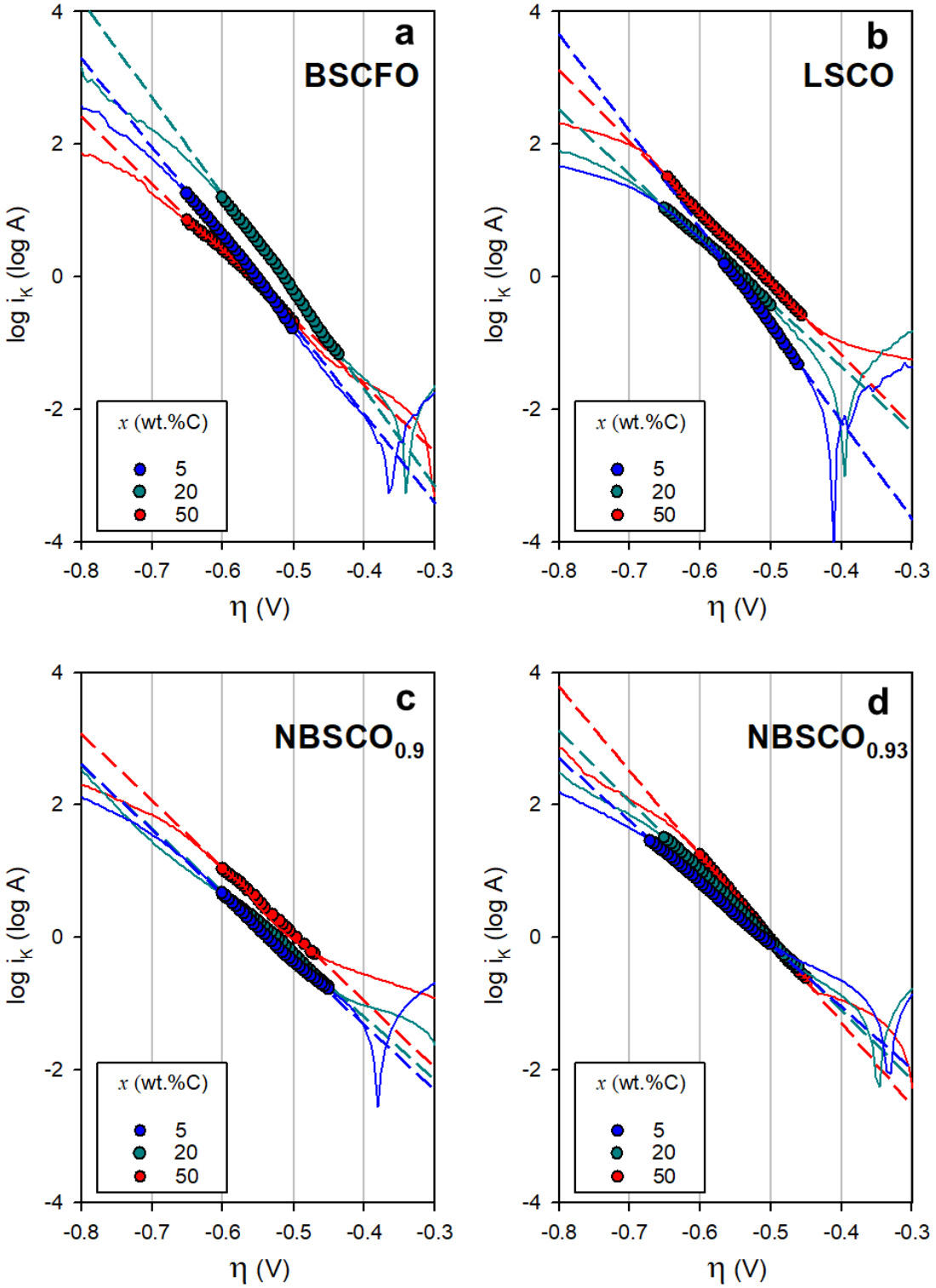

Figure 7. Tafel plots of ORR polarization: solid lines = all experimental data; symbols = data points used for obtaining Tafel slope b (mV dec^{-1}); dashed lines = linear regression lines fitting symbols.

In addition to $n_{overall}$ as a measure of ORR completion, n_{RDS} provides information on the number of electron transfer not for the overall ORR process but specifically for RDS.[59-62] Its values are calculated from Tafel equation (**Figure 7**): $\eta = a + b \log i$ where $a = \ln i_o /(\alpha n_{RDS} f)$ and $b = -2.3 /(\alpha n_{RDS} f)$ with $f = F/RT$ (Supporting information for glossary of symbols). The ORR was assumed to be symmetric, that is to say, $\alpha = 0.5$ to obtain n_{RDS}.[63] Interestingly, n_{RDS} changed with electrode conductance depending on catalyst conductivities as well as carbon contents (**Figure 4c**). The most conductive double perovskites ($NBSCO_{0.9}$ and $NBSCO_{0.93}$) showed small values of n_{RDS} closer to 1 rather than 2 (less than 1.5) for all carbon contents from 5 wt. % to 50 wt. %. In the medium-conductivity perovskite LSCO, on the other hand, its RDS at the lowest carbon content (5 wt. C) was identified more as 2e transfer and then the n_{RDS} changed from 2e to 1e around 20 wt. % C. In the least conductive BSCFO, the n_{RDS} transition was observed at higher carbon contents from 50 wt. %. That is to say, the more conductive catalyst layers are, the closer to 1e process the RDS is.

Based on experimental facts for $n_{overall}$ and n_{RDS}, therefore, 1e transfer RDS appears to be responsible for 4e ORR. The conclusion coincides with what the local electron population scenario says as discussed above. Both or either of two elementary steps of **1** and **4** (**Figure 1a**), each from steps before and after peroxide formation, were known to be highly possible RDS.[40, 41] In low-conductivity catalysts with poorly conductive environments, both of them is thought to be RDSs because n_{RDS} was estimated at 2. The latter RDS at step **4** would play a crucial role of peroxide generation by delaying forward conversion of surface peroxide to the next surface species. However, there is a single RDS ($n_{RDS} = 1$) with no RDS after the peroxide formation (that is to say, RDS at **1**; and $n_{RDS} = 1$) in highly conductive catalysts and even in poorly conductive catalysts surrounded by highly conductive environments so that most of oxygen is completely reduced via 4e process.

From a standpoint of electronic structure, the double perovskites (NBSCO, PBSCO and NBCO) had direct band gaps (E_{gap}) whereas the simple perovskite had an indirect band gap. More importantly, multiple band states were found above Fermi levels (E_F) in the double perovskites, being extended to or overlapped *directly* with valence band states below E_F[57]. Free carriers generated in the extended and delocalized states are responsible for metallic conduction. Considering that conduction carrier density in metal is proportional to $E_F^{3/2}$, which material has higher conductivity (σ) could be expected from the values of E_F. The decreasing order of σ (**Figure 1**) follows the same order of E_F: NBSCO (E_F = 3.153 eV) > PBSCO (E_F = 3.109 eV) > NBCO (E_F = 2.207 eV) > BSCFO (E_F = 0.732 eV). However, BSCFO is semi-metallic unlike the double perovskites. An energy band state (indicated by **1** in b) is not overlapped with the extended valence band even if its minimum energy is lower than the maximum energy of the topmost band state (**2**) of the extended valance band. The *indirect* overlap, characteristic of semi-metals, leads to poor conductivities with semi-conductor behavior of temperature dependency

of σ^{64}. Also, a more dilute density of states of BSCFO than the double perovskites is expected from its smaller number of band states.

2.4. Experimental

Material Preparation. Perovskite oxide catalysts (BSCFO, LSCO and NBSCO) were synthesized by sol-gel method. Stoichiometric amounts of precursors ($Nd(NO_3)_3 \cdot 6H_2O$, $Ba(NO_3)_2$, $Sr(NO_3)_2$, $Co(NO_3)_2 \cdot 6H_2O$, $Fe(NO_3)_3 \bullet 9H_2O$ and $La(NO_3)_3 \cdot 6H_2O$) were dissolved in distilled water with proper amount of Pluronic F-127. All chemicals were used as received from Aldrich. The solution was dried in the oven at 100 ºC for one day. The precursor gel was heated up to 300 ºC in air. Fine powders obtained during the combustion were calcined at 600 ºC for 4 h and then annealed in air at 950 ºC for 4 h. For measuring intrinsic electrical conductivity, the powder was pressed into pellets at 5 MPa and sintered in air at 1100 ºC for 12 h instead of the thermal treatment at 950 ºC for 4 h to achieve a relative density higher than 95 %. There were no significant differences of crystallographic structures and oxygen non-stoichiometry between the powder samples annealed at 950 ºC and the pellet samples sintered at 1100 ºC. The value of δ of the as-synthesized NBSCO ($NdBa_{0.25}Sr_{0.75}Co_2O_{5+\delta}$ with = 0.9) was tuned from 0.9 to 0.93 by thermal treatment at 800 ºC for 4hr in oxygen atmosphere.

Physicochemical characterization. The elemental compositions of perovskite materials were characterized by inductively coupled plasma atomic emission spectroscopy (ICP-AES). Their oxygen non-stoichiometry (δ) was measured by iodometric titration.[43] The crystallographic structures of materials were characterized at a scan rate of 0.6 degree min^{-1} with the 2θ range of 20 º to 60 º by X-ray diffraction (XRD; Rigaku diffractometer D/MAZX 2500V/PC with Cu K radiation). Electrical conductivities were measured in air by a four-point probe configuration. Ag wires as probes were connected to samples by Ag paste. The current/voltage was controlled/measured by a potentiostat (BioLogic VMP3) in a temperature range of 25 to 700 ºC.

Electrode preparation. Catalyst inks were prepared by dispersing a catalyst and a conducting agent in 0.45 ml of ethanol, 0.45 ml of isopropyl alcohol and 0.1 ml of 5 wt. % nafion solution (Sigma-Aldrich 274704). The total amount of the catalyst and the conducting agent was fixed at 20 mg. Carbon black (C; Akzo Nobel Ketjenblack 600JD) was used as the conducting agent at 0, 5, 20 and 50 wt. %. 5 ul of the catalyst ink was dropped on the disk compartment of ring-disk electrodes. Loading density of the composite of catalyst and conducting agent was fixed at 0.8 mg cm^{-2}. For comparison, 20 wt. % platinum nanoparticles supported by carbon black (Pt/C; Premetek P10A200) was used as a control.

Electrochemical characterization. Cyclic and linear sweep voltammograms (CVs and LSVs) were obtained on disk and ring electrodes simultaneously by a bipotentiostat (iviumstat, Ivium Technologies). Ring-disk electrodes (RRDE) of glassy carbon disk and platinum ring was used as the working electrode (disk area = 0.1256 cm^2) while a platinum wire and a Hg/HgO electrode were used as the counter and reference electrodes respectively. The RRDEs were rotated at various controlled speeds (1600 rpm

unless otherwise indicated) by a RRDE controller (ALS RRDE-3A). An aqueous solution of 0.1M KOH was used as the electrolyte. ORR polarization curves were obtained on the disk electrode from a cathodic sweep from +0.1 V to -0.7 V (vs. Hg/HgO) at 10 mV s^{-1} after five cycles of CVs. The electrolyte was saturated by oxygen for ORR while it was purged by nitrogen to measure background currents. +0.4 V was applied to the ring electrode to estimate the amount of peroxide generated from the disk electrode. The polarization curves were selected at the 5th scan of voltammetry after confirming that the voltammograms did not significantly change during the initial ten cycles. The ORR stability of the perovskite oxide catalysts used in this work were guaranteed by the long term cycle tests (**Figure 8**). The values of potential were converted from versus Hg/HgO to versus the reversible hydrogen electrode (RHE) by: Hg/HgO + 0.929 V = RHE. For the correction, the potential difference between Hg/HgO and RHE was measured in a cell where platinum wires were used as the working and counter electrodes in a hydrogen-saturated aqueous electrolyte of 0.1 M KOH with Hg/HgO as the reference electrodes. The open circuit potential was read at -0.929 V vs. Hg/HgO from a LSV at 1 mV s^{-1} (**Figure 9a**).

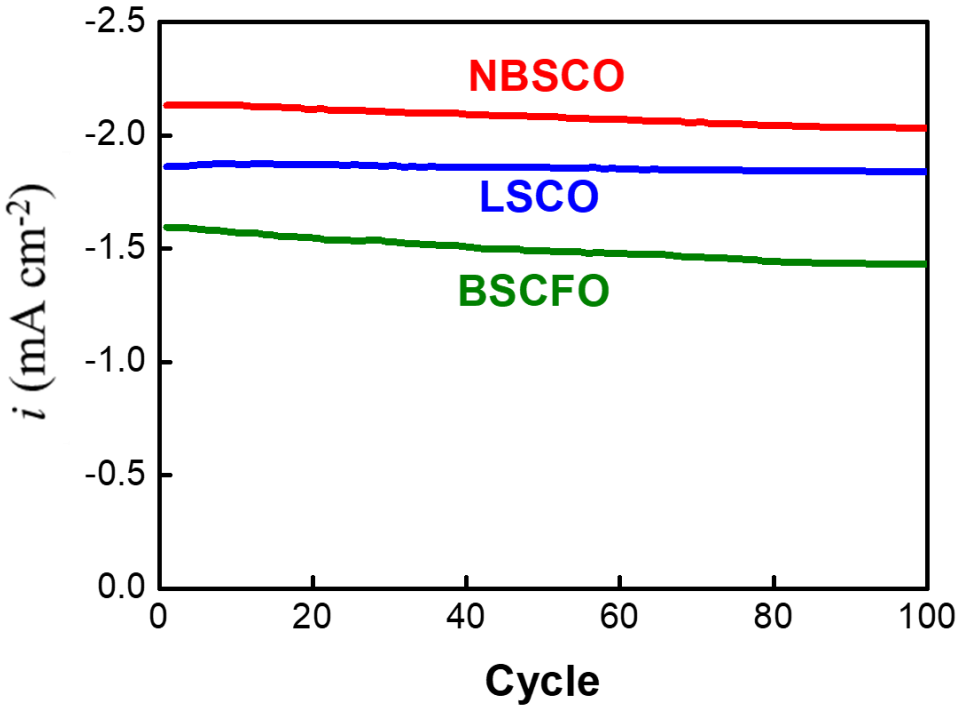

Figure 8. ORR cyclability test. Disk currents at +0.68 V vs. RHE were recorded along cycles at which potential was scanned at 50 mV s^{-1} between +0.2 V and +1 V vs. RHE.

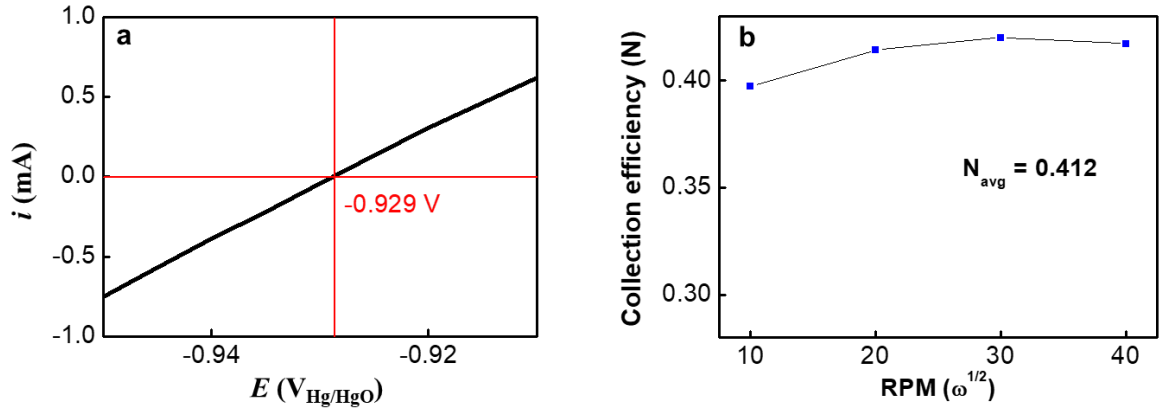

Figure 9. RHE calibration and Collection efficiency. (**a**) RHE calibration. Pt wires were used as working and counter electrodes while Hg/HgO was used as a reference electrode. The potential was swept at 1 mV s^{-1} in H_2-saturated 0.1 M KOH (aq). The open circuit potential was measured at -0.929 V vs. Hg/HgO. (**b**) Collection efficiency (N). $Fe(CN)_6^{3-}$/ $Fe(CN)_6^{4-}$ was used as a reversible redox couple for the measurement.

Number of electron transfer (n). The disk currents (I_d or i_{disk}) result from both 4e and 2e ORR processes. Hydrogen peroxide (HO_2^-) is produced only from the 2e ORR process, which is detected on the ring electrode (as I_r or i_{ring}) by re-oxidizing the hydrogen peroxide. Therefore, both n and the amounts of peroxide production (HO_2^- %) are determined by comparing the values of I_d and I_r at the same moment via the following equations:

$$n = 4\frac{I_d}{I_d+\frac{I_r}{N}} \qquad \text{(S1)}$$

$$HO_2^-(\%) = 200\frac{\frac{I_r}{N}}{I_d+\frac{I_r}{N}} \qquad \text{(S2)}$$

where N is the collection efficiency as a measure of a fraction of hydrogen peroxide produced on disk electrode to be detected on ring electrode. The value of N for the RRDE we used was measured by using 10 mM aqueous electrolyte of potassium ferricyanide ($K_3[Fe(CN)_6]$) in 0.1M KOH in a three electrode configuration (RRDE as the working electrodes, Pt wire as the counter electrode and Hg/HgO as the reference). The disk potential was swept from 0.6 V to -0.5 V at various rotating speeds while the ring potential was fixed at 0.6V. The N value estimated by the ratio of the limiting ring current to the limiting disk current was determined at 0.412 (**Figure 9b**), which was close to 0.424 that is the theoretically calculated value based on the dimension and geometry of our RRDE.

Simulation models. Cambridge Serial Total Energy Package (CASTEP)[65] is used to calculate NBSCO ($NdBa_{0.25}Sr_{0.75}Co_2O_6$), PBSCO($PrBa_{0.25}Sr_{0.75}Co_2O_6$), NBCO($NdBaCo_2O_6$) and

BSCFO($Ba_{0.5}Sr_{0.5}Co_{0.8}Fe_{0.2}O_3$) spin-polarized electronic properties in this study. The cell size of 2×2×2 is used for NBSCO, PBSCO and NBCO. The cell symmetry of NBSCO, PBSCO and NBCO is P4/MMM. Generalized-gradient approximation (GGA) with Perdew, Burke and Ernzerhof (PBE)[66, 67] functional and ultrasoft pseudopotential[68] are used. The Broyden–Flecher–Goldfarb–Shanno (BFGS) algorithm[69] is used for the geometry optimization. NBSCO and PBSCO are optimized with fixed lattice parameter and NBCO is optimized with unfixed lattice parameter with 500GPa of compressibility since NBCO was made by changing Sr atom to Ba atom in NBSCO. For geometry optimization, convergence thresholds for the maximum energy change were set to be 1×10^{-5} eV/atom (for fixed lattice) and 5×10^{-5} eV/atom (for unfixed lattice). Convergence thresholds for maximum force, stress, and displacement were set to be 0.03 eV/Å, 0.05 GPa, and 0.001 Å, respectively. The energy cutoff was set to be 500 eV for the fixed lattice parameter and 400 eV for optimizing lattice parameter. Convergence tolerance for the single atomic energy was set to be and 1×10^{-5} eV/atom. The sampling of the Brillouin Zone[66] was done with the Monkhorst-Pack scheme[70] and for the integration, the number of *k* points of 2×2×2 were used. For BSCFO, the perovskite unit cell was used with the mixed atom method and its symmetry was PM3M. Lattice parameters were fixed and other calculation method were same as fixed lattice system except for *k* points set (i.e. 4×4×4).

Glossary of Symbols

- Levich equation: $i_L = 0.62\ n\ F\ A\ D\ O^{2/3}\ \omega^{1/2}\ \nu^{-1/6}\ C_O*$

  i_L = limiting current; n = overall electron transfer number; F = Faraday constant (96,487Cmol^{-1}); A = geometric area of electrodes; D = diffusion coefficient of oxygen; C = concentration of O_2 in the aqueous solution (mol L^{-1}); ν = kinematic viscosity of electrolyte (0.01 cm s^{-1}); ω = electrode-rotation rate (rpm).

- Tafel equation: $\eta = a + b \log i$

  $a = \ln i_o / (\alpha\ n_{RDS}\ f)$; $b = -2.3 / (\alpha\ n_{RDS}\ f)$; $f = F/RT$; η = overpotential; i = current; i_o = exchange current; n_{RDS} = number of electron transfer in RDS; α = transfer coefficient, R = ideal gas constant (8.314 J/mol K); T = absolute temperature (K).

2.5. Conclusions

In this work, we presented conductivity-dependency of the number of electron transfer for ORR and its RDS. Whether electric conduction throughout electrodes is improved internally by using high-conductivity catalysts or externally by adding conducting agents such as carbon black, completion of ORR via 4e transfer was more encouraged in more conductive situations by one-step 1e RDS before surface peroxide formation. This is the most direct or the first observation, to the best of our knowledge, showing that intensive and intrinsic properties of electrochemical reactions possibly depend on electric conduction that have been easily thought to affect extensive properties such as effective amount of electroactive sites. From the conclusion, electric conductivities of electrocatalysts should be more seriously considered to obtain higher energy densities in electrocatalysis-based energy devices such as fuel cells and metal air batteries.

III. Secondary amine-conjugated polymer-assisted oxygen reduction reaction on cobalt-based oxides

3.1. Abstract

Nitrogen-containing electrocatalysts such as metal-nitrogen-carbon (M-N-C) composites and nitrogen-doped carbons are known to exhibit high activities for oxygen reduction reaction (ORR). Even if the mechanism by which nitrogen improve the activities is not completely understood, strong electronic interaction between nitrogen and active sites has been found in these composites. Herein, we demonstrate a case in which nitrogen improves electroactivity, but in the absence of strong interaction with other components. The overpotentials of ORR and oxygen evolution reaction (OER) on perovskite oxide catalysts were significantly reduced simply by mixing the catalyst particles with polypyrrole/carbon composites (pPy/C). Any strong interactions between pPy (a nitrogen-containing compound) and active sites of the catalysts were not confirmed. A scenario based on the sequential role allocation between pPy and the oxide catalysts for ORR was proposed: (1) molecular oxygen is incorporated into pPy as a form of superoxide ($pPy^{+}O^{2-}$); (2) the superoxide is transferred to the active sites of perovskite catalysts; and (3) the superoxide is completely reduced along 4e ORR process.

3.2. Introduction

Oxygen-related electrochemistry is important for next-generation energy conversion and storage. Oxygen reduction reaction (ORR) is used as the cathodic processes of fuel cells and metal air batteries for generating electricity.[71-75] Its reverse reaction, oxygen evolution reaction (OER), is the anodic processes for splitting water and charging process of metal air batteries.[76, 77] High reversibility between ORR and OER should be guaranteed in rechargeable metal air batteries[72-75] while fuel cells and water splitting are based on either forward or backward reaction of the oxygen-to-water conversion. Platinum has been known as the best ORR catalyst while the oxide layer formed on its surface at oxidative conditions deteriorates the catalytic activity for OER seriously.[78-80] Iridium or ruthenium oxides have been regarded as the best OER catalysts.[81] However, their electrocatalytic activities of ORR are not as high as those of OER, significantly inferior to other catalysts. Iridium alloys with transition metals, as another form of iridium-containing catalysts (not the oxide form), catalyzed ORR efficiently while any forms of ruthenium did not work as the ORR catalysts.[82] It is challengeable to develop a catalyst with high electroactivities for both ORR and OER.

Perovskite oxides have been studied as catalysts for the oxygen-related electrochemistry. Simple perovskite oxides (ABO_3; A = alkaline and/or rare earth metals, B = transition metals) were suggested as mono-functional catalysts for OER or ORR[40, 41, 49] and bi-functional catalysts[46-48]. Material candidates were extended from the simple perovskites to double or layered perovskites. A series of double perovskites were reported more stable during OER than their simple perovskite counterpart BSCF ($Ba_{0.5}Sr_{0.5}Co_{0.8}Fe_{0.2}O_{2.59}$).[49] Even though the perovskite series have been studied extensively, their ORR activities are still lower than those of other catalysts such as N-doped carbons. Improvement in the ORR electroactivity is required for guaranteeing the bifunctionality and reducing the potential gap between ORR and OER.

In this work, two different perovskite oxides were used as bifunctional catalysts for both ORR and OER in alkaline media at room temperature: BSCF as a simple perovskite and NBSC as a double perovskite ($NdBa_{0.25}Sr_{0.75}Co_2O_{5.9}$ in **Figure 10**).[83] The particle sizes of both oxides were controlled similar or identical at 400 to 500 nm (c.f., Ketjenblack at ~30 nm). The conductivities at room temperature were 0.25 S cm^{-1} for BSCF and 5400 S cm^{-1} for NBSC.

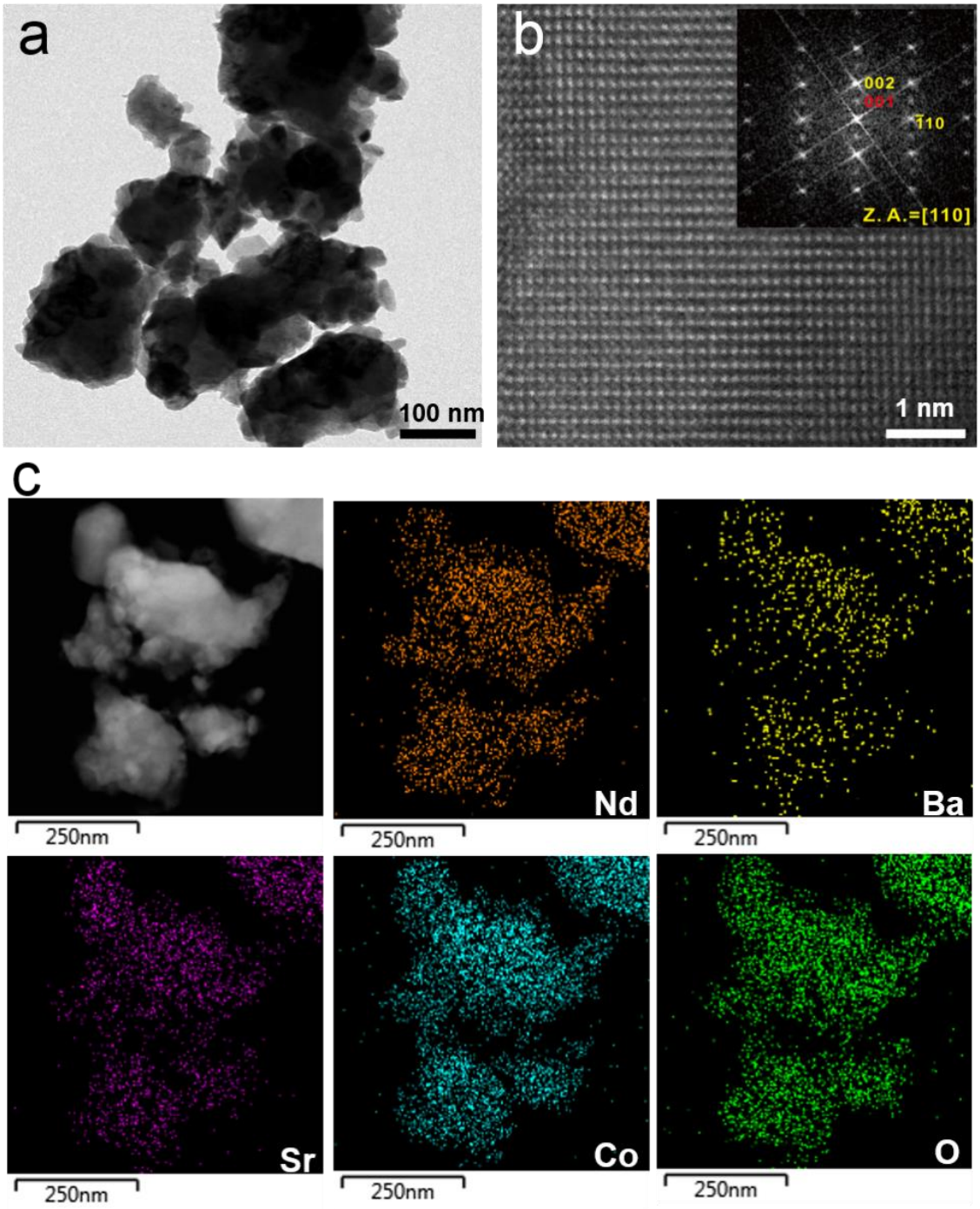

Figure 10. Electron-microscopic characterization of NBSC. **(a)** A TEM image at low magnification. **(b)** A TEM image at high magnification with its fast Fourier transformed pattern. Spots of weak intensity in the pattern were observed when electron beam was introduced in a [110] direction. They are indexed with (001) of a tetragonal super lattice, indicating the double perovskite structure. **(c)** Element mapping by energy dispersive spectroscopy (EDS). Each component was uniformly distributed throughout particles.

3.3. Results and Discussion

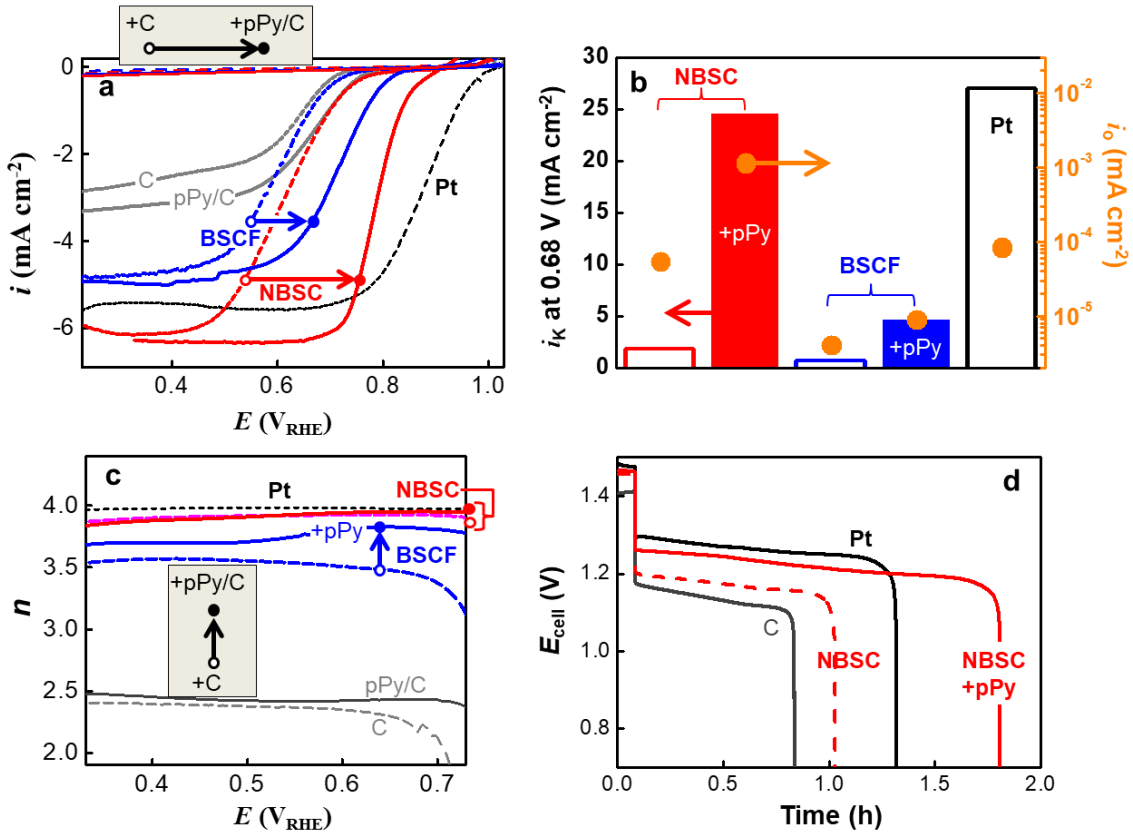

Figure 11. ORR **(a)** ORR polarization in 0.1 M KOH (aq) at cathodic scan (10 mV sec^{-1}) on 1600 rpm. C (Ketjenblack EC-600JD) or pPy/C was used at 20 wt. % with perovskite oxide catalysts (NBSC or BSCF). Open and solid circles on curves means +C and +pPy/C, respectively. Pt/C = Pt + 80 wt. % C. Loading density (L in mg_{total} cm^{-2} with total = oxide + carbon) = 0.8 for the perovskite catalyst layers and 0.4 for C and pPy/C. Baselines obtained from N_2-purged electrolyte for each sample were included. **(b)** Kinetic current densities (i_K) at 0.68 V_{RHE} and exchange current densities (i_o). **(c)** Number of electron transfer (n). **(d)** Potential profiles for the galvanostatic discharge at 20 mA cm^{-2} in zinc-air batteries. The ORR and OER polarization curves were obtained reproducibly (**Figure 12**).

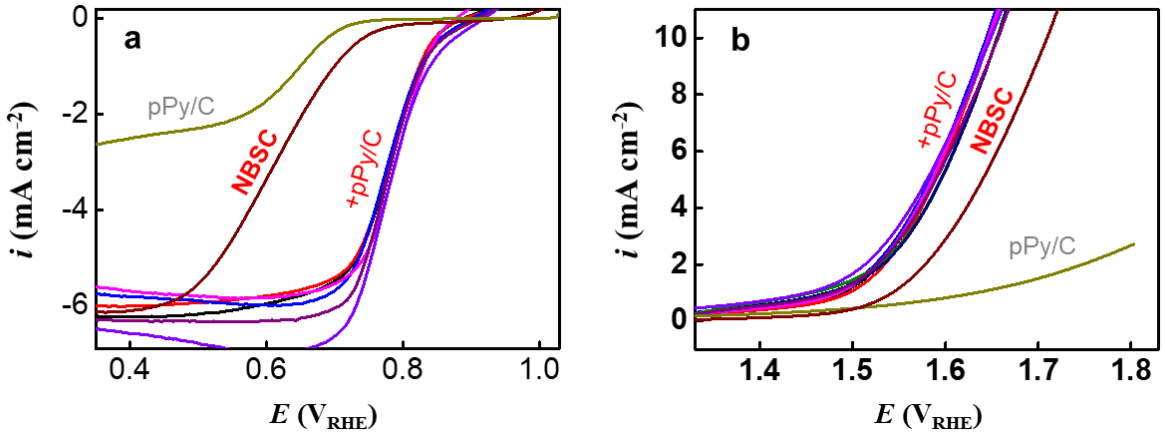

Figure 12. Reproducibility of the NBSC+pPy/C performances. **(a)** ORR polarization in 0.1 M KOH (aq) at cathodic scan. **(b)** OER polarization in 0.1 M KOH (aq) at anodic scan. Scan rate = 10 mV sec^{-1}. Rotation speed = 1600 rpm.

A significant but limited improvement in ORR and OER kinetics was achieved by NBSC when the NBSC was compared with BSCF (**Figure 11**). The polarization difference between the perovskite oxide catalysts would be due to the difference in the electronic environments surrounding cobalt active sites and their conductivities. The ORR onset potential of the highly conductive NBSC (E_{onset}; defined as the potential at -0.1 mA cm^{-2} in this work) was shifted in the more positive direction (or in the less overpotential direction) by +50 mV from that of the poorly conductive BSCF (**Figure 11a**). The exchange current density (i_o) of NBSC (calculated via Tafel equation) was estimated at 5.26 x 10^{-5} mA cm^{-2}, which is six times as high as that of BSCF (**Figure 11b**). The kinetic current densities (i_k calculated by Koutechy-Levich equation) at 0.68 V (all potentials here were reported versus RHE) was 1.81 mA cm^{-2} for NBSC, which is more than twice that of BSCF. Therefore, the double perovskite is obviously superior to its simple perovskite counterpart from a kinetic standpoint of ORR activity even if NBSC did not exceed Pt/C (**Figure 11b**). Moreover, the NBSC preferred 4e process responsible for complete oxygen reduction (the number of electron transfer, n = 3.81 to 3.92) (**Figure 11c**). In addition to ORR, NBSC was superior to BSCF and even IrO_2 (the well-known highly active OER catalyst) in terms of OER overpotential (η_{OER}) (**Figure 13a**) and its durability (**Figure 13b**): η_{OER} at 10 mA cm^{-2} of NBSC is 60 mV lower than 1.76 V for BSCF and IrO_2.

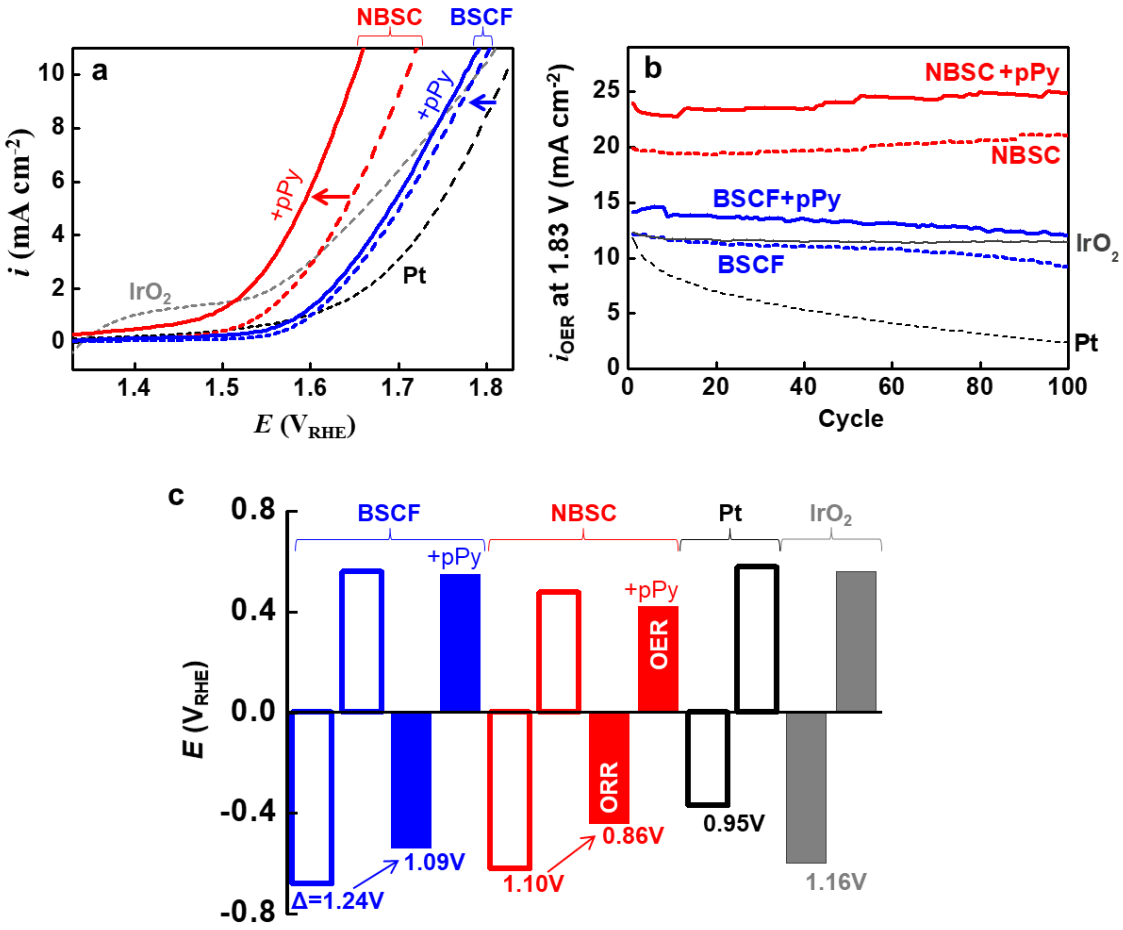

Figure 13. OER & Bifunctionality **(a)** OER polarization at anodic scan (10 mV sec^{-1}) on 1600 rpm. The contents of C and pPy/C were indicated in Figure 1. **(b)** OER Stability. The OER current (i_{OER}) at 1.83 V was traced along repeated cycles between 0.93 V and 1.83 V vs. RHE. (**c**) Bifunctionality represented by potential gaps (Δ) between the potentials at -3 mA cm^{-2} for ORR (E_{ORR}) and at +10 mA cm^{-2} for OER (E_{OER}). TheΔ are indicated as numerical values while bars indicate the overpotential of ORR and OER (η; E_{eq} = 1.23 V vs. RHE).

For more remarkable improvement, we added a nitrogen component (polypyrrole or pPy) to the perovskite oxide catalysts to boost up their kinetics because the nitrogen contents have been reported to improve ORR kinetics. Electronically coupled metal-nitrogen (M-N) active sites have been proposed as the key component of the previously reported N-assistant ORR.[84] The catalyst materials based on the M-N sites include: nitrogen-containing macrocyclic metal complexes (e.g., cobalt phthalocyanine, CoPc[85] and iron phthalocyanine, FePc with an additional pyridine ligand in the axis vertical to the Pc plane[86]); metal ions coordinated to a nitrogen-containing polymer (pPy)[87]; M-N-C composites prepared by pyrolyzing a mixture of precursors of metal, nitrogen and carbon[88-92]. Even without metal components, nitrogen-doped graphenes showed good catalytic ORR activities.[93] Also, the M-N active sites were developed by incorporating metal oxides to the N-doped carbons (MO-N-C composites).[21, 94-96] It should be pointed out that the high ORR electroactivities have not been previously achieved by physically mixing metal-containing catalysts and N-containing materials. Strong electronic interactions between metal and nitrogen atoms are required for generating the electroactive M-N sites. Therefore, guaranteed for making M-N-C or MO-N-C composites should be (1) the M-to-N physical contacts by mixing M and N precursors homogeneously in a molecular level (e.g., by dissolving precursor molecules together in a solvent or by adsorbing metal ions on nitrogen-doped carbon substrates) and (2) the strong interaction between M and N atoms (e.g., developed by pyrolysis).

In the presence of pPy, interestingly, the catalytic ORR and OER kinetics of the perovskite oxides were remarkably improved by simply *mixing* (not pyrolyzing) the catalysts with pPy. Carbon black (C; Ketjenblack) was replaced by pPy/carbon black composite (pPy/C; **Figure 14b**). The pPy reduced ORR overpotentials by shifting E_{onset} to the more positive values: to 0.835 V by +135 mV for NBSC; to 0.77 V by +110 mV for BSCF (**Figure 13a**). It should be noted that the E_{onset} of pPy/C (0.7 V) is less positive than those of the composites of perovskites and pPy/C. Also, the current parameters (j_o and j_k) of both perovskites increased dramatically in the presence of pPy (**Figure 13b**). In addition, more complete ORR was achieved by BSCF in the presence of pPy: n increased from 3.5 without pPy to 3.7 (**Figure 13c**). It was difficult to observe a significant increase in n of NBSC because the complete reduction around n = 4 was already reached even without pPy. The electroactivity of pPy-assistant NBSC, considered as the catalyst comparable to platinum in terms of ORR electroactivity, was tested in Zn-air cells (**Figure 13d**). The pPy-assistant NBSC showed smaller ORR overpotential than NBSC (however, larger than Pt) and the longest operation even longer than Pt during discharge.

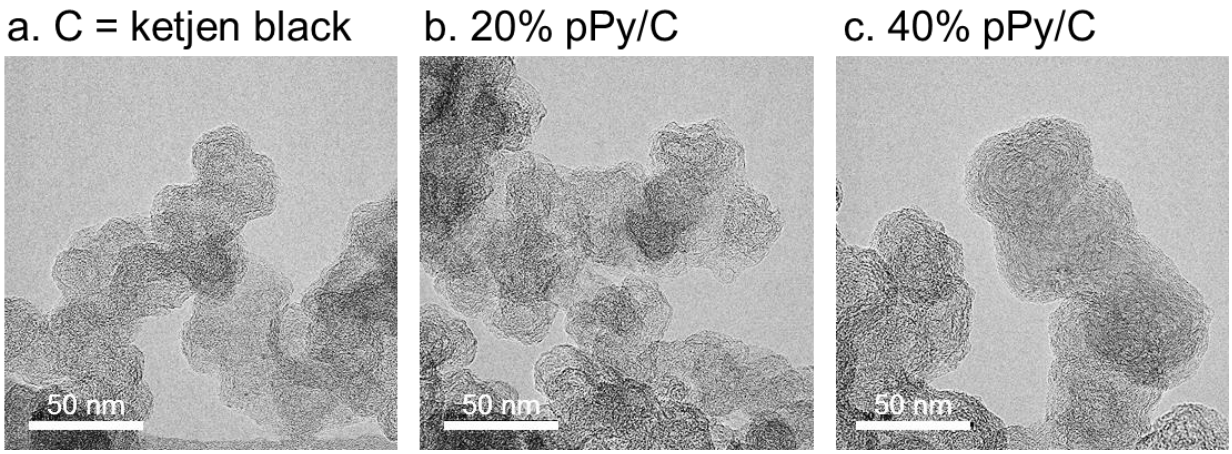

Figure 14. TEM images of carbon black and pPy/C. **(a)** C = Ketjen black. **(b)** 20 % pPy/C. **(c)** 40 % pPy/C. The scale bars are for 50 nm.

The similar improvement was observed in OER. The pPy decreased the η_{OER} of NBSC from 1.70 V to 1.65 V while η_{OER} of BSCF was not significantly changed by pPy (**Figure 13a**). The cycle retention of OER should be emphasized because there is every possibility that the corrosion (especially of carbon) at such a highly positive potential range deteriorates the cyclability. The NBSC delivered OER current without a significant decay along cycles while BSCF showed 30 % current decay after 100 cycles (**Figure 13b**). The stabilities of both NBSC+pPy and BSCF+pPy followed those of the corresponding pPy-absent systems. Bifunctionality of NBSC+pPy, which is estimated by a gap (Δ) between the potentials at -3 mA cm^{-2} for ORR and +10 mA cm^{-2} for OER, was superior to other catalysts (**Figure 13c**): Δ = 0.86 V for NBSC+pPy versus 1.24 V for BSCF, 1.16 V for IrO_2 and 1.04 V for MnO_2[52]. The value of $\Delta$of the pPy-assisted NBSC is the smallest potential gap between ORR and OER, to the best of our knowledge, especially among perovskite-based bifunctional catalysts that have been reported (**Table 1**). Also, this is another example of OER improved by nitrogen contents that has been rarely reported.[21, 96, 97]

The amount of carbon (C) in the absence of pPy did not affect the electrocatalytic performances of NBSC (**Figure 15**). On the contrary, the overpotentials of the ORR and OER polarizations were significantly reduced with the increasing amount of pPy/C. The pPy/C effect suggests the possibility of catalytic or at least catalytically assistant roles of pPy. Even the use of only 5 wt. % pPy/C (1 wt. % pPy in overall composite electrodes) was effective in decreasing overpotential of ORR while 20 wt. % pPy/C (4 wt. % pPy in overall) showed more dramatic current increase before reaching a limiting current.

Table 3. The bifunctionality of perovskite oxide catalysts.

Catalysts	E_{ORR}(V_{RHE}) at -3 mA/cm^2	E_{OER}(V_{RHE}) at +10 mA/cm^2	ΔE (V)	Ref
$NdBa_{0.2}Sr_{0.8}Co_2O_{3-\delta}$ with pPy[1a,2a]	0.79	1.65	0.86	This work
$NdBa_{0.2}Sr_{0.8}Co_2O_{3-\delta}$[1a,2a]	0.61	0.71	1.10	This work
$Ba_{0.5}Sr_{0.5}Co_{0.8}Fe_{0.2}O_{3-\delta}$[1a,2a]	0.55	1.79	1.24	This work
$Nd_{0.5}Sr_{0.5}CoO_{3-\delta}$/GnP nanorods [1a,2a]	0.70	1.72	1.02	98
$LaNiO_3$/NC[1a,2a]	0.65	1.61	0.96	97
$La_{0.5}Sr_{0.5}CoO_{2.91}$ Nanowires[1b,2a]	0.77	1.83	1.06	47
$La_{0.9}Sr_{0.1}CoO_3$ Yolk–shell[1a,2a]	0.69	1.79	1.10	99
$La_{0.5}Sr_{0.5}Co_{0.8}Fe_{0.2}O_3$/NCNT[1a,2b]	0.53	1.70	1.17	100
$La_{0.8}Sr_{0.2}Mn_{0.6}Ni_{0.4}O_3$[1a,2a]	0.47	1.78	1.31	101
$La_{0.7}(Ba_{0.5}Sr_{0.5})_{0.3}Co_{0.8}Fe_{0.2}O_{3-\delta}$[1a,2a]	0.62	1.62	1.00	102
$LaNiO_{3-\delta}$[1b,2a]	0.59	1.65	1.04	52
Pt/$CaMnO_3$[1b,2a]	0.85	1.83	0.98	103
$La_{0.95}FeO_{3-\delta}$[1b,2a]	0.47	1.66	1.28	92

[1]Scan rate: 1a = 10 mV sec^{-1}; 1b = 5 mV sec^{-1} [2]Rotation speed: 2a = 1600 rpm; 2b = 900 rpm.

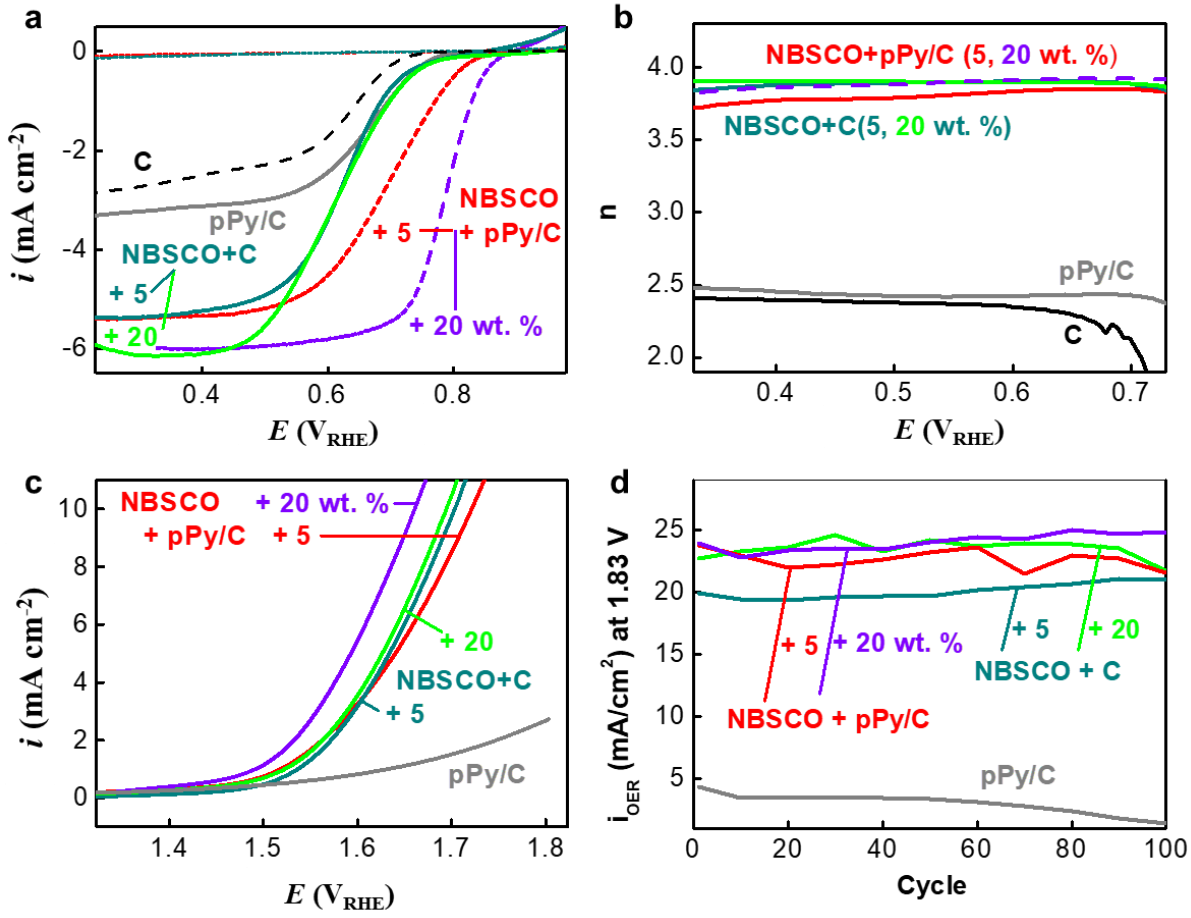

Figure 15. ORR and OER of NBSC in the presence of different conducting agents: carbon (Ketjen black; C) and polypyrrole/carbon black composite (pPy/C). **(a)** Voltammogram of disk currents of ORR in 0.1 M KOH (aq) at cathodic scan (scan rate = 10 mV sec^{-1}; rotation speed = 1600 rpm). **(b)** Number of electron transfer (n). **(c)** Voltammogram of disk current of OER at anodic scan (scan rate = 10 mV sec^{-1}; rotation speed = 1600 rpm). **(d)** Stability of OER. The OER current (i_{OER}) at 1.83 V vs. RHE was traced along repeated cycles consisting of anodic and cathodic scans between 0.93 V and 1.83 V vs. RHE.

The enhanced electroactivities of ORR and OER by pPy are surprising, considering that pPy is just physically contacted to the perovskite catalysts. The interaction between the pyrrolic N of pPy and the B-site Co of NBSC would not be as strong as the coordination bonds in the electroactive M-N sites.[88-91] There were no interactions between pPy and the perovskite oxides detected by X-ray photoelectron spectra (**Figure 16**). The possibility of conductivity enhancement by the conducting polymer pPy is not feasible since the conductivity of pPy[104, 105] is much lower than those of carbon black and NBSC.

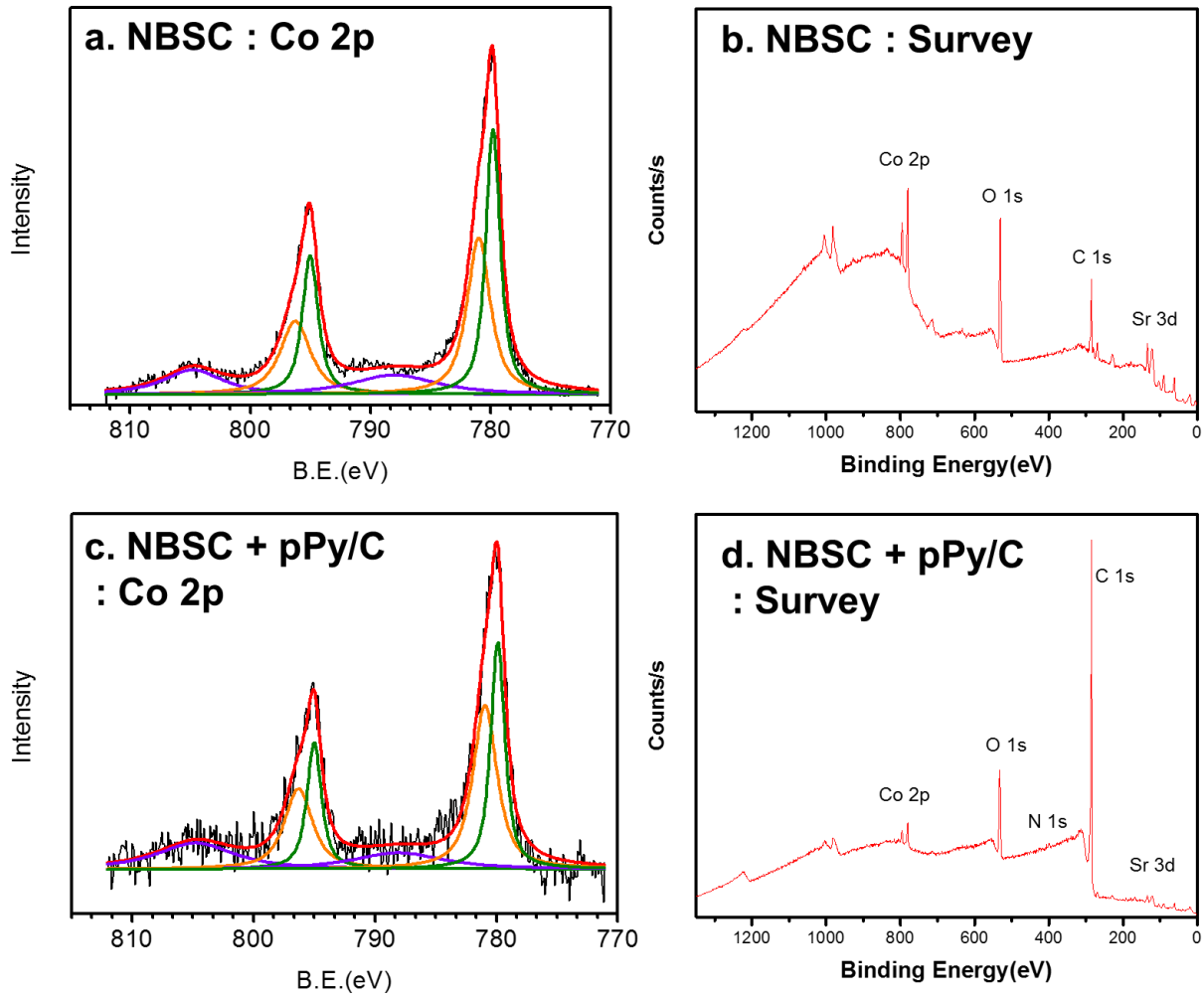

Figure 16. X-ray photoelectron spectra of Co2pwith the survey spectra. (a, b) NBSC. (c, d) NBSC + pPy/C. There were no differences observed between the two samples.

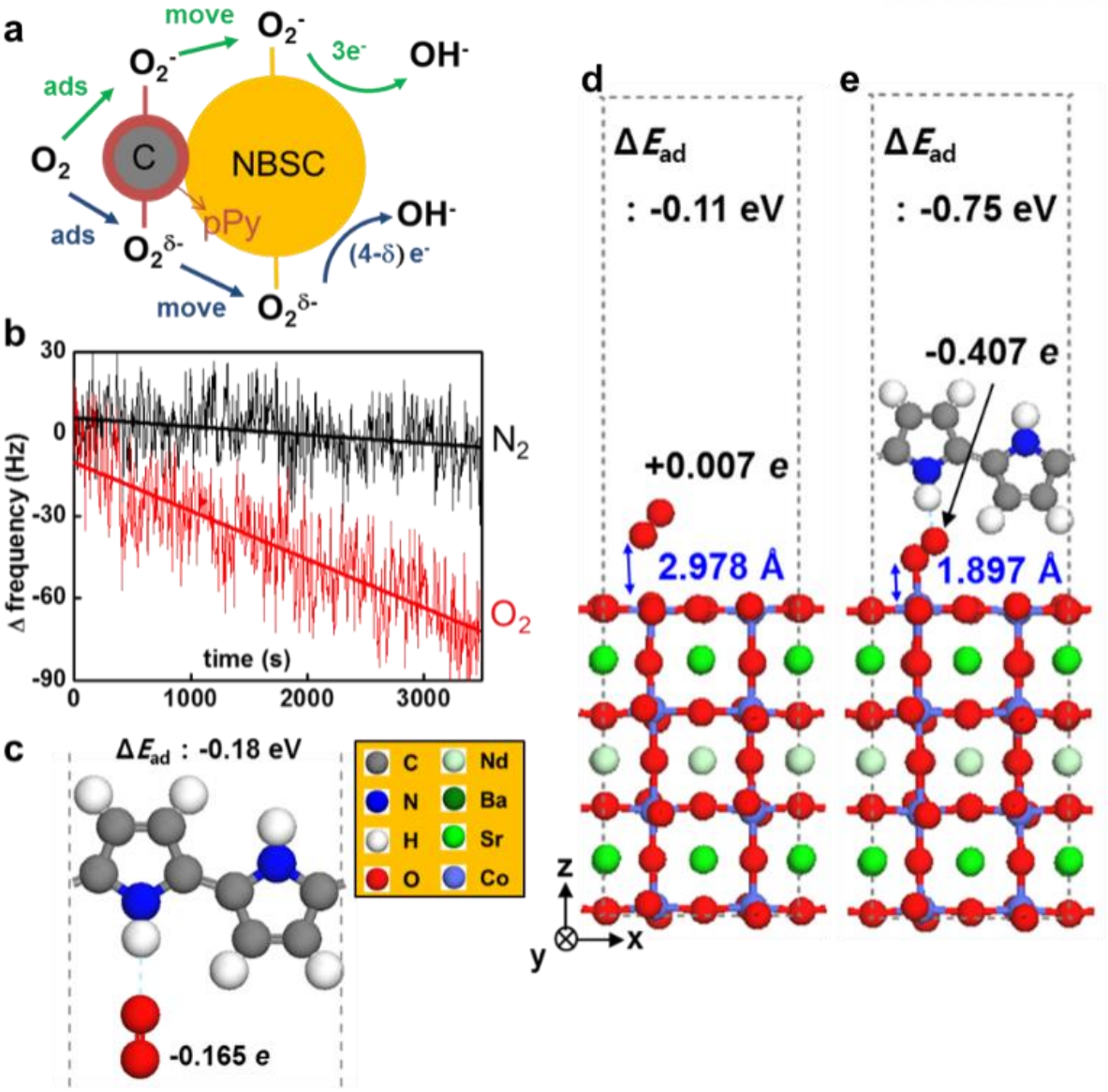

Figure 17. Sequential role allocation between pPy and oxide during ORR. (**a**) Proposed mechanism to explain the role of pPy on improved kinetics of ORR. (**b**) Frequency changes of a pPy-deposited quartz resonator in nitrogen-purged (black) or oxygen-saturated (red) deionized water. The optimized geometries of (**c**) O_2+ pPy, (**d**) NBSC+O_2 and (**e**) NBSC+O_2+pPy. The adsorption energy (ΔE_{ad}) of O_2 is indicated on top of each figure. Total charge of O_2 molecule and optimized distance between Co ion and O_2 are colored black and blue, respectively. Dashed cyan line indicates hydrogen bond. The gray dashed line indicates both lattice and periodic boundary.

Sequential allocation of catalytic roles between pPy and oxide catalysts for ORR is presumed after excluding the possibility of new active sites formation from the physical mixture of the catalysts and pPy/C.[106, 107] Introduction of pPy changed Tafel slopes of the perovskites from the two different values higher than 80 mV dec^{-1} to the same value at 65 mV dec^{-1} (**Figure 18a**). The same Tafel slopes possibly indicate that the rate-determining step (RDS) is identical.[59-62] Oxygen adsorption at the initial step is known to be the RDS of ORR on oxide catalysts.[41] Therefore, oxygen is thought to be adsorbed more dominantly on pPy in a more facile manner than on the perovskite oxide catalysts during ORR. No change in Tafel slopes of OER (the reverse reaction of ORR) also supports that pPy is relevant to the initial adsorption step because the RDS of OER is the second and/or the third steps of ORR (**Figure 18b**).[40] And, the values of n did not decrease significantly after the addition of pPy even though n obtained from pPy/C alone (2e) is much lower than that of perovskites (4e). Therefore, perovskite catalysts would be responsible for at least the latter half part of ORR (peroxide to oxide), driving 2e peroxide generation forward to complete 4e ORR.

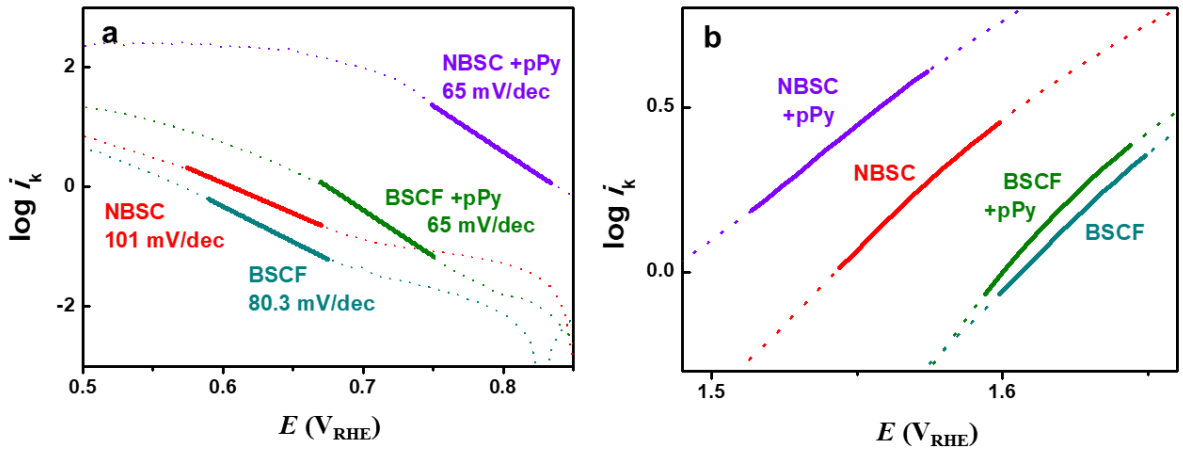

Figure 18. Tafel plots. **(a)** ORR. **(b)** OER.

Incorporation of molecular oxygen as a form of charge-transfer complex ($Py^{+}\cdot O_2^{-}$) and/or molecular association complex ($Py^{\delta+}\cdot O_2^{\delta-}$) into pPy is a possible route for the facile adsorption.[108-110] Mass gain of pPy-deposited quartz crystal resonators, indicated by frequency decrease, was observed along time only in oxygen-saturated media, confirming oxygen adsorption on pPy (**Figure 17b**). During the quartz crystal microbalance (QCM) experiment, the open circuit potential (OCV) changed from 0.1 $V_{Ag/AgCl}$ to 0.15 $V_{Ag/AgCl}$ in the presence of oxygen while no OCV change was observed in the absence of oxygen. It suggests that the electronic state of pPy changes by the interaction with oxygen and one

of the possible change is doping by oxygen species. Also, the oxygen adsorption was spectroscopically investigated. The O=O bond in molecular di-oxygen is not infrared (IR)-active due to its symmetry. However, oxygen adsorbed on pPy is IR- detected due to the interaction between -NH of pPy and oxygen to form NH^+-$^-$OO via hydrogen bond (**Figure 17c**). Intensity of the peak at 3737 cm^{-1}assigned to the OH stretching of NH^+-$^-$OO increased with exposure time to air **(Figure 19)**. Interestingly, strong interaction between -NH of pPy and oxygen was expected by density function theory calculation (DFT). -0.165 electron was transferred from pPy to oxygen at 2.24 Å gap due to the strong dipole of N-H bond. The gap between pPy and oxygen was smaller than those for conventional dopant molecules: 2.57Å for Cl^- and 3.5Å for benzene sulfonic acid.[111]

In our proposed mechanism (**Figure 17a and 20**), molecular oxygen is adsorbed on pPy and then electrons are transferred fully and/or partially from the pPy to the adsorbed oxygen ($Py^+ \cdot O_2^-$ in step 1). Even if $Py^{\delta+} \cdot O_2^{\delta-}$ is not shown in the mechanism, the molecular association complex is highly possible to co-exist with the charge transfer complex. Both complexes are possibly interpreted as dopants for pPy. The superoxide (O_2^-) and/or partially charged oxygen ($O_2^{\delta-}$) is transferred to the active site (M) of metal oxide to form O_2^--M or $O_2^{\delta-}$-M (step 2). The rest of steps follows the mechanism of ORR on perovskite oxide catalysts (step 3 to 5). The comparison of adsorption energy (ΔE_{ad}) by DFT calculation supported that the transfer of oxygen species from pPy to perovskite oxide catalysts is thermodynamically favored (**Figure 21 and Figure 17d-e**). Oxygen was preferentially adsorbed on pPy (ΔE_{ad} = -0.165 eV) rather than NBSC (-0.11 eV). Then, oxygen transfer from pPy to oxide catalyst was driven by the more negative ΔE_{ad} of oxygen on NBSC (-0.75 eV).In the presence of pPy, moreover, the distance between Co ion and O_2 decreased from 3.0 Å to 1.9 Å that is the bond length of chemisorption. This pPy-assisted O_2 adsorption was also contributed to significant charge transfer (i.e., -0.407 *e*) from pPy to O_2.

The assistant function of pPy for the ORR electroactivity was not observed from another nitrogen-containing conducting polymer, polyaniline **(Figure 22)**. As another possible scenario, pPy catalyzes peroxide formation via 2e transfer and then the perovskite oxide catalysts reduce the peroxide generated by pPy forward to oxide. However, peroxide reduction on the perovskite oxides was not faster in kinetics than oxygen reduction (**Figure 23**). There was no significant onset potential shift observed with the oxide catalysts (only with carbon black without pPy) in the presence of peroxide in electrolyte. Therefore, the first scenario of doping-and-transfer mechanism is more feasible than the second peroxide toss mechanism.

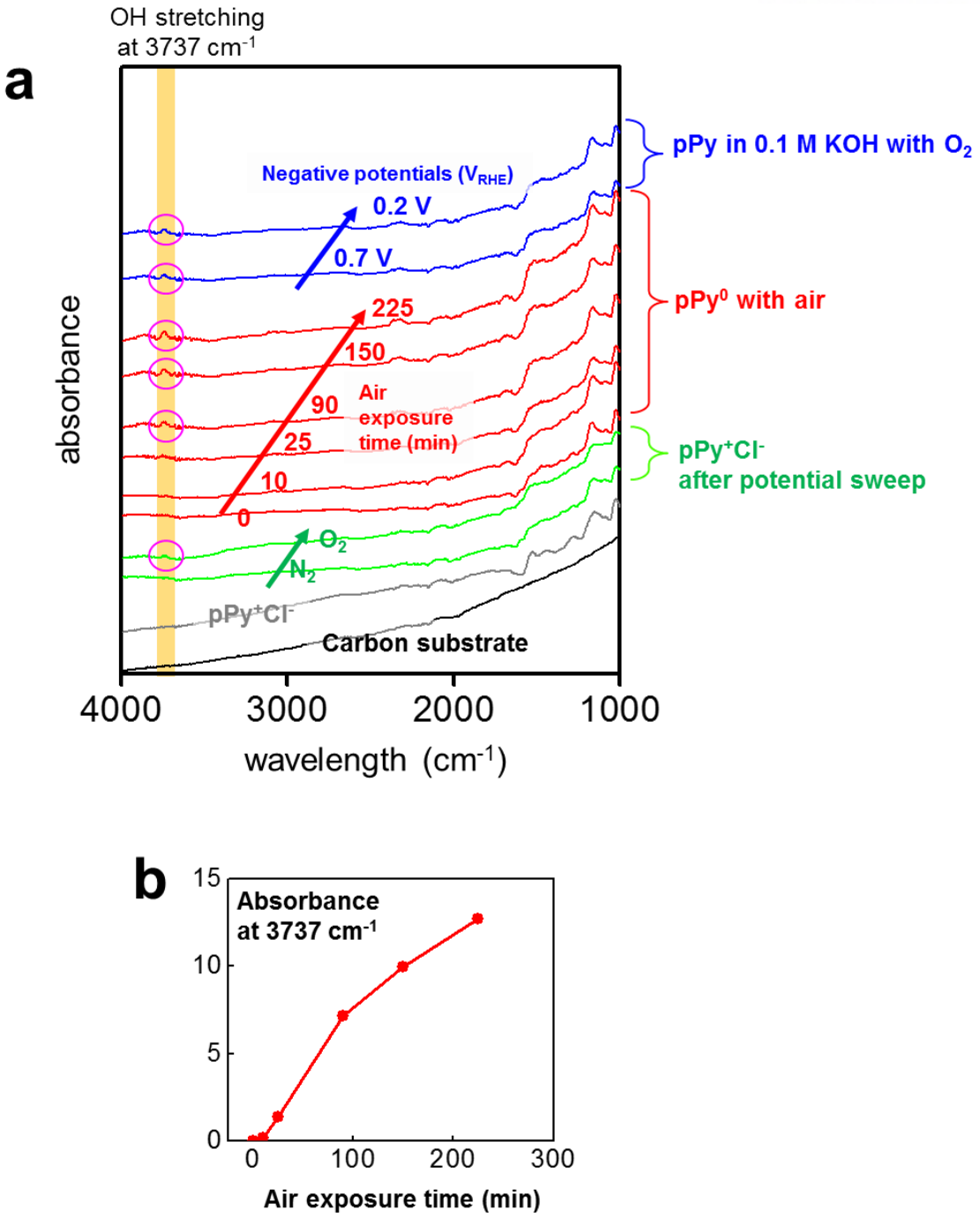

Figure 19. Spectroscopic characterization of pPy in the presence of O_2. **(a)** Infrared spectra. The peak at 3737cm^{-1} for OH stretching was developed along time when the pPy films were exposed to oxygen or air. **(b)** Temporal change in the absorbance at 3737cm^{-1}.

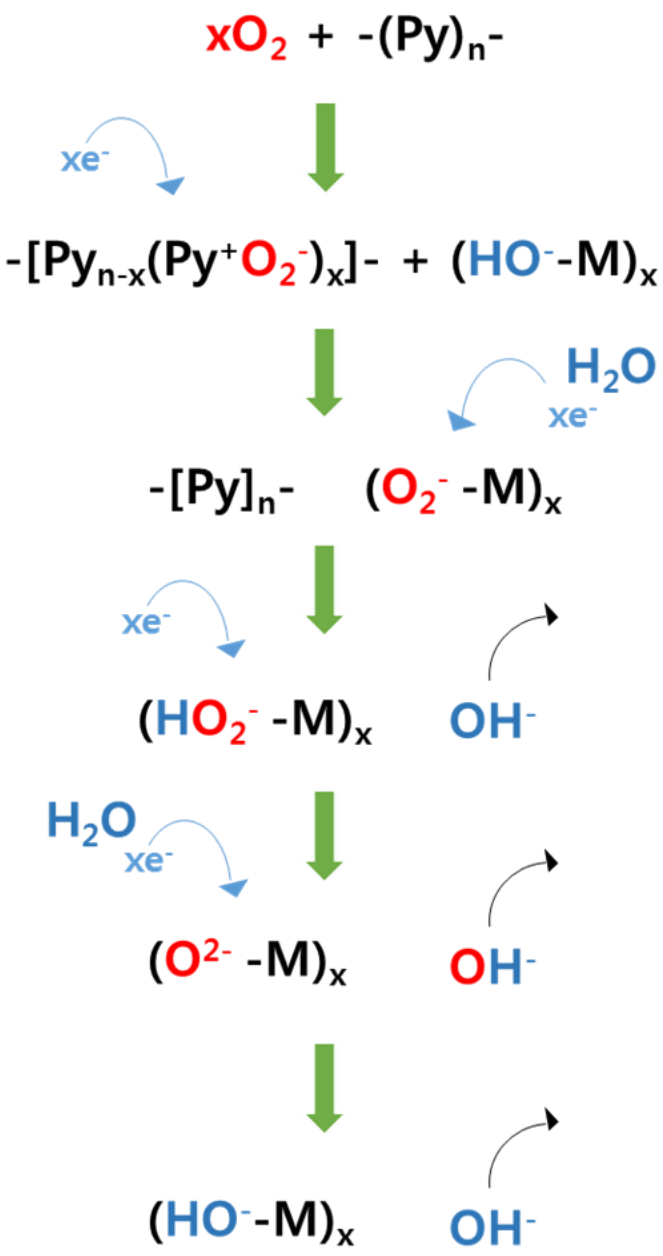

Figure 20. Proposed mechanism to explain the role of pPy on improved kinetics of ORR.

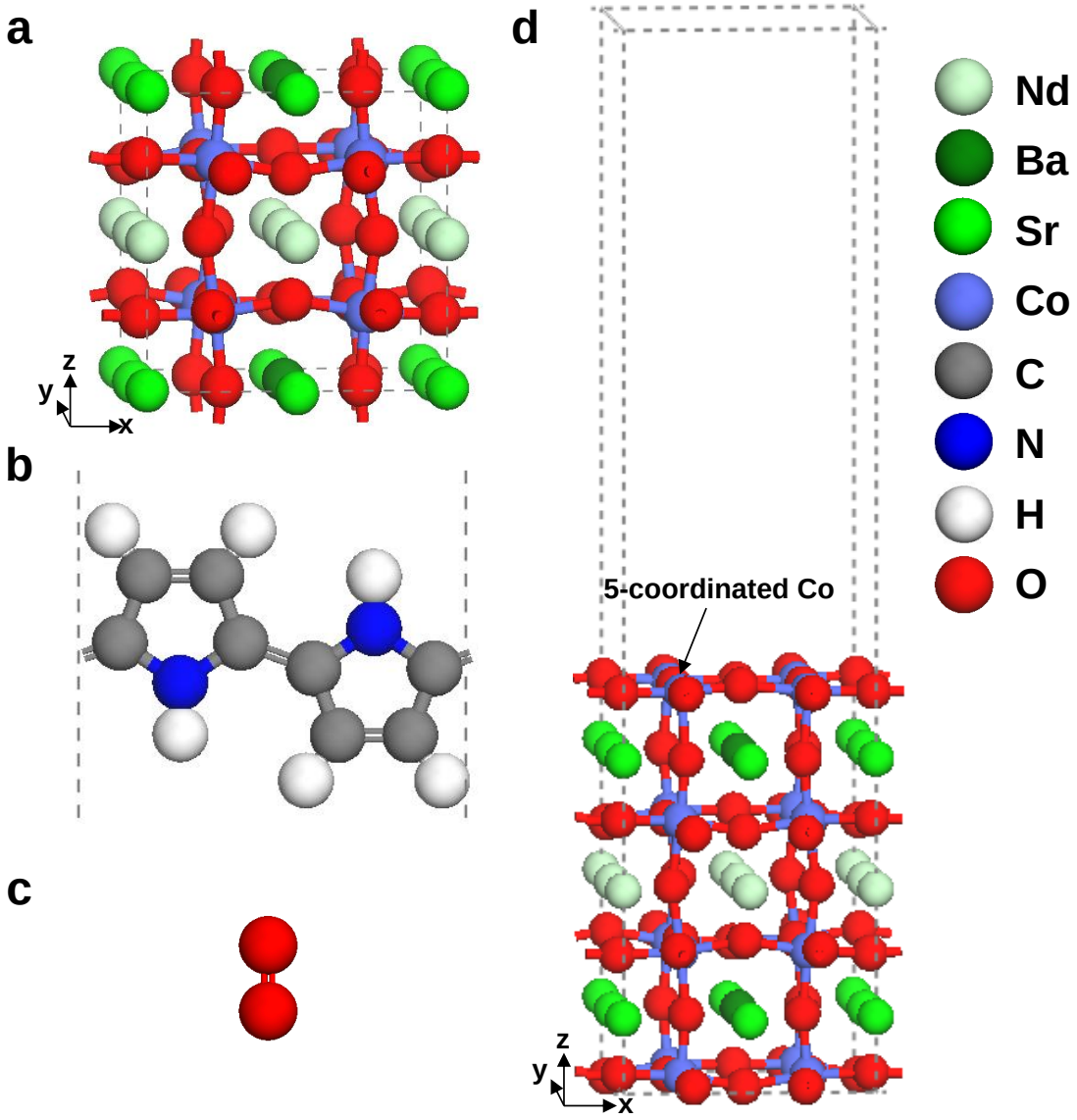

Figure 21. Optimized structures for DFT calculation. **(a)** NBSC. **(b)** pPy. **(c)** O_2. **(d)** (001) surface of NBSC. The labels of atomic colors are presented in the figure. The gray dashed line indicates both lattice and periodic boundary.

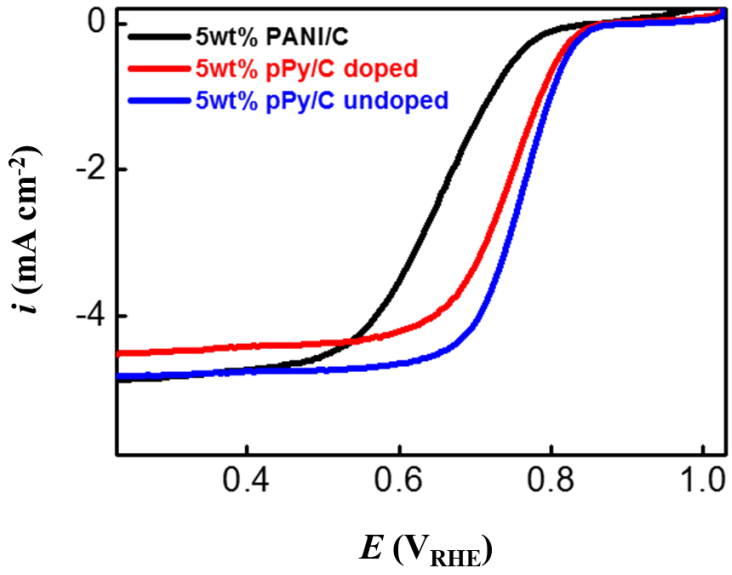

Figure 22. ORR polarization of NBSC in the presence of nitrogen-containing conducting polymers. Electrocatalytic layers were prepared by introducing 5 wt. % conducting polymer/carbon composites into NBSC. Doped pPy, undoped pPy or polyaniline was used as the conducting polymer. Scan rate = 10 mV sec^{-1}. Rotation speed = 1600 rpm.

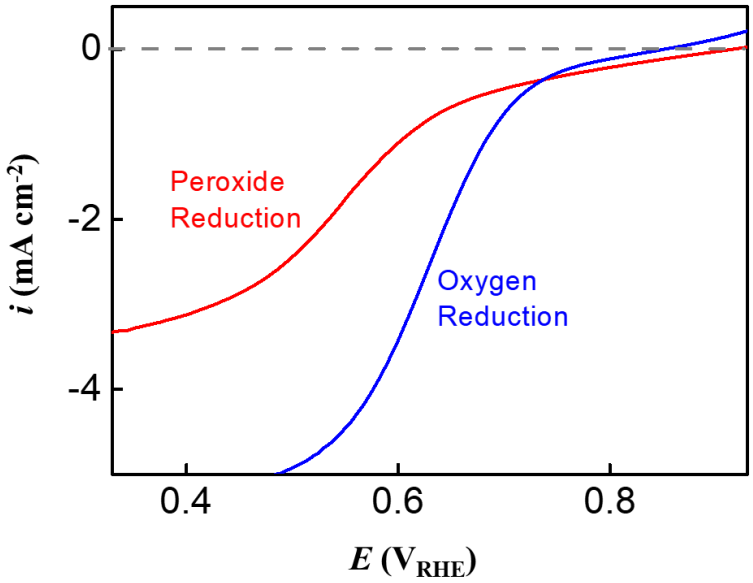

Figure 23. Polarization of peroxide reduction on NBSC in the presence of 2mM peroxide in 0.1M KOH (aq) (red solid line). Presented for comparison was the ORR polarization on NBSC in oxygen-saturated 0.1M KOH (aq) (blue solid line). Scan rate = 10 mV sec^{-1}. Rotation speed = 1600 rpm.

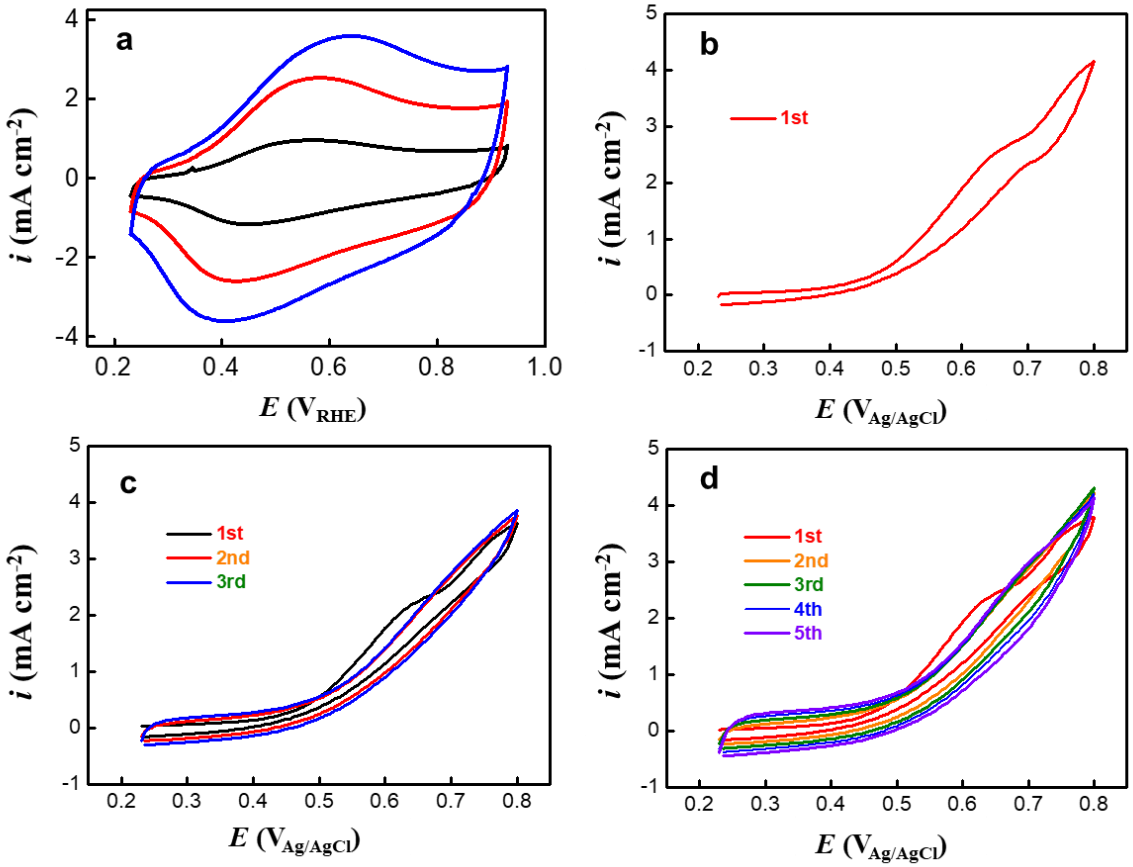

Figure 24. Electrodeposition of pPy on NBSC+C. **(a)** Cyclic voltammogram (CV) of the ORR on disk electrode in N_2-saturated 0.1 M KOH (aq) at 10 mV sec^{-1}. Black, red and blue line are pPy03, pPy06 and pPy09.

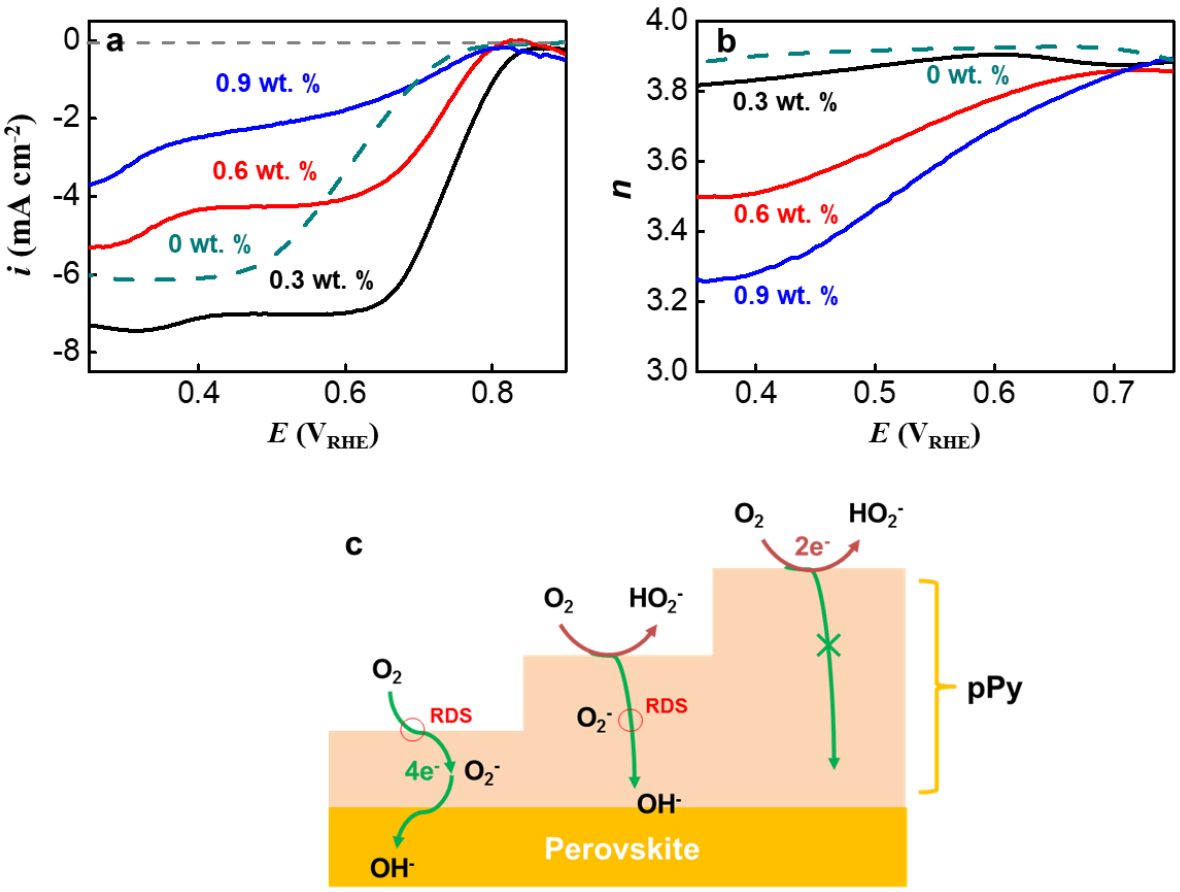

Figure 25. ORR on pPy-deposited perovskite oxide. 0, 0.3, 0.6 and 0.9 wt. % of pPy was electrochemically deposited on NBSC. **(a)** ORR polarization in 0.1 M KOH (aq) at cathodic scan at 10 mV sec^{-1} at 1600 rpm. The pPy amounts were indicated. **(b)** The number of electron transfer (n). **(c)** Oxygen reduction on perovskite catalysts covered with pPy of three different thicknesses.

The same pPy-assistant ORR improvement was observed when pPy is electrodeposited on NBSC catalytic layers. Three different amount of pPy was deposited at 0.3, 0.6 and 0.9 wt. % (**Figure 24**). The limiting currents and the n values decreased with deposited pPy amount (**Figure 25a** and **b; Figure 26**). It appears to be contradictory with the improvement of the onset potentials and the n values encouraged by the increasing amount of pPy/C (**Figure 25**). However, these electrodeposited pPy cases are different from the composite cases obtained by mixing catalyst particles and pPy/C particles (**Figure 27**). In the pPy/C cases, its amount is directly related to the effective area of pPy. On the contrary, the more amount of electrodeposited pPy increases the thickness of pPy films instead of area. In thicker pPy layers, O_2^- in the charge transfer complex and/or $O_2^{\delta-}$ in the molecular association complex is hard to be transferred to the active sites of perovskite oxide catalysts (**Figure 25c**). It is likely that rate determining step is moved from oxygen adsorption to diffusion of O_2^-/ $O_2^{\delta-}$. Therefore, a significant

amount of the intermediate oxygen species does not go forward to OH^- but to peroxide so that the n value decreases (**Figure 25b**). On the other hand, the onset potential was not changed significantly with the pPy film amounts (**Figure 25a**). It is another evidence to confirm the feasibility of our scenario on the catalytic role allocation model.

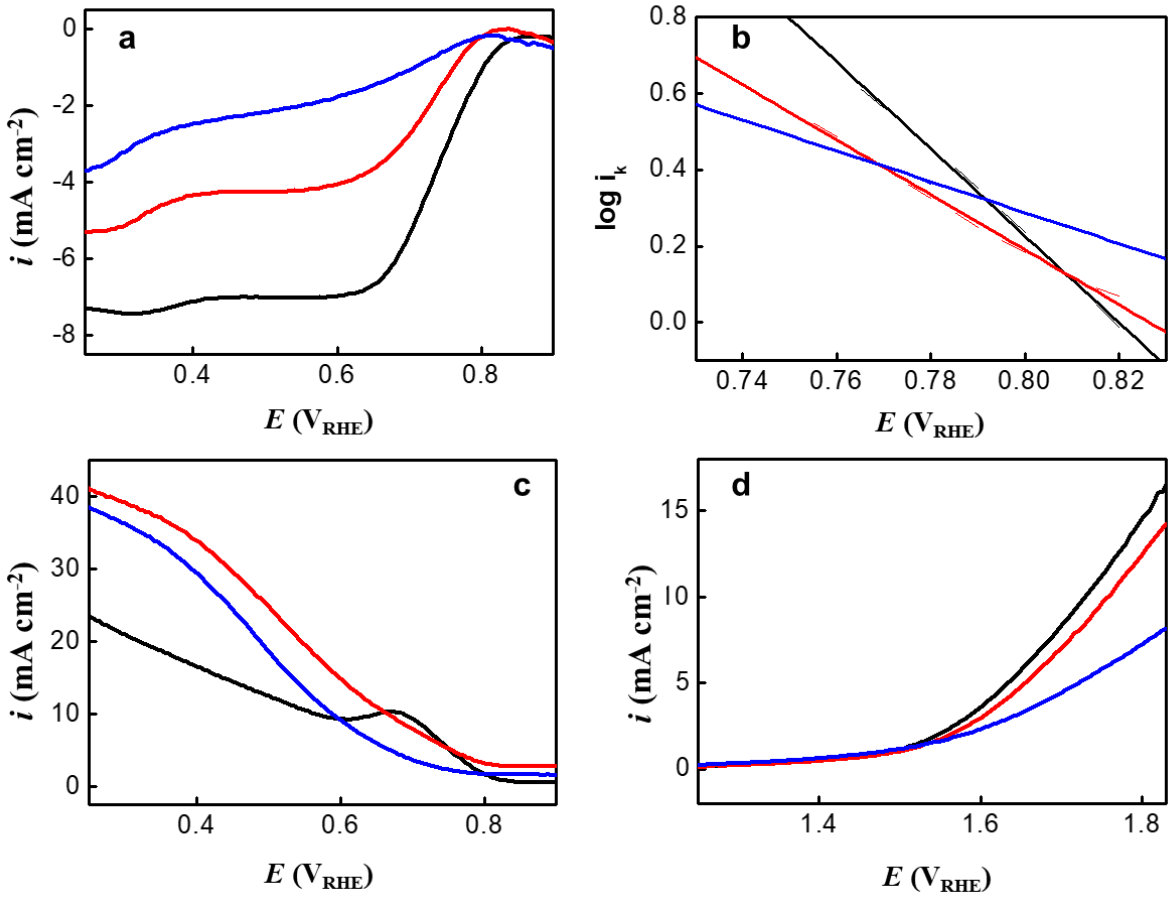

Figure 26. ORR and OER of pPy/NBSC. Black, red and blue lines are 0.3, 0.6 and 0.9 wt. % of pPy on NBSC catalyst layer, respectively. **(a)** ORR polarization in 0.1 M KOH (aq) at cathodic scan (scan rate = 10 mV sec^{-1}; rotation speed = 1600 rpm). **(b)** Tafel plots. **(c)** Voltammogram of ring current of re-oxidization at 0.4V. **(d)** OER polarization at anodic scan (scan rate = 10 mV sec^{-1}; rotation speed = 1600 rpm).

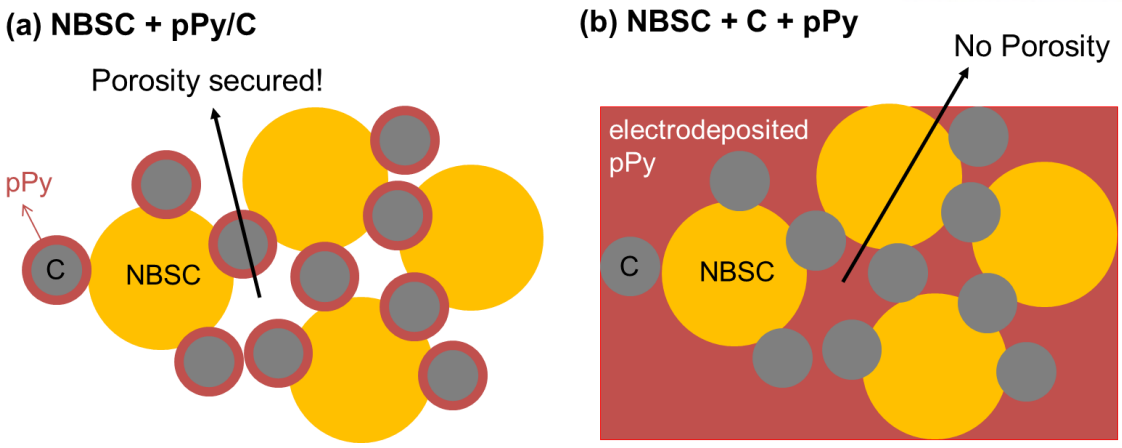

Figure 27. NBSC + pPy/C versus NBSC + C + pPy. It should be notified that the pPy-deposited system (**Figure 13**) includes carbon (C) because pPy was electrodeposited on a mixture of NBSC and C (NBSC+pPy+C). The ORR kinetics was faster in NBSC+pPy/C (**Figure 10a**) than in NBSC+pPy+C (**Figure 13a**) when comparing the slopes of current increase before the limiting situation between the two systems. Electric conductivity would not be significantly different between NBSC+pPy/C and NBSC+C+pPy. However, the major difference comes from mass transfer. The use of pPy/C guarantee the porosity between the particles of NBSC and pPy/C. On the contrary, pPy films could block the ionic pathways existing between NBSC and C in the NBSC+C+pPy system.

3.4. Experimental

Material Preparation.

Two different double perovskites (NBSC and NBSC*) were prepared. NBSC was synthesized by sol-gel method. Stoichiometric amounts of $Nd(NO_3)_3 \cdot 6H_2O$, $Ba(NO_3)_2$, $Sr(NO_3)_2$ and $Co(NO_3)_2 \cdot 6H_2O$ were dissolved in distilled water with proper amount of Pluronic F-127. All chemical was used as received from Aldrich. The solution was dried in the oven at 100 ºC for one day. The precursor gel was heated up to 300 ºC in air. Fine powders obtained during the combustion were calcined at 600 ºC for 4 h and then sintered in air at 950 ºC for 4 h. For measuring intrinsic electrical conductivity, the powder was pressed into pellets at 5 MPa and sintered in air at 1100 ºC for 12 h instead of the thermal treatment at 950 ºC for 4 h to achieve a relative density higher than 95 %. Smaller-size NBSC* was prepared by electrospray process. The same precursors used for NBSC were dissolved at 0.01 M each in N,N-dimethylformamide (DMF), followed by introducing 15 wt. % PVP (polyvinylpyrrolidone, Mw = 1,300,000) into the solution. The precursor solution was placed in a 30 ml syringe with a positively charged capillary tip with a diameter of 0.5 mm. 10 kV voltage was applied between the syringe needle tip as an anode and a metal collector wrapped with aluminum foil as a cathode with a gap at 11 cm by a high-voltage power supply (Korea Switching). The composite droplets were electrosprayed from the needle at 0.3 ml h^{-1} and collected on the aluminum foil. The electrosprayed powders were dried at 80 ºC for 1 h in air and then calcined at 3 ºC min^{-1} ramping to 800 ºC for 4 h in air.

Physicochemical characterization.

The crystallographic structures of materials were characterized at a scan rate of 0.6 degree min^{-1} with the 2θ range of 20 º to 60 º by X-ray diffraction (XRD; Rigaku diffractometer D/MAZX 2500V/PC with Cu Kα radiation). Scanning electron microscopy (SEM; FEI Nanonova 230) was used to snapshoot their morphologies. Electrical conductivities were measured in air by a four-point probe configuration. Ag wires as probes were connected to samples by Ag paste. The current/voltage was controlled/measured by a potentiostat (BioLogic VMP3) in a temperature range of 25 to 700 ºC.

Electrode preparation.

Catalyst inks were prepared by dispersing a catalyst and a conducting agent in 0.45 ml of ethanol, 0.45 ml of isopropyl alcohol and 0.1 ml of 5 wt. % nafion solution (Sigma-Aldrich 274704). The total amount of the catalyst and the conducting agent was fixed at 20 mg. A series of NBSCs were used as the double perovskite catalysts: NBSC and NBSC*. BSCFO was used as the simple perovskite counterpart. Carbon black (C; Akzo Nobel Ketjenblack 600JD) or its composite with polypyrrole (pPy/C; Sigma-Aldrich 530573) was used as the conducting agent at 0, 5 and 20 wt. %. 5 ul of the catalyst ink was dropped on

the disk compartment of ring-disk electrodes. Loading density of the composite of catalyst and conducting agent was fixed at 0.8 mg cm^{-2}. For comparison, 20 wt. % platinum nanoparticles supported by carbon black (Pt/C; Premetek P10A200) was used as a control.

Electrochemical characterization.

Cyclic and linear sweep voltammograms (CVs and LSVs) were obtained on disk and ring electrodes simultaneously by a bipotentiostat (iviumstat, Ivium Technologies). Ring-disk electrodes (RRDE) of glassy carbon disk and platinum ring was used as the working electrode (disk area = 0.1256 cm^2) while a platinum wire and a Hg/HgO electrode were used as the counter and reference electrodes respectively. The RRDEs were rotated at various controlled speeds (1600 rpm unless otherwise indicated) by a RRDE controller (ALS RRDE-3A). An aqueous solution of 0.1M KOH was used as the electrolyte. ORR polarization curves were obtained on the disk electrode from a cathodic sweep from +0.1 V to -0.7 V (vs. Hg/HgO) at 10 mV s^{-1} after five cycles of CVs. The electrolyte was saturated by oxygen for ORR while it was purged by nitrogen to measure background currents. +0.4 V was applied to the ring electrode to estimate the amount of peroxide generated from the disk electrode. The anodic sweeps from +0.35V to +0.9V (vs. Hg/HgO) after nine cycles were presented as OER polarization curves. The other conditions were the same as those for the ORR polarization curves. To demonstrate the stability of OER, anodic and cathodic sweeps were repeated at 50 mV s^{-1} for 100 cycles. The values of potential were converted from versus Hg/HgO to versus the reversible hydrogen electrode (RHE) by: Hg/HgO + 0.929 V = RHE. For the correction, the potential difference between Hg/HgO and RHE was measured in a cell where platinum wires were used as the working and counter electrodes in a hydrogen-saturated aqueous electrolyte of 0.1 M KOH with Hg/HgO as the reference electrodes. The open circuit potential was read at -0.929 V vs. Hg/HgO from a LSV at 1 mV s^{-1}.

pPy electrodeposition.

20mM pyrrole was dissolved in 0.1M $LiClO_4$ (aq). Three electrodes were immersed in the electrolyte: NBSC-loaded disk electrode (area = 0.1256 cm^2) of a rotating ring-disk electrode (RRDE) as a working electrode, a platinum wire as a counter and a Ag/AgCl electrode as a reference. The same catalyst ink as described above was used for loading NBSC for the working electrode. Pyrrole was electro-polymerized on the working electrode in the N_2-saturated electrolyte. Potential was swept at 5 mV s^{-1} between +0.2 $V_{Ag/AgCl}$ to +0.8$V_{Ag/AgCl}$ one, three and five times by a potentiostat (Ivium Iviumstat). The loading amounts of pPy on the NBSC working electrodes were calculated from the charges consumed for electrodeposition under the assumption that positive charges are developed in pPy every three monomeric unit.

pPy-O_2 interaction.

pPy films were electrodeposited on gold-coated quartz crystal resonators for quartz crystal microbalance (QCM; SEIKO QCM922) and on carbon screen-printed electrodes (Zensor, SE100; area = 0.196 cm^2) for infrared-spectroscopic (FTIR; Bruker Alpha) measurement. Pyrrole was electrochemically polymerized at 0.1 mA $cm^{-2}$for 150s in 0.1 M pyrrole in 0.1 M NaCl (aq). Then, the pPy films were de-doped at -0.5$V_{Ag/AgCl}$ for 20s. Frequencies of the pPy-deposited resonators were recorded as a measure of mass along time in nitrogen-purged or oxygen-saturated deionized water.

Zn-air batteries.

Coin-type zinc-air batteries (2032; diameter = 20 mm) were assembled with 6M KOH (aq) as an electrolyte, zinc plate as an anode, 0.05 g cm^{-2}catalyst-carbon composite loaded on carbon paper as a cathode. NBSC, NBSC+pPy/C or Pt/C was used as the catalyst for cathodes. Discharge curves were obtained at 20mAcm^{-2}.

DFT calculations.

Density functional theory (DFT) calculations were performed using Vienna Ab-initio Simulation Package (VASP)[112, 113]. The generalized gradient approximation with Perdew-Burke-Ernzerhof functional (GGA-PBE)[66] was employed for the exchange correlation energy. The electron-ion interaction was described by projector augmented-wave (PAW)[114] method. The cutoff energy for the plane wave basis set was set to be 400 eV. Spin polarization and Grimme's D2 dispersion correction[115] were considered in all calculations. The convergence criteria for self-consistent field (SCF) calculations was set to be 10^{-5} eV. The atomic positions and lattice parameters were relaxed until the Hellmann-Feynman forces acting on ions were less than 0.02 eV/Å. 3 × 3 × 3and 3 × 3 × 1 *k*-point meshes with Monkhorst-Pack scheme were used for bulk and surface systems, respectively. Bader charge analysis[116-118] was implemented to investigate the atomic charges.

Modeling and calculation details

The unit cell of $Nd_4BaSr_3Co_8O_{24}$ (NBSC) double perovskite was constructed by replacing one Sr atom by one Ba atom in $Nd_4Sr_4Co_8O_{24}$ (**Figure 21**). The lattice parameters of the optimized unit cell were determined as a = 7.53 Å, b = 7.61 Å, c = 7.51 Å, α = 90.73°β = 90.00°, and γ = 90.00°. Using the optimized unit cell, a symmetric slab model of (001) surface consisting of 7 atomic layers was constructed with the vacuum slab of 20 Å (**Figure S18**). Two atomic layers at the bottom were fixed during optimization to consider the bulk-like effect. To elucidate the role of the pPy for the adsorption of O_2 on NBSC surface, we constructed three model systems (i.e., O_2+pPy, NBSC+O_2 and NBSC+O_2+pPy) as shown in **Figure 17c-e**. The interaction between O_2 and pPy was investigated by

O_2+pPy system, which was constructed by placing O_2 near N-H bond of pPy. The pPy-assisted O_2 adsorption on the NBSC surface was investigated by comparing NBSC+O_2 and NBSC+O_2+pPy systems, where O_2 was placed above the 5-coordinated Co ion and the pPy was placed above O_2.

The adsorption energy (ΔE_{ad}) of O_2 for three systems was calculated as follows,

$$\Delta E_{\text{ad}} = E_{\text{O}_2+\text{pPy}} - E_{\text{pPy}} - E_{\text{O}_2} \quad (1)$$

$$\Delta E_{\text{ad}} = E_{\text{NBSC+O}_2} - E_{\text{NBSC}} - E_{\text{O}_2} \quad (2)$$

$$\Delta E_{\text{ad}} = (E_{\text{NBSC+O}_2\text{+pPy}} - E_{\text{NBSC}} - E_{\text{O}_2\text{+pPy}}) - (E_{\text{O}_2\text{+pPy}} - E_{\text{pPy}} - E_{\text{O}_2}) \quad (3)$$

where $E_{\text{O}_2\text{+pPy}}$, $E_{\text{NBSC+O}_2}$, and $E_{\text{NBSC+O}_2\text{+pPy}}$ represent the total energy of each system and E_{NBSC}, E_{O_2}, and E_{pPy} represent the energy of isolated NBSC surface, O_2, and pPy respectively. Note that the first and second term of equation (3) represent the interaction energy between NBSC and O_2+pPy and that between O_2 and pPy, respectively. Thus, we can calculate adsorption energy of O_2 on NBSC surface by subtracting those two terms.

3.5. Conclusions

In the presence of pPy, the ORR and OER activities of perovskite oxide catalysts were significantly improved in terms of kinetics and the number of electron transfer. The sequential role allocation between pPy and oxide catalysts for ORR was suggested to explain the synergistic effects of the organic and inorganic catalysts (pPy and perovskite). Oxygen is doped into pPy as a form of superoxide or partially charged oxygen species. The doped species are transferred from pPy to active sites of perovskite oxide catalysts. The oxygen species on perovskite are completely reduced.

IV. Secondary-amine-conjugated Polymer-assisted Oxygen Reduction Reaction on Cobalt-based Oxides.

4.1. Abstract

Synergistic effects of dual homogeneous catalysts for chemical reactions have been reported. Double activation (chemical transformation process where both catalysts work in concert to activate reactants or intermediates) was often responsible for the synergistic effects of the dual catalyst systems. Herein, we demonstrate the extension of the double activation from chemo-catalysis to electrocatalysis. The activity of low-cost cobalt oxide electrocatalysts for oxygen reduction reaction (ORR) was significantly improved by introducing a secondary-amine-conjugated polymer (HN-CPs) as the second electrocatalyst. The HN-CP activated neutral diatomic oxygen to the corresponding partially charged species ($O_2^{\delta-}$) in the initial oxygen adsorption step of the ORR. Also, the proton of the HN-CPs was transferred to the single oxygen intermediate (*O) on the active site of the electrocatalyst. The electron donation number of the HN-CPs to diatomic oxygen (δ in $O_2^{\delta-}$) well described the order of activity improvement, i.e., polypyrrole (**pPy**) > polyaniline (**pAni**) > polyindole (**pInd**). The maximum overpotential gain at ~150 mV was achieved by using **pPy** with the highest δ.

4.2. Introduction

The oxygen reduction reaction (ORR) is omnipresent. Oxygen is the final electron acceptor in the electron transfer chain in the mitochondria of living cells used to store energy in adenosine triphosphate.[119, 120] The same reaction is used to generate electricity in artificial energy storage devices, including fuel cells and metal-air batteries. The ORR is known for its slow kinetics, limiting the overall current extracted from ORR-based energy devices.[35] Pt is the best ORR catalyst to increase the limited power performance, but its use in practical devices is limited due to its high cost. A wide spectrum of cost-effective electrocatalyst alternatives to Pt have been proposed[71-75], including atomic composites of metal[121], metal-nitrogen-carbon composites (M-N-C)[84, 87], doped carbons[93] and transition metal oxides[122]. Pt-level ORR activities, which could not be achieved by nonprecious metal catalysts a decade ago, have been reported for M-N-C, doped carbon and nanostructured or nanocomposite metal oxides.[21, 94, 95] However, the striking ORR activities of these alternative materials were obtained at the cost of sophisticated material engineering, e.g., pyrolyzing a mixture of metal, nitrogen and carbon precursors (M-N-C); doping carbons with heteroatoms (e.g., N-doped graphene); and nanostructuring and/or nanocompositing metal oxides. It is still difficult to obtain Pt-level ORR activities without employing such sophisticated strategies.

Dual-catalyst system, called synergistic catalysis or dual catalysis, in which two catalysts work simultaneously to decrease the activation energy of the reaction overall has been well described in chemical synthesis.[8-10] Similar concept was computationally proposed in electrocatalysis for ORR and oxygen evolution reaction (OER) as one of way to circumvent these scaling relationships between adsorption energies of different reaction intermediates which fundamentally limit catalytic activities.[15] In this work, we demonstrate that the ORR activities of heterogeneous catalysts are significantly improved by simply mixing catalyst particles with secondary-amine-conjugated polymers (HN-CPs). No sophisticated material engineering of catalysts was involved in developing the intimate interaction between the active sites of catalysts and the HN-CPs. The HN-CP-assisted improvement in the catalytic activity was understood as oxygen activation by HN-CPs during the reduction of the oxygen species on catalytic active sites. A series of NH-CPs were tested as the second catalyst component for dual catalysis to donate electrons to oxygen to generate polarized oxygen or $O_2^{\delta-}$, including polypyrrole (**pPy**), polyaniline (**pAni**), polyindole (**pInd**), polycarbazole (**pCbz**) and polyethyleneimine (**pEI**). The number of electrons donated from NH-CP to oxygen (δ) as a single descriptor successfully characterized the effects of the NH-CPs on the ORR activity, providing a measure of the catalytic activity improvement of the Co-based catalysts with the NH-CPs. In addition to oxygen activation, from a mechanistic viewpoint, we suggest the possibility that the proton of the NH-CPs is transferred to a surface oxygen species on the active sites of the catalysts.

4.3. Results and Discussion

4.3.1. Electron donation number (δ) as the NH-CP descriptor.

pPy is a conjugated polymer that has a secondary amine structure in its heteroring moiety. Positive charges are developed every three to five monomeric units during synthesis to form charge carriers that are balanced by external anions. It was reported that atmospheric diatomic oxygen can be easily doped into **pPy** to form a charged complex $Py^{\delta+} \cdot O_2^{\delta-}$.[123] A series of HN-CPs with structural similarity to **pPy** in terms of the secondary amines and conjugated structures (**pAni**, **pInd**, **pCbz** and **pEI**) was investigated (**Figure 28a**).

We previously reported that oxygen more favorably binds to **pPy** than a Co-based perovskite oxide catalyst ($NdBa_{0.25}Sr_{0.75}Co_2O_{5.9}$).[123] Moreover, the binding energy of the diatomic oxygen species was dramatically reduced when the oxygen molecule polarized or activated by **pPy** ($O_2^{\delta-}$) was bound to the catalyst. Based on the expectation that more activated oxygen molecules on NH-CPs (i.e., a larger δ) would better accelerate the ORR kinetics, we assumed the null hypothesis that δ is not correlated with the ORR kinetics. To test the null hypothesis (more intentionally, to reject it), the number of electrons transferred from NH-CPs to O_2 (δ) was calculated for the selected NH-CPs (**Figure 28a**). Qualitatively, oxygen adsorption on NH-CP was driven by hydrogen bonding between the oxygen atom of molecular dioxygen and the hydrogen atom of the secondary amine in the most thermodynamically favored configuration (molecular configurations in **Figure 28a**). Electrons were transferred through the hydrogen bond so that the oxygen molecule to be doped into the NH-CP polymers was polarized. Quantitatively, **pPy** showed the highest δ (0.402; indicating more electron donation from the NH-CP to oxygen), followed by **pAni** (0.378), **pInd** (0.284), **pCbz** (0.276) and **pEI** (0.122). The δ is directly correlated with the charge transfer energy (HOMO level of the donor - LUMO level of the acceptor). Since the acceptor is fixed to oxygen, δ follows the order of the HOMO level of NH-CP: -3.713 eV for **pPy** > -3.716 eV for **pAni** > -4.315 eV for **pInd** > -4.632 eV for **pCbz** > -4.794 eV for **pEI** (**Figure 29**). Therefore, the NH-CP at the higher HOMO level donated a larger number of electrons to oxygen. The adsorption of more polarized oxygen with a higher δ on catalysts was thermodynamically favored, initiating the subsequent reduction process.

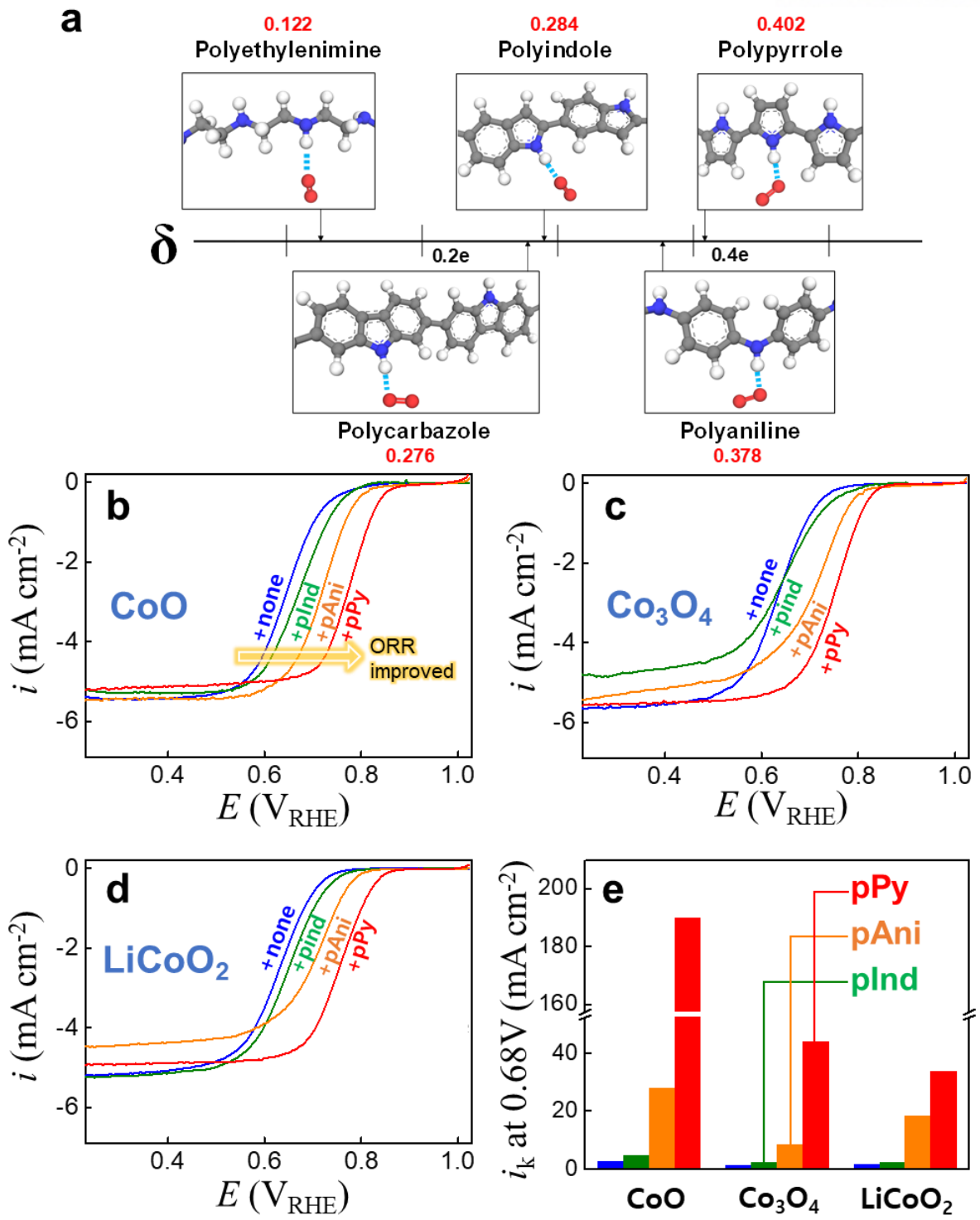

Figure 28. Improved ORR activities in the presence of NH-CPs. **(a)** The number of electrons transferred from NH-CPs to diatomic oxygen (δ). **(b to d)** The ORR polarization curves of cobalt-based electrocatalysts in the presence of NH-CPs. The overall ORR currents on catalyst-loaded disk electrodes were recorded in 0.1 M KOH (aq) when the potential was cathodically swept at 10 mV sec^{-1} and 1600 rpm. The electrocatalysts are indicated. **(e)** Kinetic current density (i_k) at 0.68 V_{RHE} (versus reversible hydrogen electrode) of the cobalt-based catalysts in the presence of NH-CPs.

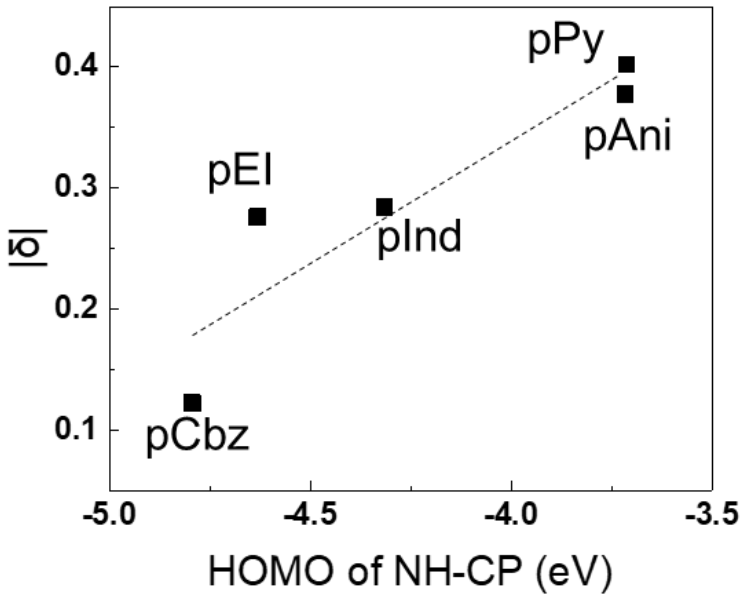

Figure 29. The correlation between the electron donation number of NH-CP to oxygen (δ) and the HOMO level of NH-CP. The value of |δ| is proportional to the charge transfer energy, which is determined by the difference between HOMO of NH-CP and the LUMO of oxygen.

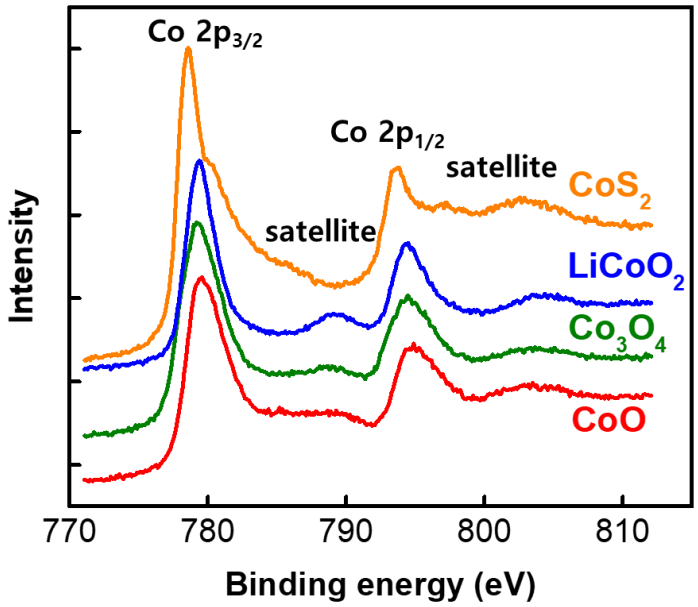

Figure 30. X-ray photoelectron Co 2p spectra of cobalt-based electrocatalysts.

4.3.2. NH-CP assisted ORR on cobalt-based oxides

As the next step following the calculation of δ as the NH-CP descriptor, the effects of the NH-CP on the ORR kinetics were experimentally quantified. The HN-CPs were tested as additional catalysts for simultaneously activating the oxygen with three different cobalt-containing electrocatalysts where cobalt is presumed to be the ORR active center: CoO, Co_3O_4 and $LiCoO_2$ (**Figure 30**). Catalysts in the presence of carbon black with NH-CP were loaded at 80:16:4 in weight (total loading = 0.8 mg cm^{-2}). The NH-CPs with $\delta > 0.28$ (**pPy**, **pAni** and **pInd**) improved the catalytic ORR kinetics of the selected catalysts, showing the δ dependency of the electrocatalytic activity (**Figure 28b** to **d** and **Figure 31** to **33**). However, **pCbz** and **pEI** at δ values less than the critical value (0.28) did not cause a kinetic gain (*inactive* NH-CPs). The active NH-CPs positively shifted the ORR polarization curves of the current versus voltage, indicating that the same turnover of the ORR was achieved with a smaller overpotential. The potential shift at 1 mA cm^{-2} as a measure of the overpotential gain was estimated at 150 mV for **pPy**, 100 mV for **pAni** and 20 mV for **pInd**. The ORR activities of the NH-CPs were negligible in the absence of catalysts. Therefore, the role of the active NH-CPs was totally dedicated to improving the activities of the catalysts.

The kinetic current density (i_k), which is responsible for charge transfer and excluding mass transfer, values of the ORR at 0.68 V_{RHE} (V versus RHE) were compared for the NH-CPs (**Figure 28e**; **Figure 34** for the turnover frequency (TOF) of the $4e^-$ ORR). For example, the ORR current of CoO increased from 2.6 mA cm^{-2} in the absence of NH-CP to 34 (**pInd**), 44 (**pAni**) and 190 mA cm^{-2} (**pPy**). The NH-CP assisted ORR activity was proportional to the δ of the NH-CPs for all cobalt-based catalysts considered (**Figure 35**). The largest overpotential gain was obtained with the highest δ, **pPy**. Therefore, the catalytic activity can be described simply by δ, which is the characteristic of NH-CP when the catalyst is fixed. Even if a monotonically increasing dependency between the overpotential gain and δ was obtained with the selected NH-CPs in this work, there is every possibility that the observed part is the left part of the volcano plot (discussed below). A strong interaction between oxygen and NH-CP (described by a too high δ) is expected to decrease the overall kinetics.

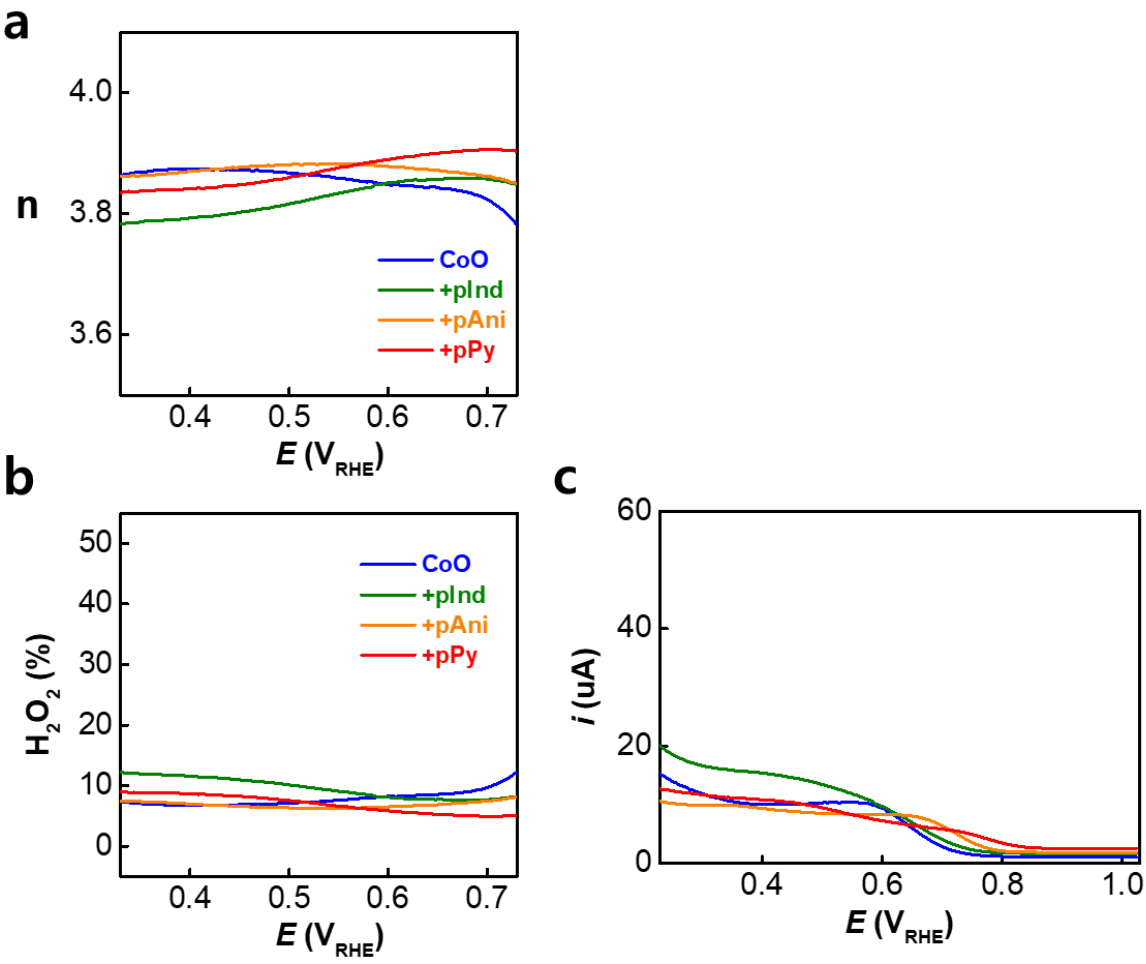

Figure 31. ORR of CoO. **(a)** Number of electron transfer (n). **(b)** production of peroxide. **(c)** Voltammogram of ring currents of ORR in 0.1 M KOH (aq) at cathodic scan (scan rate = 10 $mVsec^{-1}$; rotation speed = 1600 rpm).

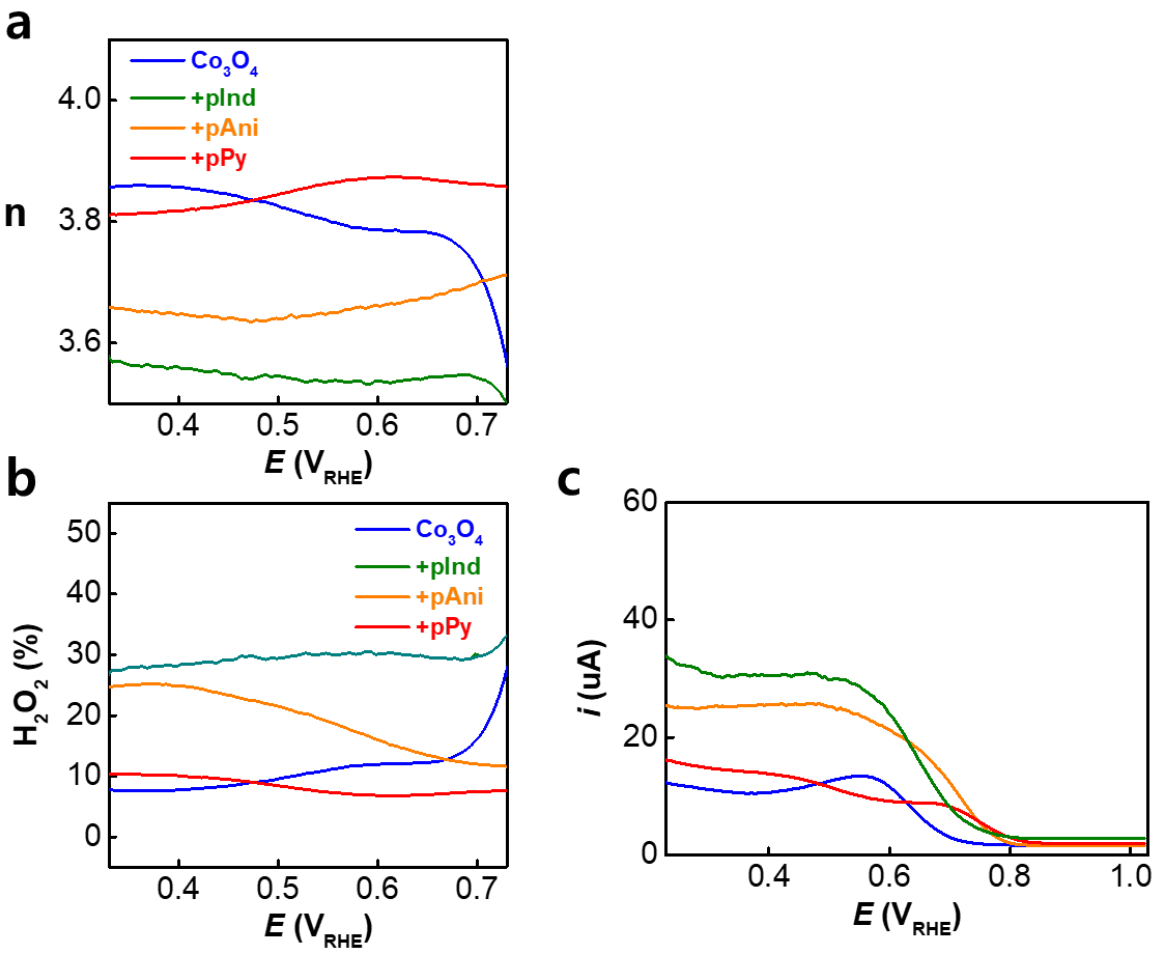

Figure 32. ORR of Co_3O_4. **(a)** Number of electron transfer (n). **(b)** production of peroxide. **(c)** Voltammogram of ring currents of ORR in 0.1 M KOH (aq) at cathodic scan (scan rate = 10 mV sec^{-1}; rotation speed = 1600 rpm).

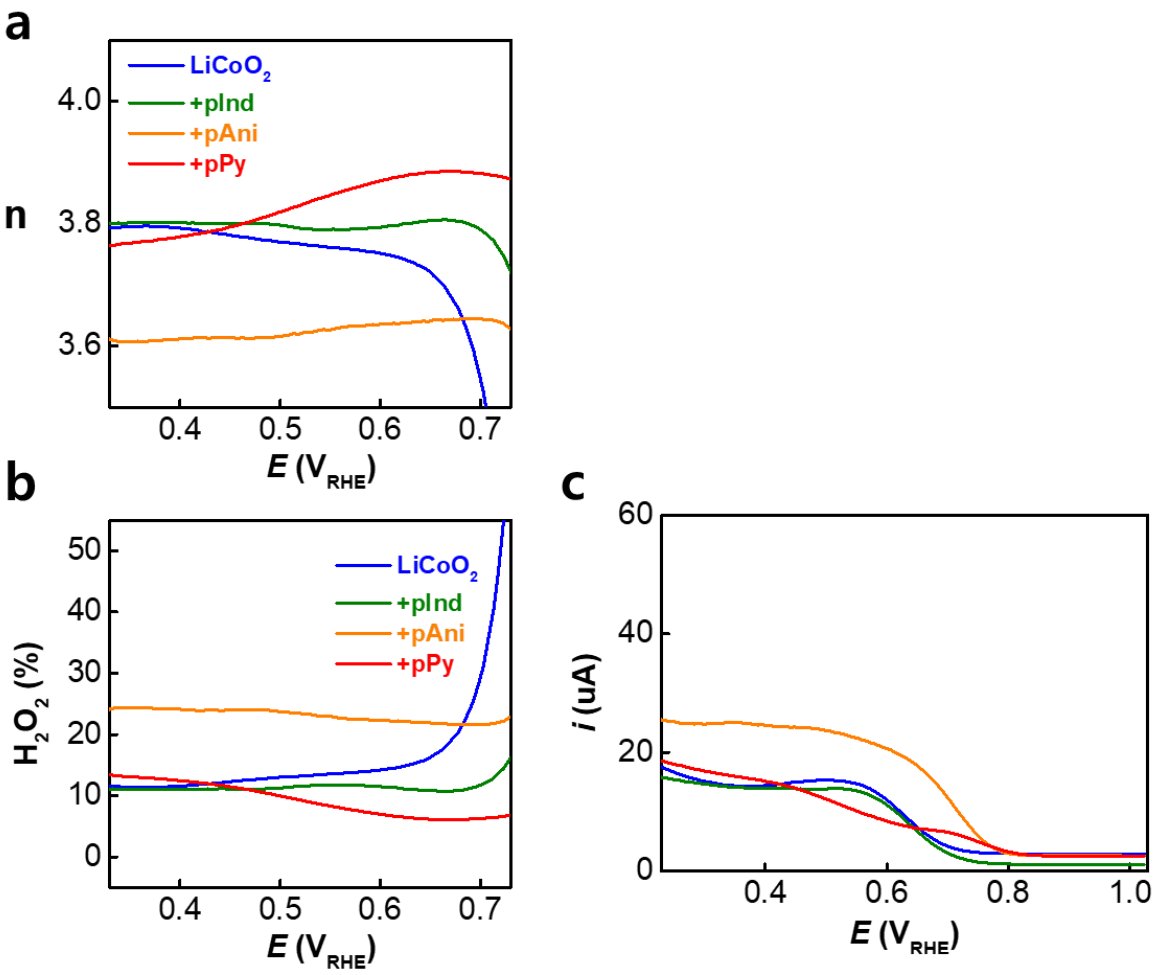

Figure 33. ORR of $LiCoO_2$. **(a)** Number of electron transfer (n). **(b)** production of peroxide. **(c)** Voltammogram of ring currents of ORR in 0.1 M KOH (aq) at cathodic scan (scan rate = 10 mV sec^{-1}; rotation speed = 1600 rpm).

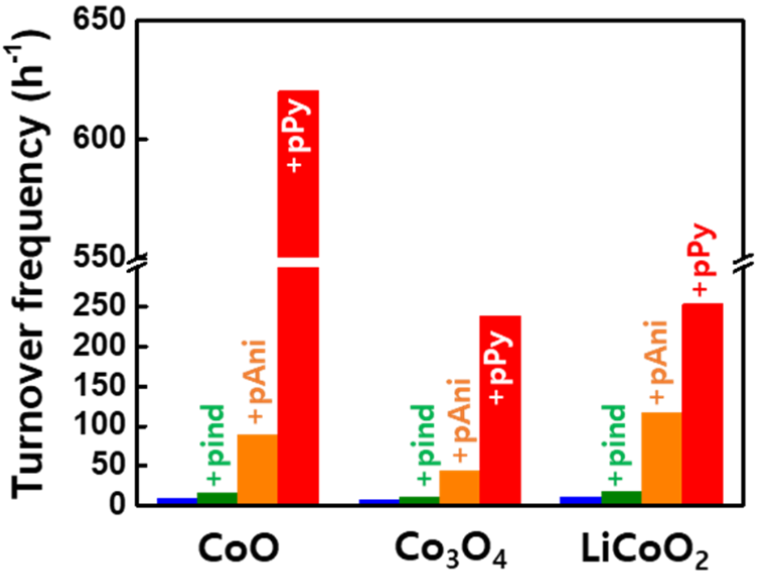

Figure 34. Turnover frequencies (TOF) of the four-electron ORR on three different electrocatalysts (CoO, Co_3O_4 and $LiCoO_2$) in the presence of NH-CPs. The TOF was calculated by:

TOF of 4e ORR = N_{Avo} x i_k x f_{4e} / F / n_{active}

where i_k = kinetic current at 0.68 V_{RHE}; N_{Avo} = Avogadro's number; F = faraday constant;

f_{4e} = fraction of $4e^-$ process = $(I_d-I_r/N)/(I_d+I_r/N)$

with I_d = disk current; I_r = ring current; N = collection efficiency;

n_{active} = number of active sites = A_{geo} / A_{active}

with

A_{geo} = geometric surface area of a catalyst under the assumption of spherical particles

= $(m_{cat} / d_{cat}) / \{4 \pi (d_{particle}/2)^3/3\}$ x $4 \pi (d_{particle}/2)^2$

m_{cat} = mass of catalyst loaded on electrode; d_{cat} = density of catalyst

$d_{particle}$ = particle size (100nm)

A_{active} = area of unit cell (100) / the number of cobalt in unit cell (100) under assumption of (100) termination on the surfaces

= $(4.26 Å)^2/2$ for CoO, $(8.06 Å)^2/4$ for Co_3O_4 and (2.44 Å x 3.42 Å)/3 for $LiCoO_2$

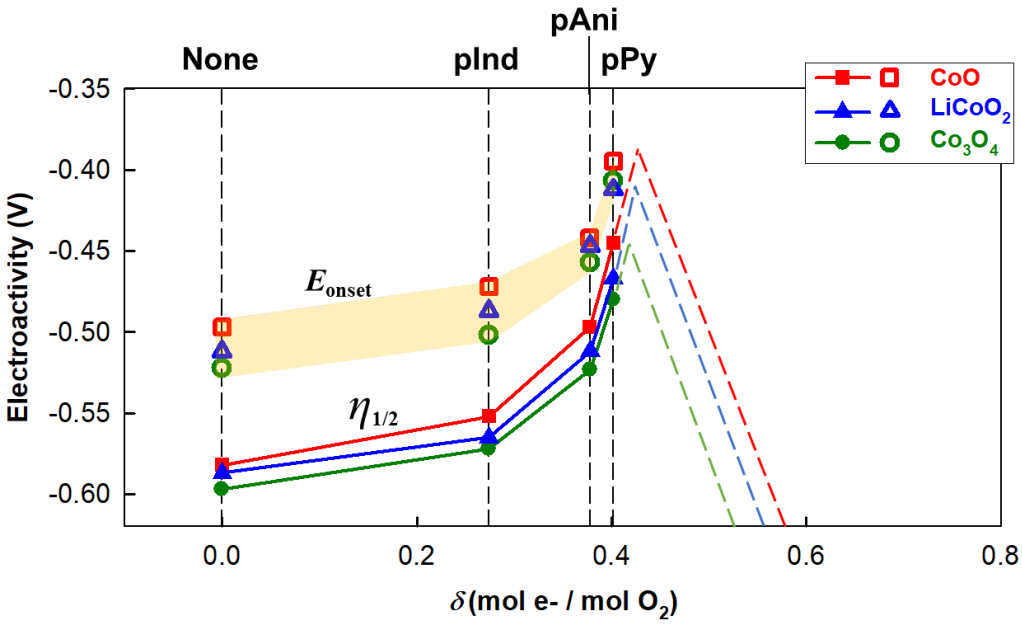

Figure 35. The δ-dependency of the ORR activity. The half-wave overpotential ($\eta_{1/2}$; filled symbols) or the onset potential (E_{onset}; open symbols) was used as the ORR activity measure in the ordinate. The number of electrons donated by the NH-CP to oxygen, δ, was used as the NH-CPs descriptor in the abscissa. Three different cobalt-based oxides (CoO, $LiCoO_2$ and Co_3O_4) were tested as the ORR electrocatalysts in the presence of three different HN-CPs (**pPy**, **pAni** and **pInd**).

4.3.3. Mechanism of NH-CP assisted ORR on cobalt-based catalyst

Even if δ is a descriptor that allows a prediction of the effect of NH-CP on the catalytic activity of ORR catalysts, the mechanism of the dual catalysis must be investigated to determine why the descriptor represents the multistep process of the ORR. According to the thermodynamic calculations, the additional activation of oxygen, receiving partial charge from pPy, are much favored in the reduction process compared to its single activation by CoO (**Figure 36 to 38**).

The protonation of the diatomic oxygen intermediate on the catalyst (formation of *OOH) was the rate determining step (RDS) of the overall ORR process in the absence of **pPy** (**Figure 39** and **Figure 40**). The endothermic relative energy change, ΔE(*OO→*OOH), was estimated at +1.05 eV during the *OO-to-*OOH process. In the presence of **pPy**, on the other hand, the endothermic relative energy change decreased significantly to +0.27 eV. The energy savings of this *OO-to-*OOH step lowers the free energies of the following steps.

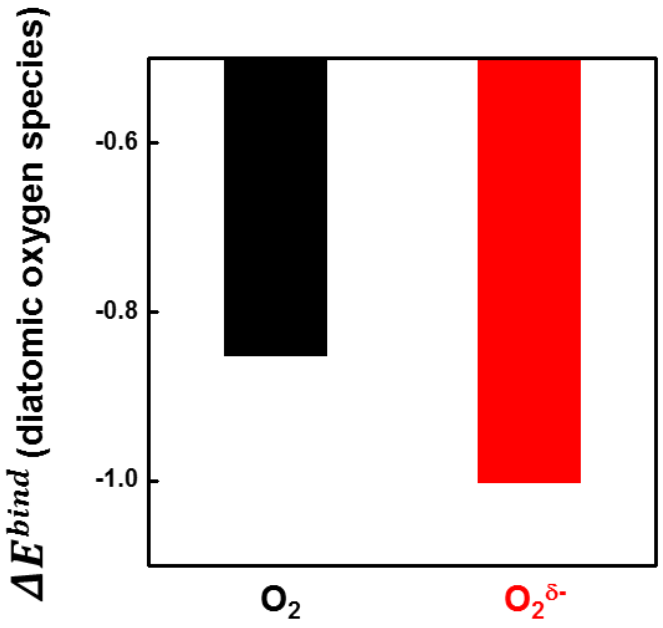

Figure 36. The binding energy (ΔE^{bind}) of diatomic oxygen species (the neutral or activated oxygen molecules, O_2 or $O_2^{\delta-}$) to CoO. The activated oxygen is generated in the presence of **pPy**. The more negative value indicates the stronger binding of oxygen molecule to CoO.

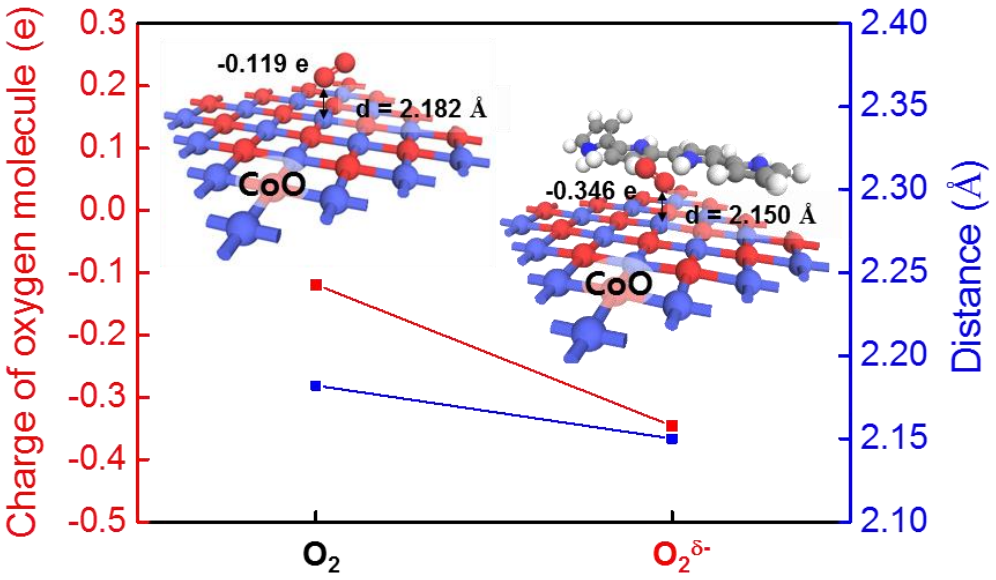

Figure 37. Adsorption of the neutral and partially charged diatomic oxygen species (O_2 and $O_2^{\delta-}$) on CoO catalyst. Bader charges developed in the diatomic species and the distance between an oxygen atom of the diatomic oxygen species and a cobalt atom of the surface lattice of CoO were indicated. The activated diatomic oxygen ($O_2^{\delta-}$) was generated in the presence of **pPy**.

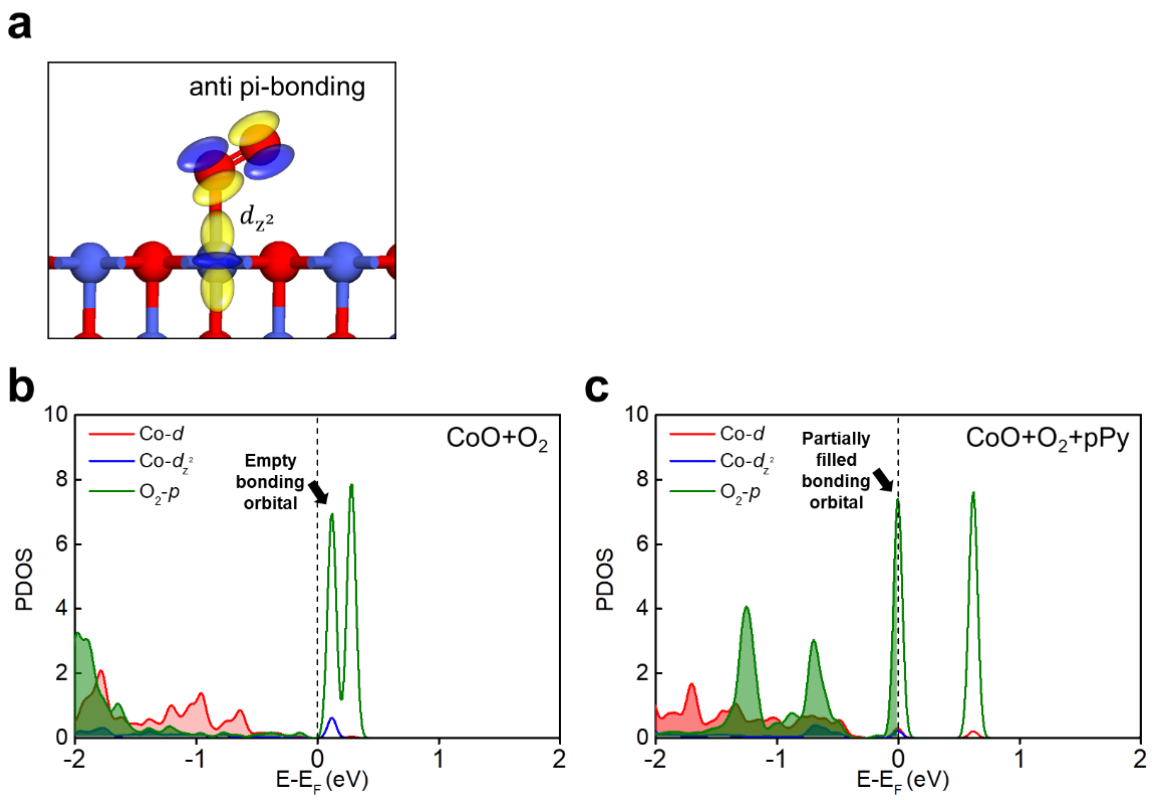

Figure 38. Hybridization between d_{z^2}-orbital of Co and *p*-orbital of O_2 molecule (*i.e.*, anti pi-bonding state near Fermi level, E_F) at CoO surface. **(a)** Molecular representation: red sphere = oxygen; blue sphere = cobalt; oval = orbital. **(b and c)** Partial density of states (PDOS) of cobalt of CoO and adsorbed O_2 in the absence of **pPy** (**b**) and in the presence of pPy (**c**): red = total *d*-orbital of Co bonded to O_2; blue = d_{z^2}-orbital of Co bonded to O_2; green = *p*-orbital of O_2. The d_{z^2}-orbital of Co and the *p*-orbital of O_2 are hybridized near E_F (indicated by arrows). The hybridized bonding orbital near E_F was partially filled when the neutral oxygen molecule (O_2) was activated to be the polarized oxygen molecule ($O_2^{\delta-}$) by the aid of **pPy**. The binding of the diatomic oxygen species to CoO surface is strengthened by the partially filled bonding orbital.

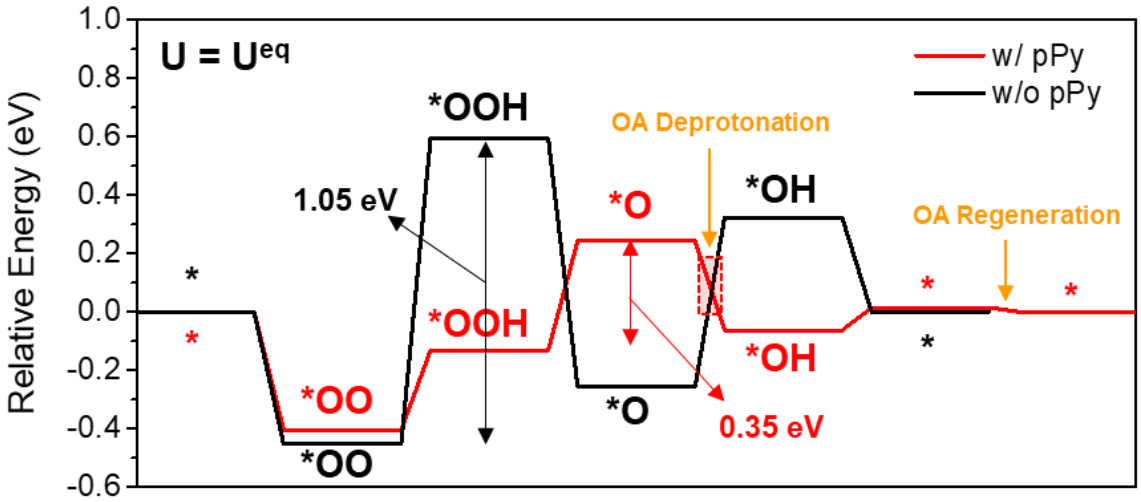

Figure 39. Energy diagram along ORR mechanism at the equilibrium potential ($U = U_{eq}$): main catalyst = CoO; additional catalyst = pPy. The pPy-present system (red) was compared with the pPy-absent system (black). The energy gap of the rate determining step of each system was indicated: 0.35 eV for the pPy-present system versus 1.05 eV for the pPy-absent system.

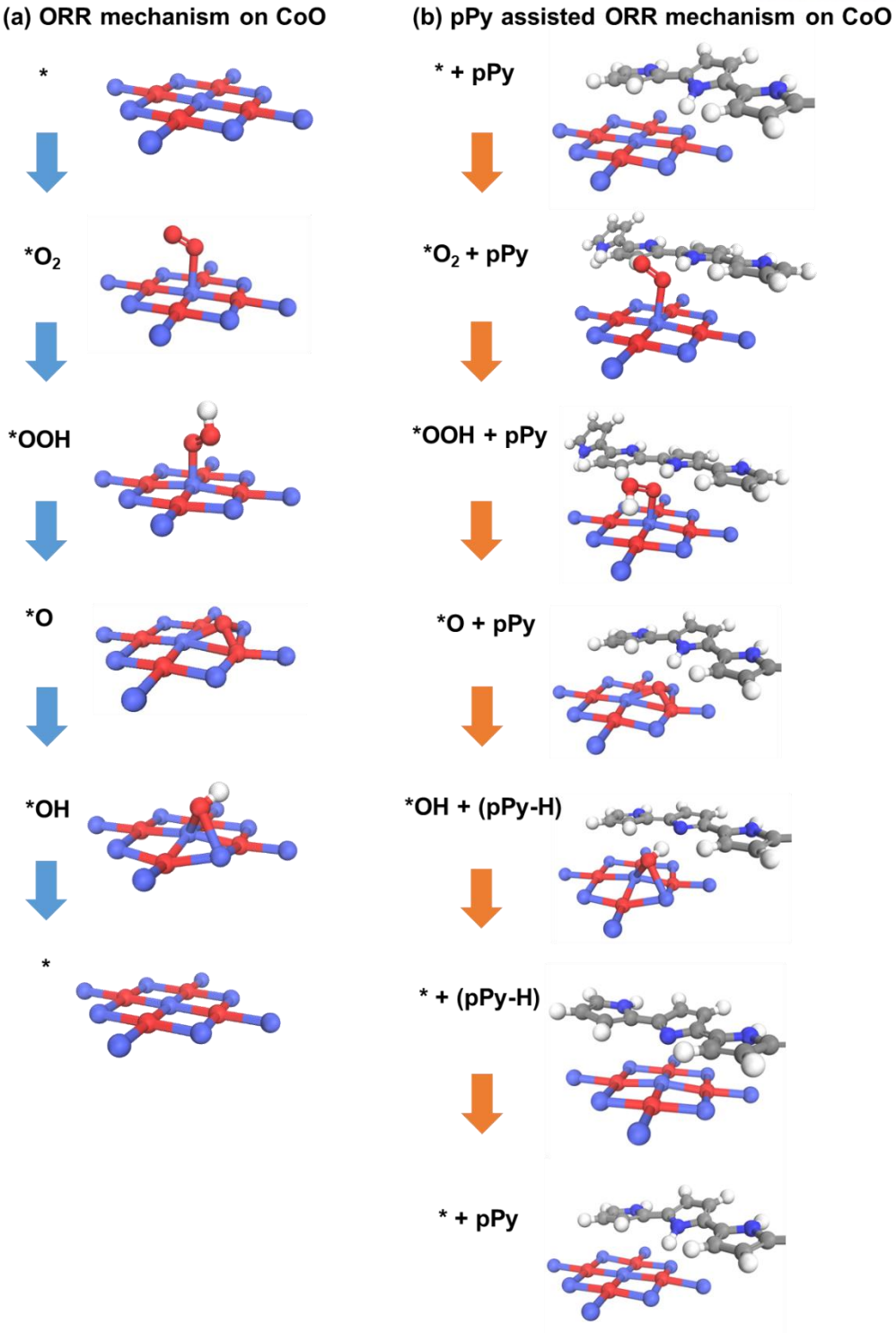

Figure 40. Molecular representation of the intermediate states along ORR mechanism on CoO electrocatalyst in the absence versus presence of **pPy** as the additional catalyst.

After the e^-/H^+ transfer step to form the surface peroxide (*OOH), interestingly, the *O formation in the presence of NH-CP was not more thermodynamically favored than that in the absence of NH-CP (the relative energy diagram along the mechanism at the equilibrium potential and the intermediates of the ORR in **Figure 39** and **Figure 40b**, respectively). The thermodynamic state of *OOH stabilized by the partial charges of the electrons transferred from the NH-CP (δ-) changed the *OOH-to-*O step from an exothermic process in the absence of NH-CP ($\Delta E_{*O} - \Delta E_{*OOH} < 0$) to an endothermic process in the presence of NH-CP ($\Delta E_{*O} - \Delta E_{*OOH} > 0$). As a result, the NH-CP switched the RDS of the overall ORR from *OOH formation ($\Delta E_{*OOH} - \Delta E_{*OO}$ = +1.05 eV in the absence of **pPy**) to *O formation ($\Delta E_{*O} - \Delta E_{*OOH}$ = +0.35 eV in the presence of **pPy**) at the equilibrium potential U_{eq} (**Figure 39**).

In the following step, we suggest that the surface single oxygen (*O) is protonated by the proton from the secondary amine of NH-CP (**Figure 41a**). It has been reported that HN-CPs are easily and reversibly deprotonated and protonated in aqueous solution.[124-127] In addition, the possibility of participating proton donor/acceptor in electrocatalytic reaction, ORR and OER, was suggested.[128] The proton-to-deuterium exchange confirmed the possibility of easy deprotonation of the HN-CPs (**Figure 42**). The wavenumber of the peak assigned to the N-H in-plane vibration mode of the amine of pyrrole (C_4H_5N) in the H_2O environment shifted from 1050 cm^{-1} to 750 cm^{-1} when pyrrole was dissolved in D_2O, confirming the conversion of C_4H_5N to C_4H_5D. The pH dependency of the overpotential gain by the NH-CP also supported that the deprotonation of the amine of the NH-CPs would affect the ORR kinetics (**Figure 41b**). The overpotential improvement by **pPy** at pH 7 was significantly larger than that of pH 13: the difference of the half-wave potentials between the absence and presence of **pPy** = 183 mV at pH 7 > 146 mV at pH 13. Additionally, two counter examples were tested to confirm that the deprotonation of NH-CPs is required. First, polythiophene did not improve the ORR kinetics because the sulfur of the conjugated polymer does not contain hydrogen that can be deprotonated (**Figure 43**). Second, the effects of pPy on ORR were not significant after a few cycles of voltammograms in an aprotic organic solvent (acetonitrile in **Figure 44**).

There are four different surface species in the ORR mechanism that are required to be protonated: *OO → *OOH, *OOH → *O + H_2O, *O → *OH and *OH → * . We determined the step in which the NH-CP deprotonation process is involved by comparing the energy required for the proton transfer from NH-CP to the surface intermediate between the targeted steps (**Figure 41**). The surface single oxygen (*O of step (5) to (7)) was the most thermodynamically favorable site to obtain a proton from the amine NH-CPs. Subsequently, the deprotonated NH-CP is presumed to be regenerated at the last step (the NH-CP regeneration step in (8) of **Figure 41a**). The stability of **pPy** was guaranteed along 500-time repeated voltammetric cycles, indicating that there was no serious problem in regenerating protonated pPy (**Figure 45**).

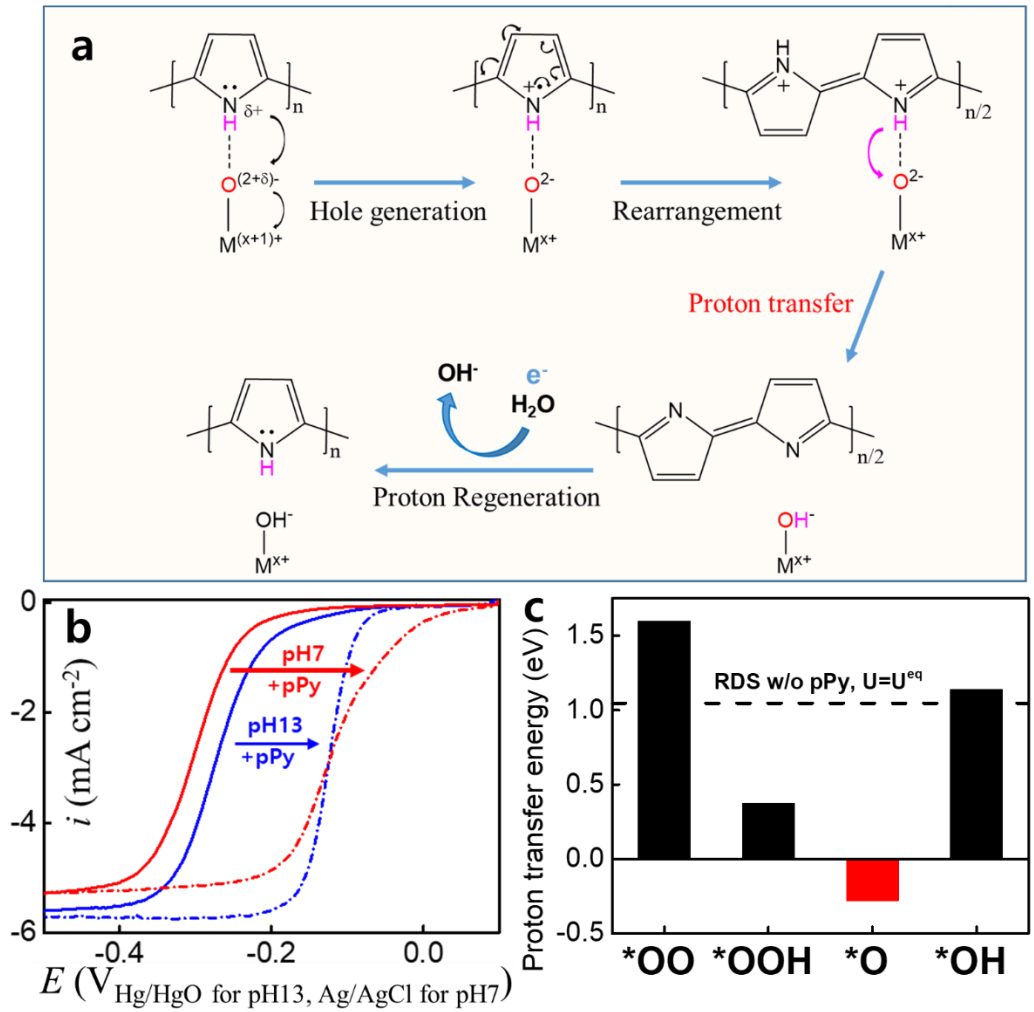

Figure 41. The mechanism of proton transfer in NH-CP assisted electrocatalysis for ORR. **(a)** A suggested mechanism of proton transfer from NH-CP to oxygen adsorbate in NH-CP assisted ORR on cobalt-based catalysts (M=active site of cobalt-based catalysts). **(b)** ORR polarization curves of CoO electrocatalyst without (solid lines) or with **pPy** (dashed lines) in a buffer solution at pH 7 (red) and 0.1 M KOH (blue; pH 13). Potential was cathodically scanned at 10 mV sec^{-1} while disk electrodes were rotated at 1600 rpm. **(c)** Energy required for the proton transfer from **pPy** to the four different intermediate states generated on CoO during the ORR.

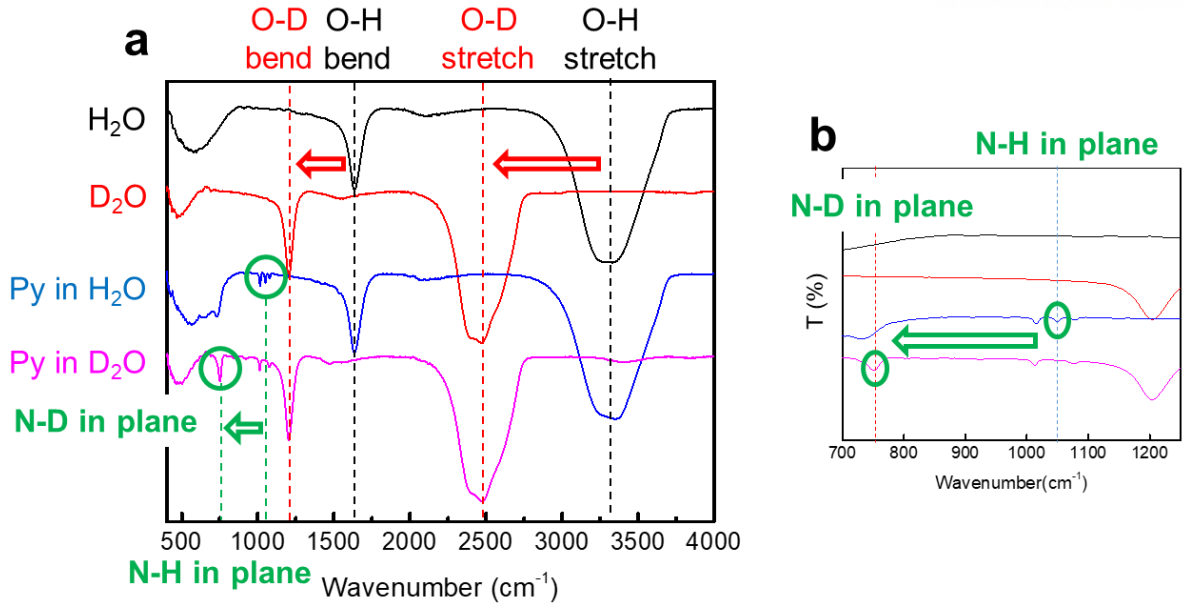

Figure 42. Deutriation of pyrrole. **(a)** Fourier-transform infrared (FTIR) spectra of H_2O (black), D_2O (red) and pyrrole dissolved in H_2O (blue) and D_2O (magenta). **(b)** The closer look of the FTIR spectra a between 700 cm^{-1} and 1250 cm^{-1}. The wavenumber of the peak assigned to N-H in-plane vibration mode shifted from 1050cm^{-1} to 750cm^{-1} after deutriation.

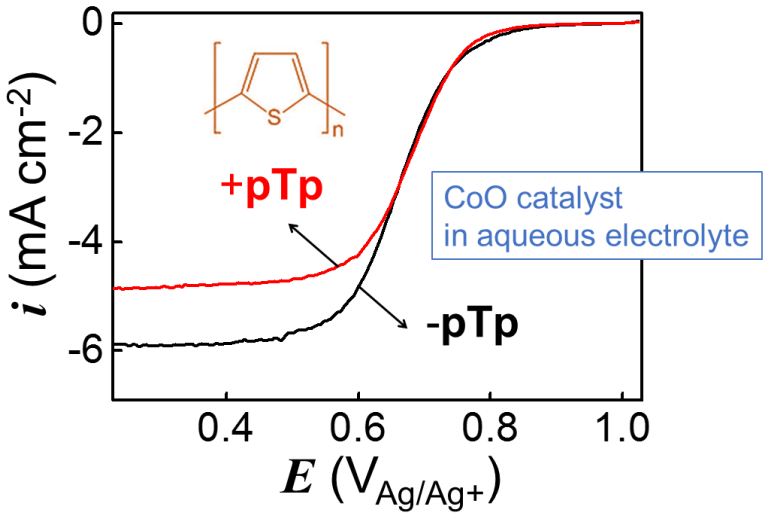

Figure 43. ORR activities of CoO in the presence of polythiophene (pTp). Linear sweep voltammograms of the ORR disk current were obtained in 0.1 M KOH (aq) at cathodic scan (scan rate = 10 mV sec-1; rotation speed = 1600 rpm). Black = CoO; Red = CoO + pTp.

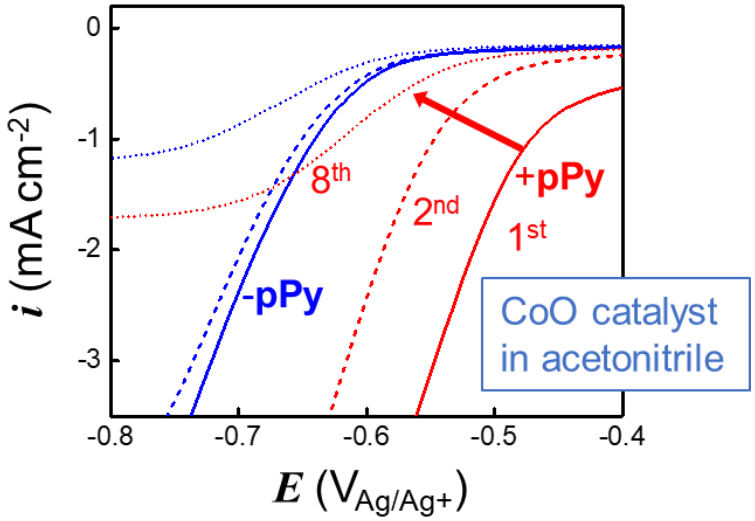

Figure 44. ORR activities of CoO in an aprotic solvent. Cyclic voltammograms of the ORR disk current at 1st (solid line), 2nd (dashed line) and 8th cycle (dotted line) were obtained in 0 .1 M $LiClO_4$ in acetonitrile at cathodic scan (scan rate = 20 mV s^{-1}). Blue = CoO; Red = CoO + pPy.

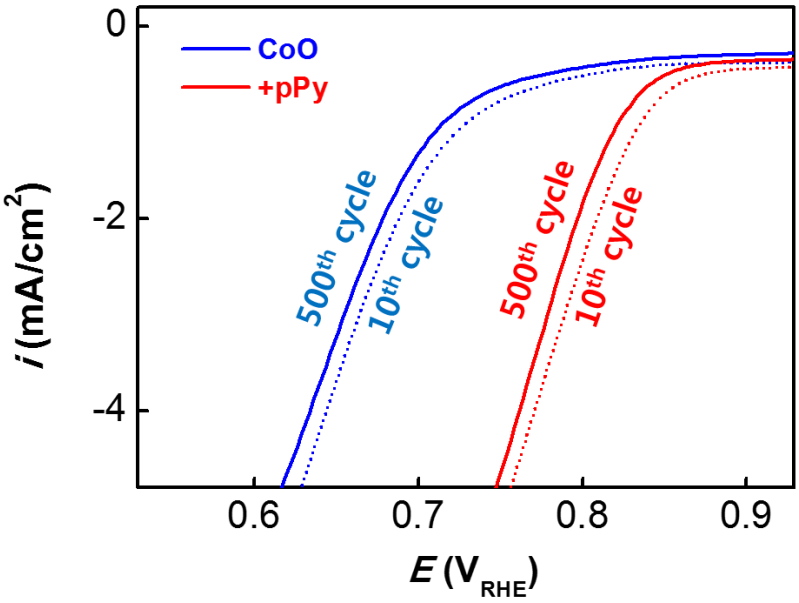

Figure 45. Stability. The ORR polarization curves of the CoO electrocatalyst without (blue) or with pPy (red) at 10th cycle (dashed lines) and 500th cycle (solid lines). The potential was cathodically scanned at 50 mV sec^{-1} while the disk electrodes were rotated at 1600 rpm. Half-wave potential was shifted about 10mV during 500 cycles in both cases.

4.4.4. The RDS at reductively biased overpotentials ($U < U_{eq}$)

We discussed above the mechanism of the *NH-CP assisted* ORR catalysis with the relative energy diagram at the equilibrium potential, U_{eq}. To obtain a significant ORR current, however, a potential more negative than the equilibrium potential ($U < U_{eq}$) needs to be applied (**Figure 28b** to **d**). To determine which step in the proposed mechanism is the RDS at the applied potential, the ORR polarization curves were interpreted by the Tafel equation. The Tafel slopes (b) were mainly determined by the NH-CPs rather than the catalysts, especially in the high-δ cases (**Figure 46**; NH-CP-effective region): b = 65 to 68.5 mV dec^{-1} for **pPy** and 73.9 to 75.9 mV dec^{-1} for **pAni**. However, the Tafel slopes of the ORR on electrocatalysts in the presence of the low-δ NH-CP s or in the absence of NH-CPs did not converge to one value so that the catalyst-dependency of b could not be neglected (NH-CP-ineffective region): b = 77.1 to 89.5 mV dec^{-1} for **pInd** and 81.6 to 86.2 mV dec^{-1} for no NH-CPs. The identical Tafel slopes for a fixed NH-CP in the NH-CP-effective situations indicate the NH-CP-dependency of the RDS of the overall ORR kinetics.[59-62] Therefore, it is reasonable to consider that an active role of the NH-CP, such as a significant structural change, is involved in the RDS. The proton transfer step (**Figure 41a**) is a highly feasible RDS in the applied potential situation where the surface single oxygen (*O) is protonated by the proton from the secondary amine of the NH-CP.

The energy diagram at a biased voltage between the initial and final states (U = 0 V_{NHE}) supported the proton transfer step as the RDS (**Figure 47a**) in that this step had the smallest downhill gap among steps. When compared with the energy diagram at U_{eq} (**Figure 39**), the RDS changed from the surface single oxygen formation step (*OOH to *O) at U_{eq} to the proton transfer step (*O to *OH) at 0 V_{NHE}. However, there was no change in the RDS for the NH-CP-absent cases (RDS = the surface peroxide formation step) independent of whether the system was biased or not (**Figure 47a** versus **Figure 39**). In other words, therefore, the NH-CP changed the RDS from *the surface peroxide formation step* (*OO to *OOH in the absence of NH-CP) to *the proton transfer step* (*O to *OH in the presence of NH-CP) at biased potentials.

The overpotential dependency of the number of electrons transferred (n) of NH-CP assisted ORR catalysis, different from that of conventional catalysis, was successfully explained by the suggested RDS. The ORR proceeds via 4e and 2e pathways to produce oxide and peroxide, respectively. The value of n for the overall ORR is estimated to be between 2 and 4 as the average value of those two processes. In the absence of NH-CP, practically, the value of n increases as the potential is moved to a more negative value (larger overpotential) (**-pPy** in **Figure 47b**). Interestingly, on the contrary, the value of n decreased significantly with the increasing overpotential in the presence of NH-CP (**+pPy** in **Figure 47b**). The different overpotential-dependencies of n are understood by considering the natures of the

steps following the surface peroxide species. For conventional ORR catalysis in the absence of NH-CPs, the surface peroxide (*OOH) is released as a form of peroxide (HO_2^-) to the electrolyte without electrons (*chemical* step or C step) or alternatively converted to a surface hydroxyl (*OH) via the electrochemical route (E step). The kinetics of the E step are accelerated at larger overpotentials (more negative potentials away from the equilibrium potential of the ORR), while the overpotential is not relevant to the kinetics of the C step (**Figure 48**). Therefore, the 4e transfer pathways are preferred so that *n* increases with increasing overpotential. For ORR dual catalysis in the presence of NH-CPs, however, the E step of *OH formation is limited by another C step of the proton transfer. As the overpotential was increased, the formation of the surface peroxide was kinetically increased without an increase in the rate of the chemical conversion from *OOH to *OH (**Figure 48**). Consequently, the 2e pathway is encouraged at high overpotentials.

The ORR dual catalysis in the presence of NH-CPs showed potential-dependent Tafel slopes, while the NH-CP-absent catalysis was well described by a single Tafel slope (**Figure 46c**). That is, the introduction of NH-CPs curved the linear ORR polarization data of $LiCoO_2$ in the Tafel plot. The $LiCoO_2$ data were described by a single slope at 81.6 mV dec^{-1}, while the data in the presence of **pPy** are represented by 68.5 mV dec^{-1} for the small overpotential region (> 0.77 V_{NHE}), 90.9 mV dec^{-1} for the middle overpotential region (between 0.73 V_{NHE} and 0.77 V_{NHE}) and a larger value than the previous two slopes for the high overpotential region (< 0.73 V_{NHE}). This change in the Tafel slope along with the potential has been observed for conventional ORR catalysis on platinum.[60, 129] The surface coverage (θ) of the intermediates on platinum is responsible for the multiplicity of the Tafel slopes at 60 and 120 mV dec^{-1}.[130] From the same coverage viewpoint, the Tafel slope (*b*) for ORR dual electrocatalysis is described by $b \sim (n\alpha)^{-1} = n^{-1}(2 + \theta_{*OH} - 2\theta_{*OO} - \theta_{*OOH})^{-1}$, where α is the apparent transfer coefficient. The proton transfer steps were assumed to be the RDS for derivation (derivation of the apparent transfer coefficient (α) in the Supporting information). According to the equation, the accumulation of the surface peroxide species (*OOH) is responsible for the increase in b with increasing overpotential (or decreasing potential to a negative value). This explanation is consistent with the above discussion that the C step of the proton transfer limits the 4e pathway to decrease the *n* value at high overpotentials (**Figure 46a**).

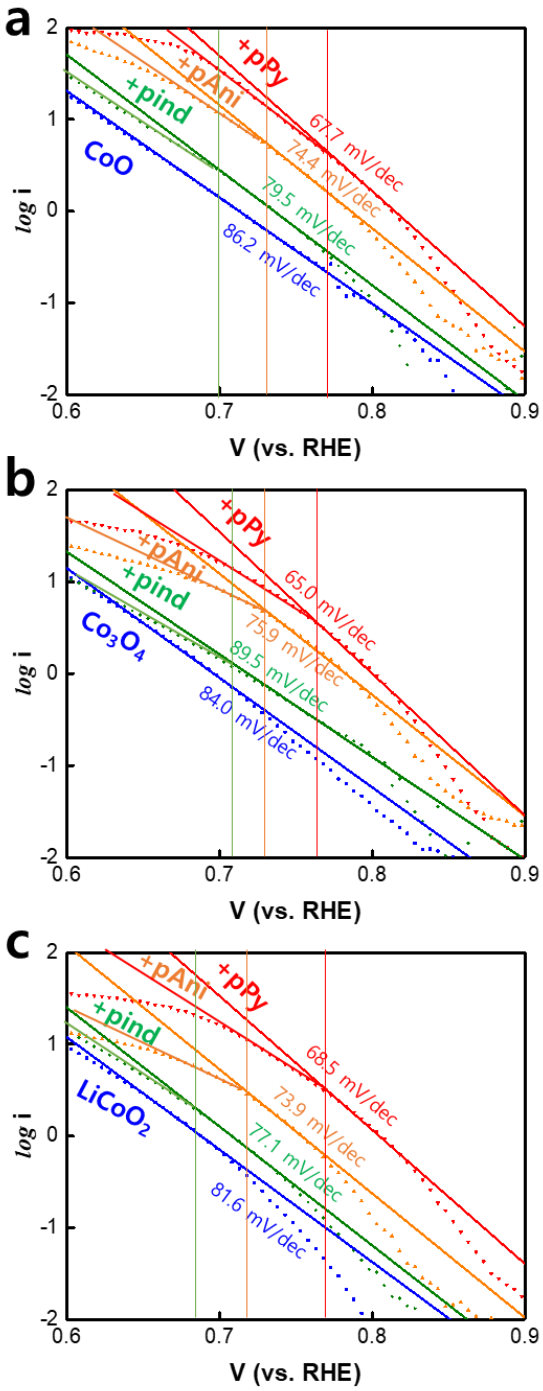

Figure 46. Tafel plots of ORR on catalysts in the absence and presence of NH-CPs. **(a)** CoO. **(b)** Co_3O_4. **(c)** $LiCoO_2$.

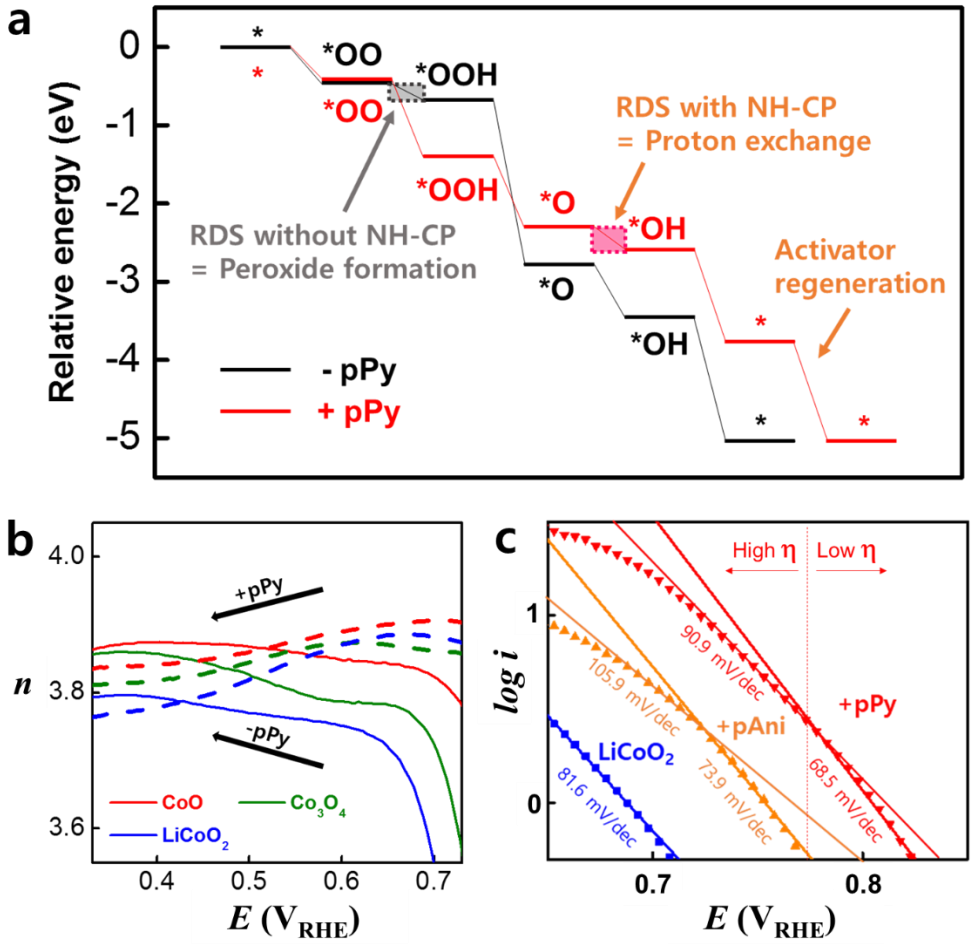

Figure 47. The rate determining step (RDS) of NH-CP assisted ORR catalysis at biased potentials. **–pPy** = conventional catalysis in the absence of NH-CPs; **+pPy** = dual catalysis in the presence of **pPy** as one of the NH-CP. **(a)** Energy diagrams along the ORR mechanism. The energies of the intermediate and final states relative to the first state were calculated by DFT. The final state was biased relative to the first state by $U = 0$ so that the energy gap between the first and final states was 5.04 eV = | $(U - U_{eq})$ x 4e | = | (0 V – 1.26 V) x 4e |. The value of U_{eq} was estimated at 1.26 V by DFT, which is a measure of the standard reduction potential of the ORR versus normal hydrogen electrode (practically known as 1.23 V versus NHE). (**b**) The number of electrons transferred (n) in the overall ORR process on the four different cobalt-based catalysts. (**c**) Tafel plots for the ORR on $LiCO_2$ in the presence of the three different NH-CPs.

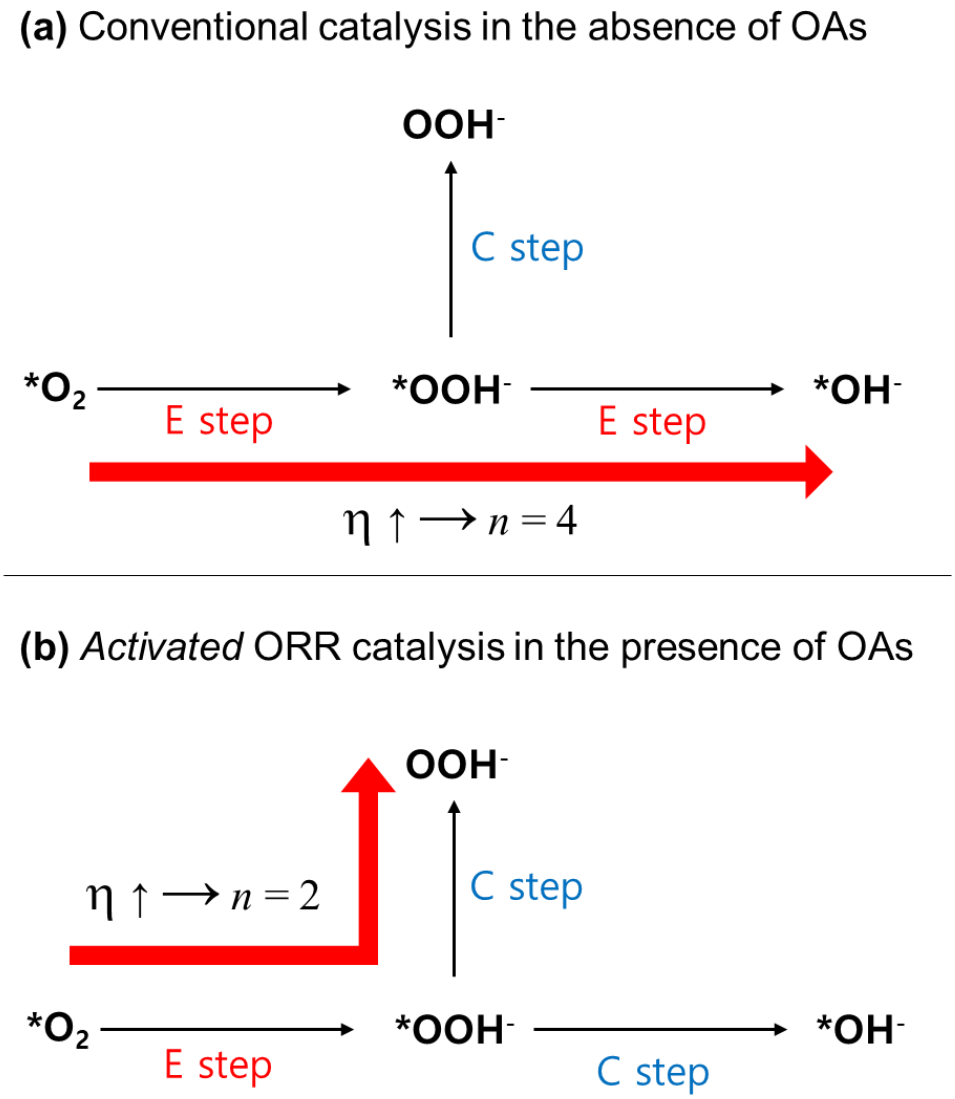

Figure 48. The overpotential (η) dependency of the number of electron transferred (n). **(a)** Conventional ORR catalysis in the absence of OA. **(b)** NH-CP-assisted ORR catalysis in the presence of OA. The 2e transfer becomes preferred in the catalysis as the applied overpotential increases.

4.3.5. Additional catalyst-described volcano plots for the dual catalysis

Volcano plots were used to show the dependency of the ORR activity on a catalyst descriptor.[6] The binding energy of monoatomic oxygen (*O resulting from the dissociative adsorption of diatomic oxygen) or hydroxide (*OH generated by the protonation of *O) to the active site of the catalysts (ΔE_O or ΔE_{OH})[6, 131] as well as the d band center of the catalysts[132] have been used as the *catalyst* descriptor. In the presence of NH-CPs, the additional catalyst descriptor, in addition to the main catalyst descriptor, is required for the dual catalysis. The electron donation number of the NH-CPs to oxygen, δ in O_2 to $O_2^{\delta-}$, could be used as the NH-CP descriptor. The ORR activity measure was plotted versus δ in the additional catalyst version of the volcano plot (**Figure 35**). The onset potential (E_{onset}) or the half-wave overpotentials ($\eta_{1/2}$) were used as the ORR performance measure.

Both the NH-CP dependency and the catalyst dependency of the ORR electrocatalytic activities were found in the volcano plot (the left part of **Figure 35**). The ORR activity was improved for all cobalt-based catalysts tested in this work (CoO, $LiCoO_2$ and Co_3O_4), as the NH-CPs donated more electrons to the diatomic oxygen (**pPy** > **pAni** > **pInd** for δ in the NH-CP dependency by horizontal comparison in the volcano plot of **Figure 35**). The NH-CPs having $\delta < 0.2$ did not affect the catalytic activity of the catalysts (NH-CP-ineffective region). At a fixed NH-CP (catalyst dependency by vertical comparison in the volcano plot of **Figure 35**), the $\eta_{1/2}$ representing the ORR activity at higher overpotentials (relatively higher than the onset potential) was determined by the ORR activity of the catalysts in the absence of the NH-CPs. For example, Co_3O_4 was inferior to CoO and $LiCoO_2$ in terms of $\eta_{1/2}$ when the same NH-CP was present (even absent) with the catalysts. However, the catalytic activity of the poorest catalyst Co_3O_4 in the presence of **pPy** exceeded that of CoO in the absence of NH-CPs.

Interestingly, the onset potential (E_{onset}) representing the ORR electrochemical activity at small overpotentials (relatively smaller than the half-wave potential) was determined with the NH-CP s and was independent of the catalyst (**Figure 49**): E_{onset} = -0.404±0.008 V (**pPy**), -0.449±0.007 V (**pAni**) and -0.487±0.015 V (**pInd**). The difference in the E_{onset} of the catalysts with a fixed NH-CP is significantly smaller than that of $\eta_{1/2}$, especially for the high-δ NH-CPs (**pPy** and **pAni**): the standard deviation of E_{onset} versus $\eta_{1/2}$ = 0.007 V versus 0.015 V for **pPy** and 0.006 V versus 0.011 V for **pAni**. From the NH-CP dependency and the catalyst independency of E_{onset}, therefore, we can easily expect that an NH-CP cannot improve the catalytic activity of a catalyst whose E_{onset} is more positive than the values obtained from other catalysts in the presence of the NH-CP.

The additional catalyst-described volcano plot (**Figure 35**) was unfinished in that we have not yet found the high-δ NH-CPs (higher than **pPy**), which would be placed on the right lower section of the plot (dashed lines in **Figure 35**). As discussed above, a δ too high is expected to decrease the catalytic activity because the strong binding of oxygen to the NH-CP will discourage the transfer of the adsorbed

oxygen species on the NH-CP to the active site of the catalyst (step (2) in **Figure 41a**).

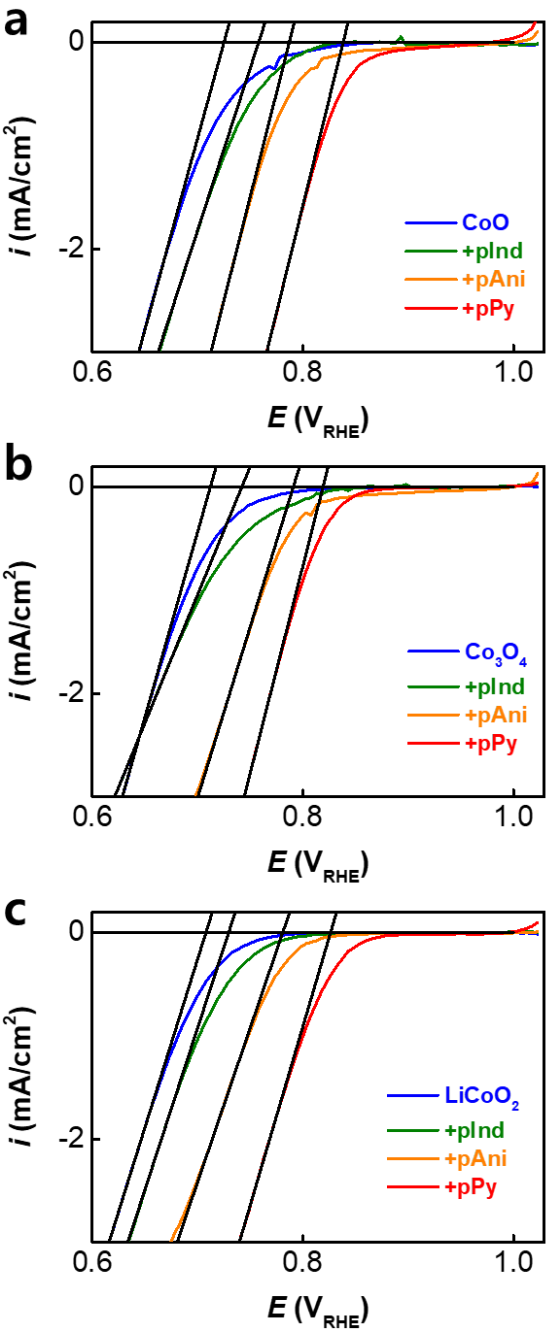

Figure 49. The onset potential (E_{onset}) in the linear sweep voltammograms for investigating the ORR polarization. The E_{onset} was read from the point of intersection between the abscissa at zero current and the line tangent to the polarization curve at high overpotential region. **(a)** CoO, **(b)** Co_3O_4 and **(c)** $LiCoO_2$

4.4. Experimental

Materials.

Commercially available cobalt-containing materials, including CoO, Co_3O_4 (Sigma-Aldrich) and $LiCoO_2$ (Umicore), were used as the ORR catalysts. Carbon black (C; Akzo Nobel Ketjen black 600JD) was used as the conducting agent included in the catalyst layer. NH-CP was introduced to the catalyst layers in the form of NH-CP loaded carbon black (NH-CP/C). pPy/C and pAni/C (20 wt. % NH-CP) were used as received from Sigma-Aldrich (530573 and 530565, respectively). pInd/C (20 wt. % NH-CP) was prepared by electropolymerizing the corresponding monomer (150 mg indole in 100 ml of 0.1 M NaCl (aq)) on carbon black. Three electrode configurations were used for the electropolymerization: the rotating ring-disk electrode (RRDE; 0.1256 cm^2) as the working electrode, platinum wire as the counter electrode and Ag/AgCl as the reference electrode. The catalyst layer, including carbon black (described in the catalyst layer section), was loaded onto the disk electrode of the RRDE. Current at 1 mA cm^{-2} was applied in the nitrogen-purged monomer-containing electrolyte for 20 seconds **(Figure 50)**. The doping level of pInd was determined by the charge consumption for polymerization and the charge of doping or dedoping of the polymer in a cyclic voltammogram (**Figure 51**): A chloride ion was doped every 5 monomeric units of pInd.

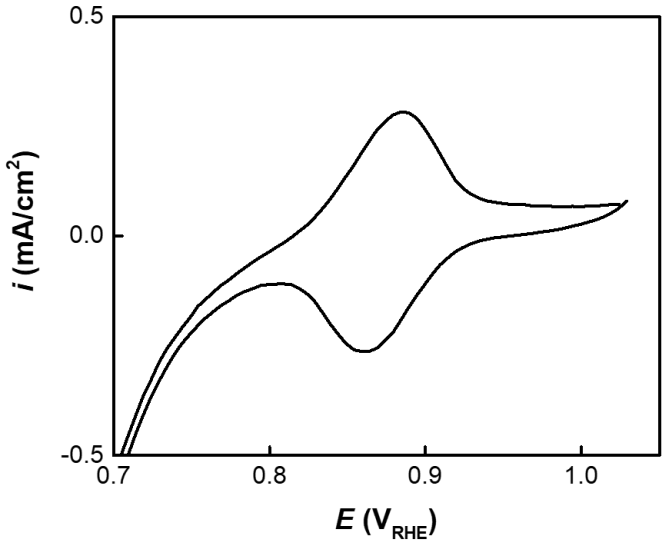

Figure 50. Cyclic voltammogram of polyindole redox reaction on catalyst-loaded electrode in oxygen saturated 0.1 M KOH(aq) at 10mV/s of scan rate.

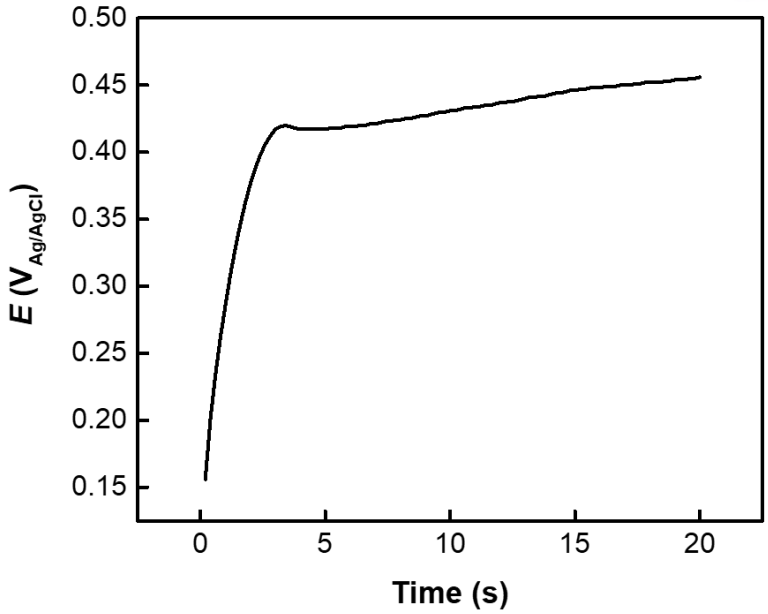

Figure 51 Chronoamperometry for electro-polymerization of indole on carbon electrode at 1 mA/cm^2 of constant current density.

Catalyst layers.

First, 16 mg catalyst and 4 mg carbon black (NH-CP-free or NH-CP-containing) were dispersed in 0.9 ml of a mixture of ethanol and 2-propanol at 1:1 in volume. Carbon black (C) or NH-CP-coated carbon black (NH-CP/C) was used as the conducting agent. Then, 0.1 ml of 5 wt. % Nafion solution (Sigma-Aldrich 274704) was added to the mixture. Five microliters of the catalyst ink were dropped onto the glassy carbon disk electrode of the rotating ring-disk electrodes. The loading density of the total composite was fixed at 0.8 mg cm^{-2}.

Electrochemical characterization.

Cyclic voltammograms and linear sweep voltammograms (CVs and LSVs) were obtained on rotating ring disk electrodes (RRDEs) by a bipotentiostat (Iviumstat, Ivium Technologies). The ring-disk electrode of the glassy carbon disk and platinum ring was used as the working electrode (disk area = 0.1256 cm^2). A graphite rod and a Hg/HgO electrode were used as the counter electrode and reference electrode, respectively. A 0.1 M KOH aqueous solution was used as the electrolyte. The working electrode was rotated at 1600 rpm by the RRDE rotator (ALS RRDE-3A). ORR polarization curves were obtained from a cathodic sweep from +0.1 V to -0.7 V (vs. Hg/HgO) at 10 mV s^{-1} after five cycles. Oxygen was purged through the electrolytes for 30 min before the potential sweep and continuously bubbled during experiments. Nitrogen was used to purge to obtain the background current; +0.4 V versus Hg/HgO was applied to the ring electrode for peroxide detection. The measured potential (V versus Hg/HgO) was adjusted to the value versus reversible hydrogen electrode (RHE) by RHE =

Hg/HgO + 0.929 The potential difference between the RHE and Hg/HgO electrodes was estimated experimentally.

Physicochemical characterization.

X-ray photoelectron spectroscopy (ESCALAB 250XI, Thermo Fisher Scientific) was used to measure the oxidation state of cobalt. Fourier transform infrared spectroscopy (Alpha, Bruker) was used to prove the proton transfer from the polypyrrole to the adsorbates.

The number of electrons transferred from NH-CP to diatomic oxygen (δ).

The values of δ were calculated using the Dmol^3 program for DFT calculation.[133, 134] The generalized gradient approximation (GGA) with the Perdew-Burke-Ernzerhof (PBE) functional was used for the exchange-correlation energy.[66] The spin-polarized calculations were performed with the basis set of DNP 4.4. All electron relativistic core treatments were also employed with a smearing value of 0.005 Ha. The semi-empirical Tkatchenko-Scheffler (TS) scheme[135] was included for the dispersion correction. The Monkhorst-Pack grid was applied as the Γ point for all model systems.[70] The convergence criteria for the geometry optimization were set to 1.0×10^{-5} Ha for energy, 0.002 Ha/Å for force and 0.005 Å for displacement. The amount of charge transfer (δ) of the NH-CPs was obtained by a Mulliken population analysis.[136]

Mechanism.

The Vienna ab initio simulation package (VASP) was employed to carry out the spin-polarized density functional theory (DFT) calculations.[112, 113] The electronic exchange correlation potential was treated by a generalized gradient approximation with the Perdew-Burke-Ernzerhof functional (GGA-PBE). The electron-ion interaction was described by the projector augmented-wave (PAW)[114] method. The energy cutoff for the plane-wave basis set was set to 550 eV. The Hubbard U (*i.e.*, $U_{\text{eff}} = 5.0$ eV) correction[137, 138] was employed for the Co 3*d* electrons. The van der Waals interactions were corrected with Grimme's D2 method[115]. The self-consistent field (SCF) calculations were performed with the convergence criterion of 1×10^{-6} eV. The atomic positions and lattice parameters were fully relaxed until the Hellmann-Feynman forces acting on the ions were less than 0.01 eV/Å. The Brillouin zone was integrated using $3 \times 3 \times 3$ k-point meshes and the Γ point with the Monkhorst-Pack scheme for bulk and surface systems, respectively. To investigate the atomic charges, the Bader charge analysis[116-118] was implemented.

Model systems.

The antiferromagnetic arrangement of the moments in CoO was used to calculate the mechanism of the

ORR.[139] The formal spin (s = +3 / -3) was initially applied to the CoO bulk/surface state before the structure relaxation. The optimized lattice parameters of the bulk CoO were determined as $a = b = c$ = 8.563 Å, $\alpha = \beta = 90°$, and $\gamma = 90°$ (**Figure 52a**). Using the optimized unit cell, a symmetric slab model of the (001) surface consisting of 4 atomic layers was constructed with a vacuum slab of 20 Å (**Figure 52b**). Note that one atomic layer at the bottom was constrained during the optimization to consider the bulk-like effect. To verify the pPy-assisted mechanism of ORR on the CoO surface and the role of pPy on the adsorption of O_2, a model system consisting of pPy/pPy-H and CoO was constructed (**Figure 53**). Then, the intermediates of the ORR (*i.e.,* *O_2, *OOH, *O, and *OH) were adsorbed onto the 5-coordinated Co ion near NH/N of pPy/pPy-H.

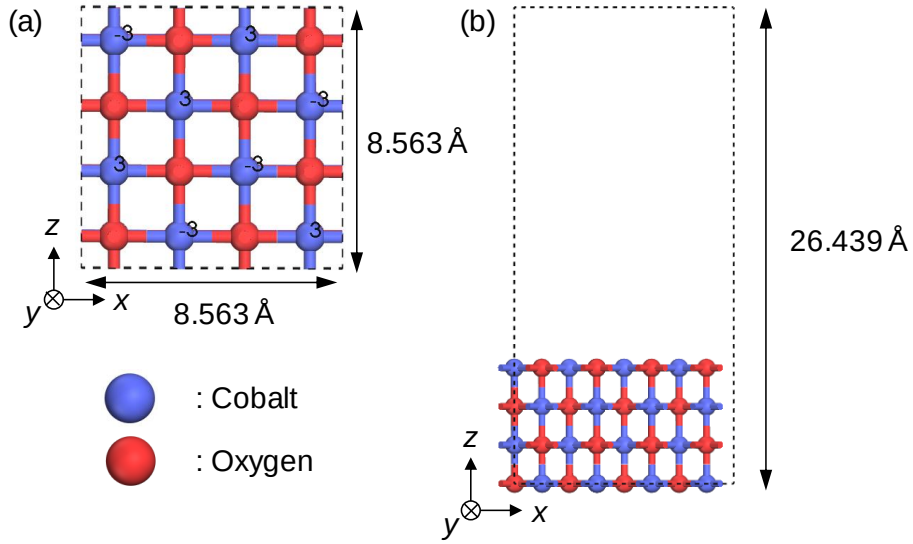

Figure 52. (a) Unit cell structure and **(b)** (001) surface of CoO. The labels of atomic colors are presented in the figure. The applied formal spins are numbered on cobalt atoms. Lattice and periodic boundary are represented by dashed line.

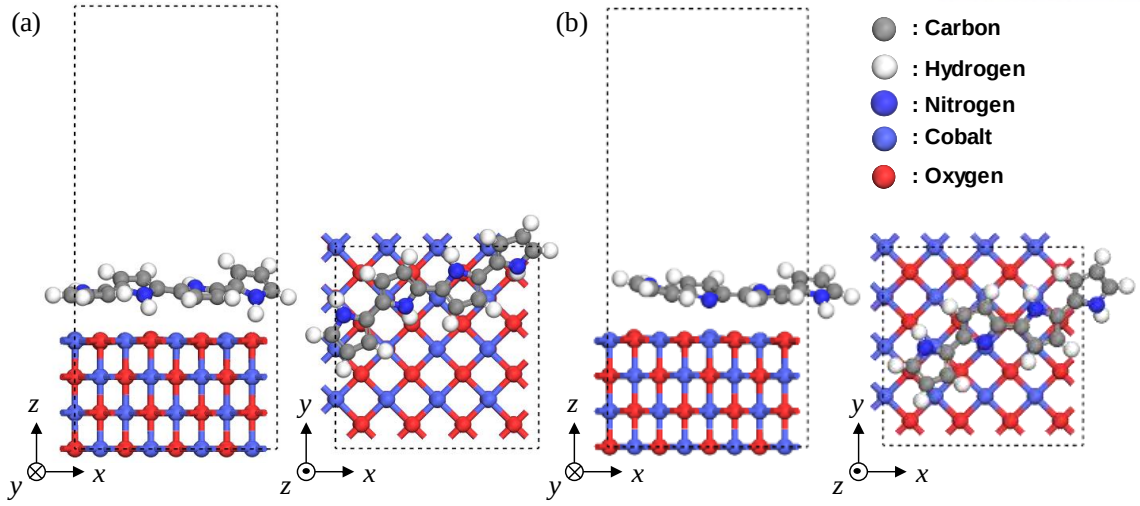

Figure 53. Model systems for **(a)** CoO+O_2+pPy and **(b)** CoO+O_2+ pPy-H . The labels of atomic colors are represented in the figure.

Derivation of apparent transfer coefficient (α).

The NH-CP-assisted ORR associative mechanism follows:

(1) $O_2 + H^+/e^- + * \rightarrow OOH*$

(2) $OOH* + H^+/e^- \rightarrow O* + H_2O$

(3) $O* + NH\text{-}CP \rightarrow OH* + N^+\text{-}CP$

(4) $OH* + H^+/e^- \rightarrow H_2O + *$

(5) $N^+\text{-}CP + H^+/e^- \rightarrow NH\text{-}CP$

Quasi-equilibrium of steps 1,2,4,5 yields:

$$K_1 = \frac{\theta_{OOH}}{P_{O_2}[H^+]\theta_*} \ , \ K_2 = \frac{\theta_O}{\theta_{OOH}[H^+]} \ , \ K_4 = \frac{\theta_*}{\theta_{OH}[H^+]} \ , \ K_5 = \frac{[OA{-}H]}{[OA][H^+]}$$

Each coverage of OH, O and OOH are:

$$\theta_{OOH} = K_1 P_{O_2}[H^+]\theta_* \ , \ \theta_O = K_1 K_2 P_{O_2}[H^+]^2\theta_* \ , \ \theta_{OH} = \frac{1}{K_4[H^+]}\theta_*$$

Set sum of all coverages is $\theta_* + \theta_{OH} + \theta_O + \theta_{OOH} = 1$,

then the coverage of free site as below:

$$\theta_* = \left[1 + \frac{\theta_{OH}}{\theta_*} + \frac{\theta_O}{\theta_*} + \frac{\theta_{OOH}}{\theta_*}\right]^{-1} = \left[1 + K_1 P_{O_2}[H^+] + K_1 K_2 P_{O_2}[H^+]^2\theta_* + \frac{1}{K_4[H^+]}\right]^{-1}$$

If RDS is step 3, ORR current is described by:

$$i_c = r_3 = k_3[OA - H]\theta_{O*} - k_{-3}[OA]\theta_{OH*} = k_3 K_1 K_2 P_{O_2}[H^+]^2\theta_* \left(1 - \frac{1}{K_3 K_4 K_5 [H^+]^3}\right)$$

If overpotential is enough, $\frac{1}{K_3 K_4 K_5 [H^+]^3} = 0$.

$$i_c = k_3 K_1 K_2 P_{O_2} [H^+]^2 \theta_*$$

$$\alpha = -\frac{RT}{F}\frac{\partial \ln|i|}{\partial E} = -\frac{RT}{F}\frac{\partial}{\partial E}\left[\ln k_3 + \ln K_1 + \ln K_2 + \ln P_{O_2} + \ln[H^+]^2 + \ln \theta_*\right]$$

$$\alpha = 0 + 1 + 1 + 0 + 0 + \frac{RT}{F}\theta_* \frac{\partial}{\partial E}[\theta_*^{-1}]$$

$$\alpha = 2 + \frac{RT}{F}\theta_* \left[\frac{-F}{RT} K_1 P_{O_2} [H^+]\theta_* + \frac{-2F}{RT} K_1 K_2 P_{O_2} [H^+]^2 \theta_* + \frac{F}{RT}\frac{1}{K_4 [H^+]}\right]$$

$$\alpha = 2 + \frac{RT}{F}\theta_* \left[\frac{-F}{RT}\frac{\theta_{OOH}}{\theta_*} + \frac{-2F}{RT}\frac{\theta_O}{\theta_*} + \frac{F}{RT}\frac{\theta_{OH}}{\theta_*}\right] = 2 + \theta_{OH} - 2\theta_O - \theta_{OOH}$$

Energy calculation.

The binding energy (ΔE^{bind}) of O_2 or $O_2^{\delta-}$ to a catalyst surface (e.g., CoO) was calculated by:

$$\Delta E^{\text{bind}}(\text{O}_2 - \text{catalyst}) = E_{(\text{O}_2+\text{catalyst})} - E_{\text{catalyst}} - E_{\text{O}_2}$$

$$\Delta E^{\text{bind}}\left(\text{O}_2^{\delta-} - \text{catalyst}\right) = E_{(\text{O}_2+\text{catalyst+pPy})} - E_{\text{catalyst+pPy}} - E_{\text{O}_2}$$

where E_{system} = the total energy of the system indicated by the subscript. The energies of the first, intermediate and final species participating in ORR were calculated based on the following mechanism:

$* + O_2 \rightarrow *O_2$

$*O_2 + H^+ + e^- \rightarrow *OOH$

$*OOH + H^+ + e^- \rightarrow *O + H_2O$

$*O + H^+ + e^- \rightarrow *OH$

$*OH + H^+ + e^- \rightarrow * + H_2O$

where * = the reaction site of the catalyst (*i.e.*, Co of the (001) surface of CoO). The proton transfer energy ($\Delta E^{\text{proton-transfer}}$) from pPy to adsorbate was calculated by:

$$\Delta E^{\text{proton-transfer}} = E_{*\text{AH@(pPy-H)}} - E_{*\text{A@(pPy)}} \ (\text{A} = \text{O}_2, \text{OOH}, \text{O}, \text{OH})$$

where *A@pPy and *AH@pPy-H are the certain oxygen species (A) with pPy and protonated oxygen species (AH) with deprotonated pPy (pPy-H), respectively. Note that when H_2O is a resulting product for the proton transfer reaction, we add the total energy of H_2O on above equation (*i.e.*, when A is OOH or OH). The result is shown in **Figure 41c**, and on the basis of this result, we predict that the proton transfer occurs at *O@(pPy).

To determine the step of ORR, at which the regeneration (or proton transfer) of deprotonated pPy achieves the highest ORR efficiency, we calculated all cases of the regeneration of deprotonated pPy with each intermediate state of ORR (*i.e.*, *, $*O_2$, *OOH, *O, *OH). The regeneration of deprotonated pPy was predicted to occur at * with deprotonated pPy (*i.e.*, *@(pPy-H)), right after the formation of two H_2O molecules through the ORR. With this result, we designed the following reaction path with the consideration of the proton transfer,

*@(pPy) + O_2 → *O_2@(pPy)

*O_2@(pPy) + $H^+ + e^-$ → *OOH@(pPy)

*OOH@(pPy) + $H^+ + e^-$ → *O@(pPy) + H_2O

*O@(pPy) → *OH@(pPy-H)

*OH@(pPy-H) + $H^+ + e^-$ → *@(pPy-H) + H_2O

*@(pPy-H) + $H^+ + e^-$ → *@(pPy)

Note that the equilibrium potential (U^{eq}) for DFT calculation was calculated with following equation,

$$U^{eq} = \frac{E_{O_2} + 2E_{H_2} - 2E_{H_2O}}{4}$$

4.5. Conclusion

In this work, dual catalysis was used as a strategy to improve the ORR activity of electrocatalysts. A series of secondary-amine-conjugated polymers (HN-CPs) was used as the third party material to polarize the reactant of the ORR to be $O_2^{\delta-}$. The activated diatomic oxygen species ($O_2^{\delta-}$) was transferred to the active site of cobalt-based electrocatalysts (CoO, $LiCoO_2$ and Co_3O_4 in this work). While the ORR proceeded along the mechanistic pathway following *OO → *OOH → *O → *OH → *OO (the surface intermediates on catalyst), the proton of the HN-CP was transformed to a single oxygen surface species (*O). The kinetic gains were obtained in the surface single oxygen formation step (*OOH to *O) at the equilibrium potential and the proton transfer step (*O to *OH) at a biased potential by dual catalysis when compared with conventional electrocatalysis in the absence of an NH-CP (RDS = the surface peroxide formation step of *OO to *OOH).

The number of electrons transferred from the NH-CP to the oxygen molecule (δ in $O_2^{\delta-}$) was the descriptor used to characterize the NH-CP and determined the ORR activity improvement. Higher-δ NH-CPs showed better ORR activity: pPy > pAni > pInd. This monotonically proportional δ-dependency of the catalytic activity was believed to be on the uphill side (left part) of the additional catalyst-described version of the volcano plot (the ORR activity measure versus the NH-CP descriptor, δ). The positively proportional δ dependency would be correct only when the activated oxygen species was more beneficial to binding to the active site of the catalyst than the neutral oxygen molecule. On the other hand, the downhill δ dependency of the catalytic activity was expected on the right wing of the volcano in the high-δ region because binding of an oxygen molecule to NH-CP that is too strong discourages the activated oxygen species from being transferred to the active site of the electrocatalyst. To complete the whole shape of the volcano, we look for an NH-CP having a value of δ higher than that of pPy. We believe that the dual electrocatalysis achieved by simply mixing catalyst particles with the NH-CPs is the most efficient and easiest way to improve the electrocatalytic activities of cost-efficient catalysts to the level of precious metal electrocatalysts. We have already confirmed that our strategy of dual electrocatalysis worked for oxygen reduction by catalysts based on other transition metals, such as Ni, Zn, Cu and Fe, in addition to Co shown in this work (not shown here but for future publication).

Publications

Total SCI journal publication: 3

1st author: 2, Co-author: 1

1. Dilimon, V. S.; **Lee, D. G.**; Yim, S. D.; Song, H. K.*
   "Multiple Roles of Superoxide on Oxygen Reduction Reaction in Li+-Containing Nonaqueous Electrolyte: Contribution to the Formation of Oxide as Well as Peroxide"
   J. Phys. Chem. C **2015**, *119*, 3472

2. **Lee, D.-G**.; Gwon, O.; Park, H.-S.; Kim, S. H.; Yang, J.; Kwak, S. K.; Kim, G.; Song, H.-K.*
   "Conductivity-Dependent Completion of Oxygen Reduction on Oxide Catalysts"
   Angew. Chem. Int. Ed. **2015**, *54*, 15730

3. **Lee, D.-G.**; Kim, S. H.; Joo, S. H.; Ji, H. I.; Tavassol, H.; Jeon, Y.; Choi, S.; Lee, M. H.; Kim, C.; Kwak, S. K.; Kim, G.; Song, H.-K.*
   "Polypyrrole-assisted oxygen electrocatalysis on perovskite oxides"
   Energy Environ. Sci. **2017**, *10*, 523.

References

(1) Yeager, E. Dioxygen Electrocatalysis - Mechanisms in Relation to Catalyst Structure *J. Mol. Catal.* **1986**, *38*, 5.

(2) Tan, P.; Chen, B.; Xu, H. R.; Zhang, H. C.; Cai, W. Z.; Ni, M.; Liu, M. L.; Shao, Z. P. Flexible Zn- and Li-air batteries: recent advances, challenges, and future perspectives *Energy Environ. Sci.* **2017**, *10*, 2056.

(3) Lu, Z. Y.; Chen, G. X.; Siahrostami, S.; Chen, Z. H.; Liu, K.; Xie, J.; Liao, L.; Wu, T.; Lin, D. C.; Liu, Y. Y.; Jaramillo, T. F.; Norskov, J. K.; Cui, Y. High-efficiency oxygen reduction to hydrogen peroxide catalysed by oxidized carbon materials *Nature Catalysis* **2018**, *1*, 156.

(4) Gong, K. P.; Du, F.; Xia, Z. H.; Durstock, M.; Dai, L. M. Nitrogen-Doped Carbon Nanotube Arrays with High Electrocatalytic Activity for Oxygen Reduction *Science* **2009**, *323*, 760.

(5) Guo, D. H.; Shibuya, R.; Akiba, C.; Saji, S.; Kondo, T.; Nakamura, J. Active sites of nitrogen-doped carbon materials for oxygen reduction reaction clarified using model catalysts *Science* **2016**, *351*, 361.

(6) Norskov, J. K.; Rossmeisl, J.; Logadottir, A.; Lindqvist, L.; Kitchin, J. R.; Bligaard, T.; Jonsson, H. Origin of the overpotential for oxygen reduction at a fuel-cell cathode *J. Phys. Chem. B* **2004**, *108*, 17886.

(7) Pérez-Ramírez, J.; López, N.; Strategies to break linear scaling relationships *Nature Catalysis* **2019**, *2*, 971.

(8) Allen, A. E.; MacMillan, D. W. C. Synergistic catalysis: A powerful synthetic strategy for new reaction development *Chem Sci* **2012**, *3*, 633.

(9) Skubi, K. L.; Blum, T. R.; Yoon, T. P. Dual Catalysis Strategies in Photochemical Synthesis *Chem. Rev.* **2016**, *116*, 10035.

(10) Lichosyt, D.; Zhang, Y.; Hurej, K.; Dydio, P. Dual-catalytic transition metal systems for functionalization of unreactive sites of molecules *Nature Catalysis* **2019**, *2*, 114.

(11) Shi, Y. L.; Peterson, S. M.; Haberaecker, W. W.; Blum, S. A. Alkynes as Stille reaction pseudohalides: Gold- and palladium-cocatalyzed synthesis of tri- and tetra-substituted olefins *J. Am. Chem. Soc.* **2008**, *130*, 2168.

(12) Lim, B.; Jiang, M. J.; Camargo, P. H. C.; Cho, E. C.; Tao, J.; Lu, X. M.; Zhu, Y. M.; Xia, Y. N. Pd-Pt Bimetallic Nanodendrites with High Activity for Oxygen Reduction *Science* **2009**, *324*, 1302.

(13) Greeley, J.; Stephens, I. E. L.; Bondarenko, A. S.; Johansson, T. P.; Hansen, H. A.; Jaramillo, T. F.; Rossmeisl, J.; Chorkendorff, I.; Norskov, J. K. Alloys of platinum and early transition metals as oxygen reduction electrocatalysts *Nat. Chem.* **2009**, *1*, 552.

(14) Bradley, K.; Giagloglou, K.; Hayden, B. E.; Jungius, H.; Vian, C. Reversible perovskite electrocatalysts for oxygen reduction/oxygen evolution *Chem Sci* **2019**, *10*, 4609.

(15) Doyle, A. D.; Montoya, J. H.; Vojvodic, A. Improving Oxygen Electrochemistry through Nanoscopic Confinement *Chemcatchem* **2015**, *7*, 738.

(16) Shen, X. C.; Nagai, T.; Yang, F. P.; Zhou, L. Q.; Pan, Y. B.; Yao, L. B.; Wu, D. Z.; Liu, Y. S.; Feng, J.; Guo, J. H.; Jia, H. F.; Peng, Z. M. Dual-Site Cascade Oxygen Reduction Mechanism on SnOx/Pt-Cu-Ni for Promoting Reaction Kinetics *J. Am. Chem. Soc.* **2019**, *141*, 9463.

(17) Cao, L.; Scheiba, F.; Roth, C.; Schweiger, F.; Cremers, C.; Stimming, U.; Fuess, H.; Chen, L. Q.; Zhu, W. T.; Qiu, X. P. Novel nanocomposite Pt/RuO_2 . xH_2O/carbon nanotube catalysts for direct methanol fuel cells *Angew. Chem. Int. Ed.* **2006**, *45*, 5315.

(18) Ermete, A. Carbon supports for low-temperature fuel cell catalysts *Appl. Catal. B-Environ.* **2009**, *88*, 1.

(19) Kou, R.; Shao, Y. Y.; Wang, D. H.; Engelhard, M. H.; Kwak, J. H.; Wang, J.; Viswanathan, V. V.; Wang, C. M.; Lin, Y. H.; Wang, Y.; Aksay, I. A.; Liu, J. Enhanced activity and stability of Pt catalysts on functionalized graphene sheets for electrocatalytic oxygen reduction *Electrochem. Commun.* **2009**, *11*, 954.

(20) Guo, S. J.; Dong, S. J.; Wang, E. K. Three-Dimensional Pt-on-Pd Bimetallic Nanodendrites Supported on Graphene Nanosheet: Facile Synthesis and Used as an Advanced Nanoelectrocatalyst for Methanol Oxidation *ACS Nano* **2010**, *4*, 547.

(21) Liang, Y. Y.; Li, Y. G.; Wang, H. L.; Zhou, J. G.; Wang, J.; Regier, T.; Dai, H. J. Co3O4 nanocrystals on graphene as a synergistic catalyst for oxygen reduction reaction *Nat. Mater.* **2011**, *10*, 780.

(22) Rao, C. V.; Reddy, A. L. M.; Ishikawa, Y.; Ajayan, P. M. Synthesis and electrocatalytic oxygen reduction activity of graphene-supported Pt3Co and Pt3Cr alloy nanoparticles *Carbon* **2011**, *49*, 931.

(23) Li, Y. J.; Li, Y. J.; Zhu, E. B.; McLouth, T.; Chiu, C. Y.; Huang, X. Q.; Huang, Y. Stabilization of High-Performance Oxygen Reduction Reaction Pt Electrocatalyst Supported on Reduced Graphene Oxide/Carbon Black Composite *J. Am. Chem. Soc.* **2012**, *134*, 12326.

(24) Bi, E. B.; Chen, H.; Yang, X. D.; Peng, W. Q.; Gratzel, M.; Han, L. Y. A quasi core-shell nitrogen-doped graphene/cobalt sulfide conductive catalyst for highly efficient dye-sensitized solar cells *Energy Environ. Sci.* **2014**, *7*, 2637.

(25) Flandrois, S.; Simon, B. Carbon materials for lithium-ion reachargeable battries *Carbon* **1999**, *37*, 165.

(26) Mennola, T.; Mikkola, M.; Noponen, M.; Hottinen, T.; Lund, P. Measurement of ohmic voltage losses in individual cells of a PEMFC stack *J. Power Sources* **2002**, *112*, 261.

(27) Zhang, W. M.; Wu, X. L.; Hu, J. S.; Guo, Y. G.; Wan, L. J. Carbon Coated Fe3O4 Nanospindles as a Superior Anode Material for Lithium-Ion Batteries *Adv. Funct. Mater.* **2008**, *18*, 3941.

(28) Cui, L. F.; Yang, Y.; Hsu, C. M.; Cui, Y. Carbon-Silicon Core-Shell Nanowires as High Capacity Electrode for Lithium Ion Batteries *Nano Lett.* **2009**, *9*, 3370.

(29) Breysse, M.; Veron, J.; Claudel, B.; Latreill.H; Guenin, M. Catalysis of Carbon-Monoxide Oxidation by Cerium Dioxide .1. Correlations between Catalytic Activity and Electrical Conductivity *J. Catal.* **1972**, *27*, 275.

(30) Stoerzinger, K. A.; Lü, W.; Li, C.; Ariando; Venkatesan, T.; Shao-Horn, Y. Highly Active Epitaxial $La_{(1-x)}Sr_xMnO_3$ Surfaces for the Oxygen Reduction Reaction: Role of Charge Transfer *J. Phys. Chem.*

Lett. **2015**, *6*, 1435.

(31) Passalacqua, E.; Lufrano, F.; Squadrito, G.; Patti, A.; Giorgi, L. Nafion content in the catalyst layer of polymer electrolyte fuel cells: effects on structure and performance *Electrochim. Acta* **2001**, *46*, 799.

(32) van der Vliet, D.; Strmcnik, D. S.; Wang, C.; Stamenkovic, V. R.; Markovic, N. M.; Koper, M. T. M. On the importance of correcting for the uncompensated Ohmic resistance in model experiments of the Oxygen Reduction Reaction *J. Electroanal. Chem.* **2010**, *647*, 29.

(33) Fabbri, E.; Mohamed, R.; Levecque, P.; Conrad, O.; Kötz, R.; Schmidt, T. J. Composite Electrode Boosts the Activity of $Ba_{0.5}Sr_{0.5}Co_{0.8}Fe_{0.2}O_{3-\delta}$ Perovskite and Carbon toward Oxygen Reduction in Alkaline Media *Acs Catal* **2014**, *4*, 1061.

(34) Goodenough, J. B.; Cushing, B. L. In *Handbook of Fuel Cells*; Vielstich, W.,Gasteiger, H. A.,Yokokawa, H., Eds.; John Wiley & Sons: 2010.

(35) Markovic, N. M.; Schmidt, T. J.; Stamenkovic, V.; Ross, P. N. Oxygen Reduction Reaction on Pt and Pt Bimetallic Surfaces: A Selective Review *Fuel Cells* **2001**, *1*, 105.

(36) Markovic, N. M.; Ross, P. N. Surface science studies of model fuel cell electrocatalysts *Surf. Sci. Rep.* **2002**, *45*, 121.

(37) Markovic, N. M.; Gasteiger, H. A.; Philip, N. Oxygen reduction on platinum low-index single-crystal surfaces in alkaline solution: Rotating ring disk(Pt(hkl)) studies *J. Phys. Chem.* **1996**, *100*, 6715.

(38) Komanicky, V.; Iddir, H.; Chang, K. C.; Menzel, A.; Karapetrov, G.; Hennessy, D.; Zapol, P.; You, H. Shape-Dependent Activity of Platinum Array Catalyst *J. Am. Chem. Soc.* **2009**, *131*, 5732.

(39) El-Deab, M. S.; Ohsaka, T. Manganese oxide nanoparticles electrodeposited on platinum are superior to platinum for oxygen reduction *Angew. Chem. Int. Ed.* **2006**, *45*, 5963.

(40) Suntivich, J.; May, K. J.; Gasteiger, H. A.; Goodenough, J. B.; Shao-Horn, Y. A Perovskite Oxide Optimized for Oxygen Evolution Catalysis from Molecular Orbital Principles *Science* **2011**, *334*, 1383.

(41) Suntivich, J.; Gasteiger, H. A.; Yabuuchi, N.; Nakanishi, H.; Goodenough, J. B.; Shao-Horn, Y. Design principles for oxygen-reduction activity on perovskite oxide catalysts for fuel cells and metal–air batteries *Nat. Chem.* **2011**, *3*, 546.

(42) Park, S.; Choi, S.; Kim, J.; Shin, J.; Kim, G. Strontium Doping Effect on High-Performance $PrBa_{1-x}SrxCo_2O_{5+\delta}$ as a Cathode Material for IT-SOFCs *ECS Electrochem. Lett.* **2012**, *1*, F29.

(43) Yoo, S.; Choi, S.; Kim, J.; Shin, J.; Kim, G. Investigation of layered perovskite type $NdBa_{1-x}Sr_xCo_2O_{5+\delta}$ (x = 0, 0.25, 0.5, 0.75, and 1.0) cathodes for intermediate-temperature solid oxide fuel cells *Electrochim. Acta* **2013**, *100*, 44.

(44) Risch, M.; Stoerzinger, K. A.; Maruyama, S.; Hong, W. T.; Takeuchi, I.; Shao-Horn, Y. La0.8Sr0.2MnO3-delta Decorated with $Ba_{0.5}Sr_{0.5}Co_{0.3}Fe_{0.2}O_{3-\delta}$: A Bifunctional Surface for Oxygen Electrocatalysis with Enhanced Stability and Activity *J. Am. Chem. Soc.* **2014**, *136*, 5229.

(45) Takeguchi, T.; Yamanaka, T.; Takahashi, H.; Watanabe, H.; Kuroki, T.; Nakanishi, H.; Orikasa, Y.; Uchimoto, Y.; Takano, H.; Ohguri, N.; Matsuda, M.; Murota, T.; Uosaki, K.; Ueda, W. Layered Perovskite Oxide: A Reversible Air Electrode for Oxygen Evolution/Reduction in Rechargeable Metal-Air

Batteries *J. Am. Chem. Soc.* **2013**, *135*, 11125.

(46) Xu, J.-J.; Xu, D.; Wang, Z.-L.; Wang, H.-G.; Zhang, L.-L.; Zhang, X.-B. Synthesis of Perovskite-Based Porous $La_{0.75}Sr_{0.25}MnO_3$ Nanotubes as a Highly Efficient Electrocatalyst for Rechargeable Lithium–Oxygen Batteries *Angew. Chem. Int. Ed.* **2013**, *52*, 3887.

(47) Zhao, Y. L.; Xu, L.; Mai, L. Q.; Han, C. H.; An, Q. Y.; Xu, X.; Liu, X.; Zhang, Q. J. Hierarchical mesoporous perovskite $La_{0.5}Sr_{0.5}CoO_{2.91}$ nanowires with ultrahigh capacity for Li-air batteries *Proc. Natl. Acad. Sci. U. S. A.* **2012**, *109*, 19569.

(48) Jung, J.-I.; Jeong, H. Y.; Lee, J.-S.; Kim, M. G.; Cho, J. A Bifunctional Perovskite Catalyst for Oxygen Reduction and Evolution *Angew. Chem. Int. Ed.* **2014**, *53*, 4582.

(49) Grimaud, A.; May, K. J.; Carlton, C. E.; Lee, Y.-L.; Risch, M.; Hong, W. T.; Zhou, J.; Shao-Horn, Y. Double perovskites as a family of highly active catalysts for oxygen evolution in alkaline solution *Nat. Commun.* **2013**, *4*, 2439.

(50) Kim, J.; Yin, X.; Tsao, K. C.; Fang, S. H.; Yang, H. Ca2Mn2O5 as Oxygen-Deficient Perovskite Electrocatalyst for Oxygen Evolution Reaction *J. Am. Chem. Soc.* **2014**, *136*, 14646.

(51) Zhu, Y. L.; Zhou, W.; Chen, Z. G.; Chen, Y. B.; Su, C.; Tade, M. O.; Shao, Z. P. $SrNb_{0.1}Co_{0.7}Fe_{0.2}O_{3-\delta}$ Perovskite as a Next-Generation Electrocatalyst for Oxygen Evolution in Alkaline Solution *Angew. Chem. Int. Ed.* **2015**, *54*, 3897.

(52) Zhou, W.; Sunarso, J. Enhancing Bi-functional Electrocatalytic Activity of Perovskite by Temperature Shock: A Case Study of $LaNiO_{3-\delta}$ *J. Phys. Chem. Lett.* **2013**, *4*, 2982.

(53) Zhu, Y.; Su, C.; Xu, X.; Zhou, W.; Ran, R.; Shao, Z. A Universal and Facile Way for the Development of Superior Bifunctional Electrocatalysts for Oxygen Reduction and Evolution Reactions Utilizing the Synergistic Effect *Chem. Eur. J.* **2014**, *20*, 15533.

(54) Liu, R.; Liang, F.; Zhou, W.; Yang, Y.; Zhu, Z. Calcium-doped lanthanum nickelate layered perovskite and nickel oxide nano-hybrid for highly efficient water oxidation *Nano Energy* **2015**, *12*, 115.

(55) Zhu, Y.; Zhou, W.; Chen, Y.; Yu, J.; Xu, X.; Su, C.; Tadé, M. O.; Shao, Z. Boosting Oxygen Reduction Reaction Activity of Palladium by Stabilizing Its Unusual Oxidation States in Perovskite *Chem. Mater.* **2015**, *27*, 3048.

(56) Zhou, W.; Zhao, M.; Liang, F.; Smith, S. C.; Zhu, Z. High activity and durability of novel perovskite electrocatalysts for water oxidation *Mater. Horiz.* **2015**, *2*, 495.

(57) Blase, X.; Bustarret, E.; Chapelier, C.; Klein, T.; Marcenat, C. Superconducting group-IV semiconductors *Nat. Mater.* **2009**, *8*, 375.

(58) Park, S. M.; Ho, S.; Aruliah, S.; Weber, M. F.; Ward, C. A.; Venter, R. D.; Srinivasan, S. Electrochemical Reduction of Oxygen at Platinum Electrodes in KOH Solutions - Temperature and Concentration Effects *J. Electrochem. Soc.* **1986**, *133*, 1641.

(59) Parthasarathy, A.; Srinivasan, S.; Appleby, A. J.; Martin, C. R. Pressure-Dependence of the Oxygen Reduction Reaction at the Platinum Microelectrode Nafion Interface - Electrode-Kinetics and Mass-Transport *J. Electrochem. Soc.* **1992**, *139*, 2856.

(60) Paulus, U. A.; Schmidt, T. J.; Gasteiger, H. A.; Behm, R. J. Oxygen reduction on a high-surface area Pt/Vulcan carbon catalyst: a thin-film rotating ring-disk electrode study *J. Electroanal. Chem.* **2001**, *495*, 134.

(61) Zhang, L.; Lee, K.; Zhang, J. J. The effect of heat treatment on nanoparticle size and ORR activity for carbon-supported Pd-Co alloy electrocatalysts *Electrochim. Acta* **2007**, *52*, 3088.

(62) Voinovic, V. M.; Sepa, B. D. Reaction intermediates as a controlling factor in the kinetics and mechanism of oxygen reduction at platinum electrodes *Electrochim. Acta 26*, 781.

(63) Song, C.; Zhang, J. In *PEM Fuel Cell Electrocatalysts and Catalyst Layers*; Zhang, J., Ed.; Springer: London, 2008; pp 89-134.

(64) Mercier, J. P.; Zambelli, G.; Kurz, W., *Introduction to Materials Science*. ed.; Elsevier: Oxford, 2002; 'Vol.' p.

(65) Segall, M. D.; Philip, J. D. L.; Probert, M. J.; Pickard, C. J.; Hasnip, P. J.; Clark, S. J.; Payne, M. C. First-principles simulation: ideas, illustrations and the CASTEP code *J. Phys.: Condens. Matter* **2002**, *14*, 2717.

(66) Perdew, J. P.; Burke, K.; Ernzerhof, M. Generalized gradient approximation made simple *Phys. Rev. Lett.* **1996**, *77*, 3865.

(67) Perdew, J. P.; Zunger, A. Self-interaction correction to density-functional approximations for many-electron systems *Phys. Rev. B* **1981**, *23*, 5048.

(68) Seidl, A.; Görling, A.; Vogl, P.; Majewski, J. A.; Levy, M. Generalized Kohn-Sham schemes and the band-gap problem *Phys. Rev. B* **1996**, *53*, 3764.

(69) Broyden, C. G. The Convergence of a Class of Double-Rank Minimization Algorithms *J. Inst. Math. Appl.* **1970**, *6*, 76.

(70) Monkhorst, H. J.; Pack, J. D. Special Points for Brillouin-Zone Integrations *Phys. Rev. B* **1976**, *13*, 5188.

(71) Steele, B. C. H.; Heinzel, A. Materials for fuel-cell technologies *Nature* **2001**, *414*, 345.

(72) Black, R.; Adams, B.; Nazar, L. F. Non-Aqueous and Hybrid Li-O_2 Batteries *Adv. Energy Mater.* **2012**, *2*, 801.

(73) Bruce, P. G.; Freunberger, S. A.; Hardwick, L. J.; Tarascon, J. M. Li-O_2 and Li-S batteries with high energy storage *Nat. Mater.* **2012**, *11*, 19.

(74) Cheng, F. Y.; Chen, J. Metal-air batteries: from oxygen reduction electrochemistry to cathode catalysts *Chem. Soc. Rev.* **2012**, *41*, 2172.

(75) Lee, J. S.; Kim, S. T.; Cao, R.; Choi, N. S.; Liu, M.; Lee, K. T.; Cho, J. Metal-Air Batteries with High Energy Density: Li-Air versus Zn-Air *Adv. Energy Mater.* **2011**, *1*, 34.

(76) Walter, M. G.; Warren, E. L.; McKone, J. R.; Boettcher, S. W.; Mi, Q. X.; Santori, E. A.; Lewis, N. S. Solar Water Splitting Cells *Chem. Rev.* **2010**, *110*, 6446.

(77) Maeda, K.; Teramura, K.; Lu, D. L.; Takata, T.; Saito, N.; Inoue, Y.; Domen, K. Photocatalyst releasing hydrogen from water - Enhancing catalytic performance holds promise for hydrogen production by water splitting in sunlight. *Nature* **2006**, *440*, 295.

(78) Schultze, J. W.; Vetter, K. J. The influence of the tunnel probability on the anodic oxygen evolution and other redox reactions at oxide covered platinum electrodes *Electrochim. Acta* **1973**, *18*, 889.

(79) Damjanovic, A.; Dey, A.; Bockris, J. O. M. Kinetics of oxygen evolution and dissolution on platinum electrodes *Electrochim. Acta* **1966**, *11*, 791.

(80) Miles, M. H.; Klaus, E. A.; Gunn, B. P.; Locker, J. R.; Serafin, W. E.; Srinivasan, S. The oxygen evolution reaction on platinum, iridium, ruthenium and their alloys at 80°C in acid solutions *Electrochim. Acta* **1978**, *23*, 521.

(81) Lee, Y.; Suntivich, J.; May, K. J.; Perry, E. E.; Shao-Horn, Y. Synthesis and Activities of Rutile IrO_2 and RuO_2 Nanoparticles for Oxygen Evolution in Acid and Alkaline Solutions *J. Phys. Chem. Lett.* **2012**, *3*, 399.

(82) Antolini, E. Iridium As Catalyst and Cocatalyst for Oxygen Evolution/Reduction in Acidic Polymer Electrolyte Membrane Electrolyzers and Fuel Cells *Acs Catal* **2014**, *4*, 1426.

(83) Lee, D.-G.; Gwon, O.; Park, H.-S.; Kim, S. H.; Yang, J.; Kwak, S. K.; Kim, G.; Song, H.-K. Conductivity-Dependent Completion of Oxygen Reduction on Oxide Catalysts *Angew. Chem. Int. Ed.* **2015**, *54*, 15730.

(84) Zitolo, A.; Goellner, V.; Armel, V.; Sougrati, M. T.; Mineva, T.; Stievano, L.; Fonda, E.; Jaouen, F. Identification of catalytic sites for oxygen reduction in iron- and nitrogen-doped graphene materials *Nat. Mater.* **2015**, *14*, 937.

(85) Jasinski, R. A New Fuel Cell Cathode Catalyst *Nature* **1964**, *201*, 1212.

(86) Cao, R.; Thapa, R.; Kim, H.; Xu, X.; Gyu Kim, M.; Li, Q.; Park, N.; Liu, M.; Cho, J. Promotion of oxygen reduction by a bio-inspired tethered iron phthalocyanine carbon nanotube-based catalyst *Nat. Commun.* **2013**, *4*.

(87) Bashyam, R.; Zelenay, P. A class of non-precious metal composite catalysts for fuel cells *Nature* **2006**, *443*, 63.

(88) Gupta, S.; Tryk, D.; Bae, I.; Aldred, W.; Yeager, E. Heat-treated polyacrylonitrile-based catalysts for oxygen electroreduction *J. Appl. Electrochem.* **1989**, *19*, 19.

(89) Lefevre, M.; Proietti, E.; Jaouen, F.; Dodelet, J.-P. Iron-Based Catalysts with Improved Oxygen Reduction Activity in Polymer Electrolyte Fuel Cells *Science* **2009**, *324*, 71.

(90) Shui, J.-L.; Karan, N. K.; Balasubramanian, M.; Li, S.-Y.; Liu, D.-J. Fe/N/C Composite in Li–O_2 Battery: Studies of Catalytic Structure and Activity toward Oxygen Evolution Reaction *J. Am. Chem. Soc.* **2012**, *134*, 16654.

(91) Sha, H.-D.; Yuan, X.; Li, L.; Ma, Z.; Ma, Z.-F.; Zhang, L.; Zhang, J. Experimental identification of the active sites in pyrolyzed carbon-supported cobalt–polypyrrole–4-toluenesulfinic acid as electrocatalysts for oxygen reduction reaction *J. Power Sources* **2014**, *255*, 76.

(92) Ju, Y.-W.; Yoo, S.; Kim, C.; Kim, S.; Jeon, I.-Y.; Shin, J.; Baek, J.-B.; Kim, G. Fe@N-Graphene Nanoplatelet-Embedded Carbon Nanofibers as Efficient Electrocatalysts for Oxygen Reduction Reaction *Advanced Science* **2016**, *3*, 1500205.

(93) Qu, L.; Liu, Y.; Baek, J.-B.; Dai, L. Nitrogen-Doped Graphene as Efficient Metal-Free Electrocatalyst for Oxygen Reduction in Fuel Cells *ACS Nano* **2010**, *4*, 1321.

(94) Wu, Z. S.; Yang, S. B.; Sun, Y.; Parvez, K.; Feng, X. L.; Mullen, K. 3D Nitrogen-Doped Graphene Aerogel-Supported Fe_3O_4 Nanoparticles as Efficient Eletrocatalysts for the Oxygen Reduction Reaction *J. Am. Chem. Soc.* **2012**, *134*, 9082.

(95) Chen, Z.; Yu, A. P.; Ahmed, R.; Wang, H. J.; Li, H.; Chen, Z. W. Manganese dioxide nanotube and nitrogen-doped carbon nanotube based composite bifunctional catalyst for rechargeable zinc-air battery *Electrochim. Acta* **2012**, *69*, 295.

(96) Liang, Y. Y.; Wang, H. L.; Zhou, J. G.; Li, Y. G.; Wang, J.; Regier, T.; Dai, H. J. Covalent Hybrid of Spinel Manganese-Cobalt Oxide and Graphene as Advanced Oxygen Reduction Electrocatalysts *J. Am. Chem. Soc.* **2012**, *134*, 3517.

(97) Hardin, W. G.; Slanac, D. A.; Wang, X.; Dai, S.; Johnston, K. P.; Stevenson, K. J. Highly Active, Nonprecious Metal Perovskite Electrocatalysts for Bifunctional Metal-Air Battery Electrodes *J. Phys. Chem. Lett.* **2013**, *4*, 1254.

(98) Kim, C.; Gwon, O.; Jeon, I. Y.; Kim, Y.; Shin, J.; Ju, Y. W.; Baek, J. B.; Kim, G. Cloud-like graphene nanoplatelets on $Nd_{0.5}Sr_{0.5}CoO_3^{-\delta}$ nanorods as an efficient bifunctional electrocatalyst for hybrid Li-air batteries *J. Mater. Chem. A* **2016**, *4*, 2122.

(99) Bie, S. Y.; Zhu, Y. Q.; Su, J. M.; Jin, C.; Liu, S. H.; Yang, R. Z.; Wu, J. One-pot fabrication of yolk-shell structured $La_{0.9}Sr_{0.1}CoO_3$ perovskite microspheres with enhanced catalytic activities for oxygen reduction and evolution reactions *J. Mater. Chem. A* **2015**, *3*, 22448.

(100) Park, H. W.; Lee, D. U.; Park, M. G.; Ahmed, R.; Seo, M. H.; Nazar, L. F.; Chen, Z. W. Perovskite-Nitrogen-Doped Carbon Nanotube Composite as Bifunctional Catalysts for Rechargeable Lithium-Air Batteries *Chemsuschem* **2015**, *8*, 1058.

(101) Wang, Z. D.; You, Y.; Yuan, J.; Yin, Y. X.; Li, Y. T.; Xin, S.; Zhang, D. Nickel-Doped $La_{0.8}Sr_{0.2}Mn_{1-x}Ni_xO_3$ Nanoparticles Containing Abundant Oxygen Vacancies as an Optimized Bifunctional Catalyst for Oxygen Cathode in Rechargeable Lithium-Air Batteries *ACS Appl. Mater. Interfaces* **2016**, *8*, 6520.

(102) Jung, J. I.; Risch, M.; Park, S.; Kim, M. G.; Nam, G.; Jeong, H. Y.; Shao-Horn, Y.; Cho, J. Optimizing nanoparticle perovskite for bifunctional oxygen electrocatalysis *Energy Environ. Sci.* **2016**, *9*, 176.

(103) Han, X. P.; Cheng, F. Y.; Zhang, T. R.; Yang, J. G.; Hu, Y. X.; Chen, J. Hydrogenated Uniform Pt Clusters Supported on Porous $CaMnO_3$ as a Bifunctional Electrocatalyst for Enhanced Oxygen Reduction and Evolution *Adv. Mater.* **2014**, *26*, 2047.

(104) Phillips, G.; Suresh, R.; Waldman, J.; Kumar, J.; I-Chen, J.; Tripathy, S.; Huang, J. C. Dielectric properties of polypyrrole doped with tosylate anion in the far infrared and microwave *J. Appl. Phys.* **1991**, *69*, 899.

(105) Wang, Y.-J.; Wilkinson, D. P.; Zhang, J. Noncarbon Support Materials for Polymer Electrolyte Membrane Fuel Cell Electrocatalysts *Chem. Rev.* **2011**, *111*, 7625.

(106) Khomenko, V. G.; Barsukov, V. Z.; Katashinskii, A. S. The catalytic activity of conducting

polymers toward oxygen reduction *Electrochim. Acta* **2005**, *50*, 1675.

(107) Yuan, Y.; Zhou, S.; Zhuang, L. Polypyrrole/carbon black composite as a novel oxygen reduction catalyst for microbial fuel cells *J. Power Sources* **2010**, *195*, 3490.

(108) Lei, J. T.; Martin, C. R. Investigations of the Chemical Interactions between Molecular-Oxygen and Pristine (Undoped) Polypyrrole *Chem. Mater.* **1995**, *7*, 578.

(109) Little, S.; Ralph, S. F.; Too, C. O.; Wallace, G. G. Solvent dependence of electrochromic behaviour of polypyrrole: Rediscovering the effect of molecular oxygen *Synth. Met.* **2009**, *159*, 1950.

(110) Scott, J. C.; Pfluger, P.; Krounbi, M. T.; Street, G. B. Electron-Spin-Resonance Studies of Pyrrole Polymers - Evidence for Bipolarons *Phys. Rev. B* **1983**, *28*, 2140.

(111) Hakansson, E.; Lin, T.; Wang, H. X.; Kaynak, A. The effects of dye dopants on the conductivity and optical absorption properties of polypyrrole *Synth. Met.* **2006**, *156*, 1194.

(112) Kresse, G.; Furthmuller, J. Efficient iterative schemes for ab initio total-energy calculations using a plane-wave basis set *Phys. Rev. B* **1996**, *54*, 11169.

(113) Kresse, G.; Furthmuller, J. Efficiency of ab-initio total energy calculations for metals and semiconductors using a plane-wave basis set *Comput. Mater. Sci.* **1996**, *6*, 15.

(114) Kresse, G.; Joubert, D. From ultrasoft pseudopotentials to the projector augmented-wave method *Phys. Rev. B* **1999**, *59*, 1758.

(115) Grimme, S. Semiempirical GGA-type density functional constructed with a long-range dispersion correction *J. Comput. Chem.* **2006**, *27*, 1787.

(116) Tang, W.; Sanville, E.; Henkelman, G. A grid-based Bader analysis algorithm without lattice bias *J Phys. Condens Mat.* **2009**, *21*.

(117) Sanville, E.; Kenny, S. D.; Smith, R.; Henkelman, G. Improved grid-based algorithm for Bader charge allocation *J. Comput. Chem.* **2007**, *28*, 899.

(118) Henkelman, G.; Arnaldsson, A.; Jonsson, H. A fast and robust algorithm for Bader decomposition of charge density *Comput. Mater. Sci.* **2006**, *36*, 354.

(119) Turrens, J. F. Mitochondrial formation of reactive oxygen species *J Physiol. London* **2003**, *552*, 335.

(120) Li, X. Y.; Fang, P.; Mai, J. T.; Choi, E. T.; Wang, H.; Yang, X. F. Targeting mitochondrial reactive oxygen species as novel therapy for inflammatory diseases and cancers *J Hematol Oncol* **2013**, *6*.

(121) Lin, L.; Yang, Z. K.; Jiang, Y. F.; Xu, A. W. Nonprecious Bimetallic (Fe,Mo)-N/C Catalyst for Efficient Oxygen Reduction Reaction *Acs Catal* **2016**, *6*, 4449.

(122) Gorlin, Y.; Jaramillo, T. F. A Bifunctional Nonprecious Metal Catalyst for Oxygen Reduction and Water Oxidation *J. Am. Chem. Soc.* **2010**, *132*, 13612.

(123) Lee, D. G.; Kim, S. H.; Joo, S. H.; Ji, H. I.; Tavassol, H.; Jeon, Y.; Choi, S.; Lee, M. H.; Kim, C.; Kwak, S. K.; Kim, G.; Song, H. K. Polypyrrole-assisted oxygen electrocatalysis on perovskite oxides *Energy Environ. Sci.* **2017**, *10*, 523.

(124) Xie, Q. J.; Kuwabata, S.; Yoneyama, H. EQCM studies on polypyrrole in aqueous solutions *J. Electroanal. Chem.* **1997**, *420*, 219.

(125) Inganas, O.; Erlandsson, R.; Nylander, C.; Lundstrom, I. Proton Modification of Conducting Polypyrrole *J. Phys. Chem. Solids* **1984**, *45*, 427.

(126) Pei, Q.; Qian, R. Protonation and Deprotonation of Polypyrrole Chain in Aqueous-Solutions *Synth. Met.* **1991**, *45*, 35.

(127) Kang, E. T.; Li, Z. F.; Neoh, K. G.; Dong, Y. Q.; Tan, K. L. Protonation and deprotonation of polyaniline films and powders: effects of acid and base concentrations on the surface intrinsic oxidation states *Synth. Met.* **1998**, *92*, 167.

(128) Busch, M.; Halck, N. B.; Kramm, U. I.; Siahrostami, S.; Krtil, P.; Rossmeisl, J. Beyond the top of the volcano? - A unified approach to electrocatalytic oxygen reduction and oxygen evolution *Nano Energy* **2016**, *29*, 126.

(129) Antoine, O.; Bultel, Y.; Durand, R. Oxygen reduction reaction kinetics and mechanism on platinum nanoparticles inside Nafion(R) *J. Electroanal. Chem.* **2001**, *499*, 85.

(130) Holewinski, A.; Linic, S. Elementary Mechanisms in Electrocatalysis: Revisiting the ORR Tafel Slope *J. Electrochem. Soc.* **2012**, *159*, H864.

(131) Viswanathan, V.; Hansen, H. A.; Rossmeisl, J.; Norskov, J. K. Unifying the 2e(-) and 4e(-) Reduction of Oxygen on Metal Surfaces *J. Phys. Chem. Lett.* **2012**, *3*, 2948.

(132) Lima, F. H. B.; Zhang, J.; Shao, M. H.; Sasaki, K.; Vukmirovic, M. B.; Ticianelli, E. A.; Adzic, R. R. Catalytic activity-d-band center correlation for the O_2 reduction reaction on platinum in alkaline solutions *J. Phys. Chem. C* **2007**, *111*, 404.

(133) Delley, B. An All-Electron Numerical-Method for Solving the Local Density Functional for Polyatomic-Molecules *J. Chem. Phys.* **1990**, *92*, 508.

(134) Delley, B. From molecules to solids with the DMol^3 approach *J. Chem. Phys.* **2000**, *113*, 7756.

(135) Tkatchenko, A.; Scheffler, M. Accurate Molecular Van Der Waals Interactions from Ground-State Electron Density and Free-Atom Reference Data *Phys. Rev. Lett.* **2009**, *102*.

(136) Mulliken, R. S. Electronic Population Analysis on Lcao-Mo Molecular Wave Functions .1. *J. Chem. Phys.* **1955**, *23*, 1833.

(137) Lee, Y. L.; Kleis, J.; Rossmeisl, J.; Shao-Horn, Y.; Morgan, D. Prediction of solid oxide fuel cell cathode activity with first-principles descriptors *Energy Environ. Sci.* **2011**, *4*, 3966.

(138) Lee, Y. L.; Kleis, J.; Rossmeisl, J.; Morgan, D. Ab initio energetics of LaBO3(001) (B=Mn, Fe, Co, and Ni) for solid oxide fuel cell cathodes *Phys. Rev. B* **2009**, *80*.

(139) Roth, W. L. Magnetic Structures of MnO, FeO, CoO, and Nio *Phys. Rev.* **1958**, *110*, 1333.